論文 / 著書情報
Article / Book Information

題目(和文)	
Title(English)	Development and Application of Viable Eddy Current Testing Methods for Corrosion Quantification and Stress Change Evaluation in Steel Structures
著者(和文)	BajracharyaSanjeema
Author(English)	Sanjeema Bajracharya
出典(和文)	学位:博士(学術), 学位授与機関:東京工業大学, 報告番号:甲第11533号, 授与年月日:2020年3月26日, 学位の種別:課程博士, 審査員:佐々木 栄一,廣瀬 壮一,岩波 光保,千々和 伸浩,BUI QUOC TINH,小林 裕介
Citation(English)	Degree:Doctor (Academic), Conferring organization: Tokyo Institute of Technology, Report number:甲第11533号, Conferred date:2020/3/26, Degree Type:Course doctor, Examiner:,,,,,
学位種別(和文)	博士論文
Type(English)	Doctoral Thesis

DOCTORAL DISSERTATION

Development and Application of Viable Eddy Current Testing Methods for Corrosion Quantification and Stress Change Evaluation in Steel Structures

By

Sanjeema BAJRACHARYA

Academic Supervisor

Associate Professor Eiichi SASAKI

Tokyo Institute of Technology

Department of Civil Engineering

2020

Table of Contents

List of figures

Chapter 1

Chapter 2

Chapter 4

List of tables

Chapter 2

Chapter 3

Chapter 4

Acknowledgements

I would like to express my deepest and sincerest gratitude to my supervisor, Associate Professor Eiichi Sasaki, for his invaluable guidance, constructive criticisms, and infallible advice without which this study would not have come to fruition. I am indebted to his very kind support, understanding, and positive reinforcements during the most exigent times during this doctoral study.

I am thankful to rest of the committee members – Prof. Iwanami, Prof. Hirose, Assoc. Prof. Kobayashi, Assoc. Prof. Chijiwa, and Assoc. Prof. Bui for their valuable comments and suggestions that contributed to the refinement of this dissertation. I would also like thank Assoc. Prof. Tamura, who is currently at Yokohama National University, for his kind advices during the early part of my research works.

I would like to extend my gratefulness to Mr. Joe Renaud, senior engineer at EddyFi (Canada) and Mr. Onodera from TechnoDenshi for their kind support and quick correspondences that proved crucial for the better understanding of Ectane and eddy current instrumentation, which propelled the progress of my research as well. The credit for arranging the highly fruitful meetings with TechnoDenshi and conference that led to link with Mr. Joe indubitably goes to my supervisor.

Special thanks goes to Ms. Ishihara for her help in processing the necessary documents for official works during my doctoral course. I would also like to express my gratitude to Assistant Professor Akutsu and Mr. Hirao for their help and support in conducting a part of my experimental works. My warm appreciation to all the current and graduate students from Sasaki lab I have met and known well for their friendship in and outside the lab environment.

Finally, I am ever grateful to my parents Ms. Sahida Bajracharya and Mr. Shreeghan Bajracharya for their unending support and understanding, my late grandfather Mr.

Dillisworananda Bajracharya who instilled in me the importance of perseverance, and the rest of my family for their mutual support.

Abstract

Steel structures forming an integral part of the infrastructures such as bridges, highways, and various offshore structures however are prone to corrosion, fatigue cracking, failure of joints like bolted connection due to reduction in bolt tension, etc. Therefore, structural health monitoring of these structures using non-destructive testing methods such as eddy current testing for gauging the extent of corrosion particularly under protective cover, detection of fatigue cracking, and reduction in bolt tension to maintain their safety and integrity is deemed crucial.

The present study has proposed corrosion profile estimation as a more viable approach to address the need for corrosion quantification method for steel members with corroded exterior, under protective cover, when the only side accessible to the eddy current probe is rough. On the other hand, the stress change evaluation in the structural members is identified as an important parameter and eddy current based stress measurement is established as a new, viable approach to detect the progress of damages such as fatigue cracking and reduction in bolt tension, through both numerical and experimental campaigns.

For the corrosion quantification, three-dimensional numerical simulations are conducted for characterization of the eddy current response against change in probe lift-offs and plate thicknesses at various excitation frequencies. Whereby, a lift-off estimation curve, constructed at the selected excitation frequency with no thickness effect, is used to obtain the corrosion profile of a corroded steel plate. Furthermore, the effect of probe geometry such as coil height, diameter, tilt, etc. are investigated to improve the estimation accuracy of the corrosion profile of the corroded steel plate, with or without the protective FRP or Titanium cover, which was compared against the corrosion profile data obtained from the laser displacement meter. Finally, corrosion severity

histogram constructed from the corrosion profile data is used to evaluate whether the overall corrosion is light, moderate, or severe.

For developing the methodology to conduct eddy current based stress measurement, three-dimensional numerical simulations are carried out for a steel plate subjected to change in relative permeability, representative of stress. The effect of other influential parameters such as lift-off, excitation frequency, and probe size on the eddy current response is also evaluated, for which a new, concise method called Phase diagram is proposed in the present study. It displays the concurrent changes due to the relative permeability and lift-off at an excitation frequency for a probe size, which facilitated in formulating the criteria for the selection of excitation frequency and probe size to conduct eddy current based stress measurement.

Next, the concept of the eddy current based stress measurement is tested out experimentally for its application in two example cases – detection of fatigue crack based on the stress change near the weld toe due to the crack and determination of bolt tension. The tensile test was first conducted to calibrate the eddy current index against the tensile stress, which was then used as calibration data for determining the stress near the weld toe of a butt-welded tensile specimen. The stress change behavior near the weld toe corresponding to the crack formation and propagation can be used in detection of cracks in further experimental campaigns. The mechanism of stress change behavior near the weld was also verified numerically through FE simulations of a butt-welded tensile specimen without and with cracks, whose dimensions are taken from the beach marks formed in the experiment. On the other hand, finite element modeling of a bolt with washer subjected to the bolt tension is conducted, affirming the change in stress at the bolt head for different bolt tensions. Then, experimental works are conducted whereby the eddy current response obtained at the bolt head was calibrated to the known value of bolt tension induced using

torque wrench and measured by a bolt tension calibrator, confirming the applicability of eddy current based stress measurement at the bolt head as a viable means for determining the remaining bolt tension.

Hence, corrosion profile estimation and eddy current based stress measurement have been devised in the present study for monitoring of the progress of damages such as corrosion, fatigue cracking, and reduction in bolt tension, with the experimental verifications of the feasibility of their applications.

Chapter 1. Introduction

Structural health monitoring of the steel structures has become crucial due to the increasing number of steel structures nearing the end of their design life, for timely repair and maintenance to meet the safety and serviceability standards. This chapter briefs the major concerns observed in the steel structures such as corrosion, fatigue cracking, failure of bolted connections, etc., various non-destructive testing methods that have been employed for their detection and quantification, related research, gap in the research, thus highlighting the purpose and objectives of this study.

1.1 Background

Steel structures form an integral part of the infrastructure such as bridges, highways, and various offshore structures owing to the ease of rapid construction and lightweight structure. However, they are prone to corrosion due to continuous exposure to environment, fatigue cracking under repeated and increasing traffic load, failure of connections such as bolted joints due to loss of bolt preload, etc., which compromise their safety, integrity, and serviceability conditions. Moreover, these structures are large in size and it is difficult to generalize and deduce the occurrence location or time of failure. Therefore, inspection and monitoring of these steel structures, using suitable non-intrusive techniques are necessary to preclude any catastrophic failures leading to loss of life and property. The present study has addressed these issues by investigating into viable, structural health monitoring approaches as elucidated below.

1.1.1 Corrosion

Corrosion occurring in steel structures due to long-term exposure to environment leads to reduction in the cross-sectional area of load carrying members and subsequent decrease in load bearing capacity, thus adversely affecting their structural strength and integrity [1-6], incurring an estimated global cost equivalent to 3.4% of the global Gross Domestic Product [7]. It is therefore important to quantify and monitor corrosion so that timely maintenance, repair and replacement works can be carried out economically, whereby savings up to 15-35% of the corrosion cost could be realized [7], while ensuring the functionality and safety of structures. Most of the literatures have used the method of determining the remaining thickness of a structural member to gauge the extent of corrosion and considered uniform reduction in the plate thicknesses to demonstrate the feasibility of the proposed concept and methods in determining the reduced plate thicknesses due to corrosion [8-15]. However, in case of unshielded steel sheet pilings or pipe pilings, with or

without protective covering, used in the foundation of bridges in a marine environment and buried piping having corroded exterior [16-18], the only accessible surface for inspection is the corroded one with highly undulated surface due to widespread, but non-uniform corrosion distribution. In such cases, it might be more feasible to determine the corrosion profile to evaluate the material loss due to corrosion rather than the remaining thickness of a steel member. This proves especially beneficial in estimating the irregular wall loss beneath the protective FRP (Fiber Reinforced Polymer) or Titanium cover of steel pipe piles [17] without having to remove the outer covering, as shown in Figure 1.1. Hence, the methodology to conduct corrosion profile estimation in view of determining the extent of corrosion should be developed.

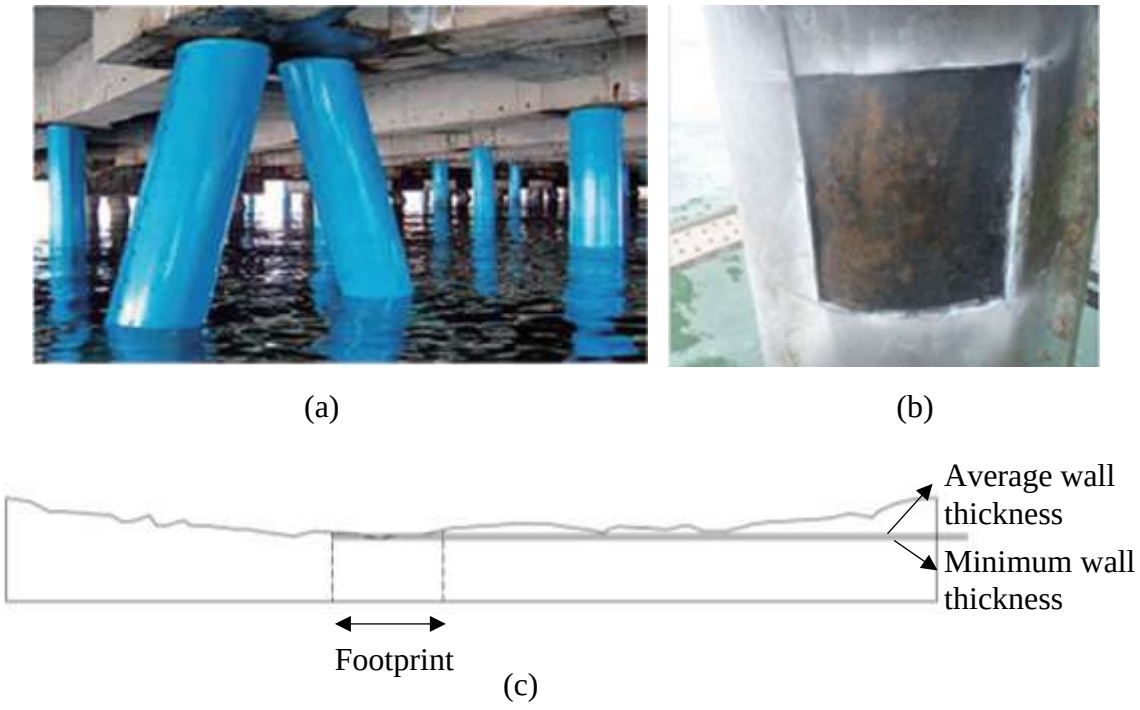

Figure 1.1 (a) Steel pipe piles used as the foundation in offshore structures with protective FRP over, (b) Corrosion under protective Titanium cover [17], and (c) Irregular wall loss occurring in Corrosion Under Insulation (CUI) [18].

1.1.2 Fatigue cracking

Fatigue failures are one of the major concerns in steel structures, as more and more of them reach towards the end of their design life. In addition to age, poor detailing, increased loadings with time such as larger traffic volume in a steel bridge, fabrication or construction imperfections, weld defects and holes, further reduce the fatigue life of the steel structures [19]. The fatigue cracks generally occur near the weld details, due to unfavorable welding residual stresses, stress concentrations due to weld geometry, etc., and discontinuities such as connection between floor beams and main load carrying members, stringer to floor beam connections, etc. [20]. However, unlike other forms of damages such as corrosion, they are difficult to detect during visual inspection since they are hair-like cracks and often hidden beneath the coating, at the initial stage of crack propagation [21]. These cracks when left undetected propagate into the structural member causing sudden, brittle fracture with little warning, causing catastrophic failure of the entire structure and loss of life and property [22]. Therefore, it is critical to detect the presence of fatigue cracks as early as possible for repair and maintenance of these steel structures. To this end, viable approaches to detect the fatigue cracks in existing steel structures should be investigated.

Figure 1.2 Fatigue cracks in Jiangyin Yangtze bridge [23].

1.1.3 Failure of bolted connection

Bolted connections have been used extensively in steel structures for their possibility of large load bearing capacity, lower installation cost, ease of installation and maintenance, unlike the riveted connections that are cumbersome and time consuming to install, remove, and offer limited clamp load [24]. However, bolted connections are susceptible to loosening due to vibration loads, which have been overcome by the use of pretension, high-strength bolts. They provide high tensile strength in flexure and tensile behaviors, high performance in fatigue loading due to the reduced stress range, and prevents bolt loosening due to vibration [25, 26]. Nevertheless, it is inevitable that these bolted connections suffer from self-loosening due to inadequate preloads during installation [24] or self-relaxation during service period. In addition, the loss of a section of the bolt head due to corrosion [27, 28] also results in the reduction of the bolt tension. This causes slippage between the components in the bolted connection due to reduced clamping force and affects the integrity and fatigue strength of the bolted connection [29, 30]. Therefore, it is of crucial importance to monitor bolt tension by using suitable non-destructive testing methods to ensure that it meets the minimum requirements to generate sufficient clamping force and achieve desired performance of the bolted connections.

Figure 1.3 Corrosion in a bolted connection [31]

1.1.4 Stress change evaluation

It is to be noted that all the aforementioned problems in steel structures involves the change in stress of the affected structural member. Corrosion causes stress concentration at the affected area due to the loss of material, which would be significant particularly for long-span steel bridges, and affect their load bearing capacity while, cracks cause redistribution of stress in the structural member to impede the crack growth [32]. On the other hand, bolt preload is the pretension applied in the bolt during installation, which is the axial stress applied to the bolt and is gradually reduced due to self-loosening, corrosion, etc.

Conventionally, the extent of corrosion is determined from the remaining thickness of the structural members [8-10, 13], the presence of fatigue cracks is detected by visual inspections and distortion of signals due to crack [21, 33], and the bolt tension is determined indirectly by measuring applied torque, or interface contact change due to change in bolt preload [30]. However, since stress variation has been identified as one common parameter for such varied failure scenarios of corrosion, fatigue cracking, and reduction in bolt preload, stress change evaluation is proposed in the present study as an alternative, more viable approach to qualitatively and quantitatively investigate these various failure scenarios. Furthermore, the proposed approach can also be used in determination of the stress distribution in the structural members of a skewed bridge, having non-uniform stress distribution for identifying a critical member. This is highly realistic, since asymmetries and heterogeneity cannot be avoided while conforming to the real-life conditions. Therefore, a highly robust method based on stress change evaluation in a structural member that would address various concerns in the structural health monitoring of the steel structures is being investigated in the present study.

1.1.5 Non-destructive testing methods

The inspection and monitoring of the damages such as corrosion, cracks, and condition of bolted connections for structural health monitoring of steel structures are carried out by using non-destructive testing methods such as ultrasonic testing [3, 27, 30, 34-36], eddy current testing [8-15, 21, 33, 37-39], infrared thermography [27, 40, 41], acoustic emission method [30, 42, 43], and piezoelectric method [30, 44, 45]. In addition to the above-mentioned methods, X-ray diffraction method is used for measuring the stress in a structural member [46-48]. However, many of these methods require surface preparation of the test material and contact between the sensor/probe and the test material by using a coupling agent, lack repeatability, and have high sensitivity to temperature, dust, and rust [49]. As a result, they are not the most feasible for field applications. Although eddy current testing requires skilled operator to conduct measurement and analyze the data, it is a non-contact method that does not require direct contact with the surface to be inspected. As a result, the rust or dust layer and protective covers, which have poor conductivity do not affect the induction of eddy current on the steel surface to be inspected. Therefore, eddy current testing does not require surface preparation or use of a coupling agent between the probe and the surface to be inspected. It is much more workable and time and cost efficient particularly for field applications and therefore has been selected in the present study for stress change evaluation in a steel structural member.

1.2 Related research

1.3.1 Corrosion profile estimation

The extent of corrosion can be ascertained by measuring the remaining thickness of a steel member using various non-destructive testing and evaluation methods such as ultrasonic testing [3], eddy

current testing [8, 9], and pulsed eddy current testing [11]. Unlike ultrasonic testing, eddy current testing does not require post- and pre-treatment of inspection surface, couplant or direct contact [8] and therefore is highly convenient for remaining thickness measurement without having to remove rust, dirt, or protective coverings such as fireproofing and insulation.

On the other hand, pulsed eddy current testing uses a pulse or square wave consisting multiple frequency contents, providing more information in a single measurement [11] than conventional eddy current testing. However, to improve the sensitivity of pick-up coil, it is provided with large number of turns thus increasing the probe size [50]. Since, only average thickness of the sensing area beneath the probe is obtained in either [18, 51], sensitivity of the probe to small but continuous thickness changes, occurring in steel members exposed to highly corrosive environment or due to irregular wall loss occurring beneath protective coverings, decreases as the probe size increases. Hence, eddy current testing is deemed best for evaluating the continuous variation of thickness of a corroded steel member.

Different variations of eddy current testing such as single frequency [52], multi frequency [13-15], swept frequency [10, 53], and low frequency [55] have been proposed for measuring the thickness of metal films, plates, pipes, etc. and inspection of wall thinning of large pipes. Nevertheless, most of them [10, 13-15] focus on estimating the thickness of a uniform plate, rather than continuous changes in the plate thickness. Whereas, corrosion or material loss profile in a plate geometry has been reconstructed analytically, using eddy current testing, by linearizing the relationship between the material loss profile and the measured impedances [55] and by joint application of eddy current testing and particle swarm optimization technique [56]. Nevertheless, only backside corrosion has been considered in these studies and eddy current measurements are

conducted from the smooth side only. Furthermore, the analytical solutions are complex, entailing a need for simpler method to estimate the corrosion profile.

Tamura et al. (2015) have experimentally obtained the distance to the steel surface from the probe elevation, using detected voltage as an index, to determine the remaining thickness of a corroded steel plate, which in essence is the determination of corrosion profile through probe lift-offs [51]. However, it is be noted that not only probe lift-offs but also the change in plate thickness affects the detected voltage at any excitation frequency [8], which has not been addressed in this study. Moreover, the dimensions of a commercial probe targeted for general surface inspections might not be optimal for the detailed estimation of the corrosion profile, whereby the need for study of geometric parameters of the selected probe was felt.

Besides the geometric parameters, the configuration of a probe also plays an important role in the determination of the corrosion profile. Although several innovative probes such as differential planar eddy current probe [57], differential type plus point probe [58], biorthogonal rectangular probe [59], uniform eddy current probe [60, 61], E-shaped core coil [62], coil arrays [63-65], etc. have been developed till date, they are targeted for detection and characterization of isolated flaws. However, the efficiency of these probes in continuous determination of small changes in the corrosion profile is not clear. Therefore, in the present study, a reflection probe comprising of an exciting coil and a detecting coil is selected for its higher gain and wider frequency range to be able to grasp the small changes in the corrosion profile. Furthermore, its structure is geometrically optimized through the parametric study conducted via numerical simulations.

Regarding the numerical modeling, eddy current problems can be simplified into 2D axisymmetric problems [8, 9, 66] or modelled in 3D [30, 52, 59, 63], the latter having high

computational cost. Nonetheless, since the probe has to be moved over the corroded steel plate to obtain its corrosion profile, it necessitates three-dimensional modeling of the problem. Therefore, in the present study, all the numerical simulations are carried out in 3D in the AC/DC module of the FEM software, COMSOL Multiphysics 5.2a.

1.3.2 Eddy current based stress measurement

The stress in a steel plate can be measured by strain gauges or non-destructive testing methods such as X-ray diffraction, ultrasonic testing, and eddy current testing [46-48, 67]. However, strain gauges are limited to the predetermined gauge locations [47] while X-ray diffraction and ultrasonic testing methods require surface preparation [48, 67] such as removing the top rust layer in a corroded girder. Furthermore, X-ray diffraction requires specific operating conditions due to radiation hazard for the personnel [46], while ultrasonic testing requires use of couplant between the probe and test surface [8, 47], thus making them time consuming, costly, and not preferable for on-site inspections. On the other hand, eddy current testing [8], being non-contact method, does not require surface preparation nor the use of a couplant, and therefore is much more convenient, time-, and cost-efficient for field investigation. Hence, eddy current testing has been selected in the present study as a means to determine the stress state of a steel plate.

Eddy current testing can detect stress change in a magnetic material such as steel, based on the Villari effect or inverse magnetostrictive effect, whereby the change in stress causes domain reorientation in magnetic materials and changes their magnetic permeability, which in turn is reflected in the eddy current signal [46, 68, 69]. Eddy current based stress measurement has been used in the measurement of internal stresses of mechanical equipment in industry [46, 67], tension force in post-tensioning (PT) tendon [70], and pre-stressed steel bars, cables, and strands in reinforced concrete constructions [71-75]. However, it has not been implemented yet in the

evaluation of stress state of structural members for a wider variety of damages such as fatigue cracking, corrosion, loss of bolt preload, etc.

As for the configuration of eddy current probes, sensors with U-shaped ferrite core having coil winding on both legs [46] or on the core body [71, 72], E-shaped core [71], eddy current array sensor [73, 74], single coil sensor [75], ring-type eddy current sensor with two coils [70], and planar eddy current sensor [67] have been employed for force or stress measurement in the aforementioned studies. However, they are mostly for inspection of cables and designed to encircle them, whereas, a surface probe is required for the inspection of a flat surface such as steel plate girder for crack detection or to place over the bolt head to measure bolt tension, therefore, requiring a proper methodology to conduct the eddy current based stress measurement. Moreover, lift-off has been maintained at a constant minimum of 0.125 mm [46] or 0.1 mm [73] to ensure sufficient sensitivity of the eddy current probe, but highly varying lift-offs are often inevitable in onsite inspections, for example, in a corroded girder surface. Hence, a reflection probe with an outer exciting coil and an inner detecting coil that provides high gain has been selected for the present study, for better sensitivity to lift-offs.

Furthermore, only [71, 72, 75] have considered the effect of excitation frequency on the eddy current response and have used optimized frequency for determining the stress. In addition, only one study has considered the effect of probe size [71], concluding that miniaturization of the probe provides better sensor sensitivity, which however might not hold true when factoring in the influence of lift-offs. Hence, the present study has also taken into account the influence of excitation frequency and probe size on the eddy current response, and their selection for the stress measurement.

1.3.3 Fatigue cracking and bolt tension

The cracks on the surface are conventionally detected by the distortion of eddy currents around them, reflected in the eddy current signal. However, in case of welded structures, fatigue cracks originate from the weld toe and eventually propagate into the structural member rather than on the surface as shown in Figure 1.4. In addition to this, in weathering steels a layer of rust is formed, which acts as a protective layer to prevent further rusting. In such a case, it is not reliable to hold the eddy current probe over the weld corner to detect the presence of fatigue crack near the weld directly, as seen in Figure 1.4 (a), because of the rust layer and tilting of the probe with unlikely possibility of maintaining a constant lift-off at different measurement time. To overcome this, the present study proposes to determine the stress change behavior near the weld toe with the eddy current probe held horizontal as shown in Figure 1.4 (b), for an indication of crack formation and propagation, since it is known that stress near the weld changes due to the crack as shown in Figure 1.5. Before cracking, the stress is maximum at the weld toe and decreases as the distance from the weld toe increases. In contrast, after cracking occurs, the stress near the toe is small and increases as the distance from the weld toe increases. Hence, in the present study, the concept of eddy current based stress measurement is used to observe the stress change behavior near the weld toe due to fatigue crack formation and propagation.

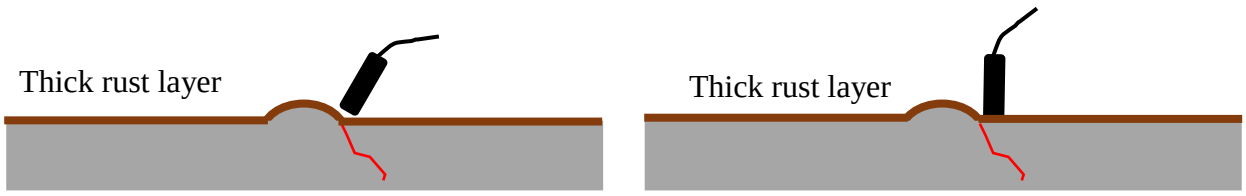

(a) (b)

Figure 1.4 (a) Accessibility problem to eddy current probe at the weld corner with probe tilt, (b) Stress measurement near the weld toe without any probe tilt.

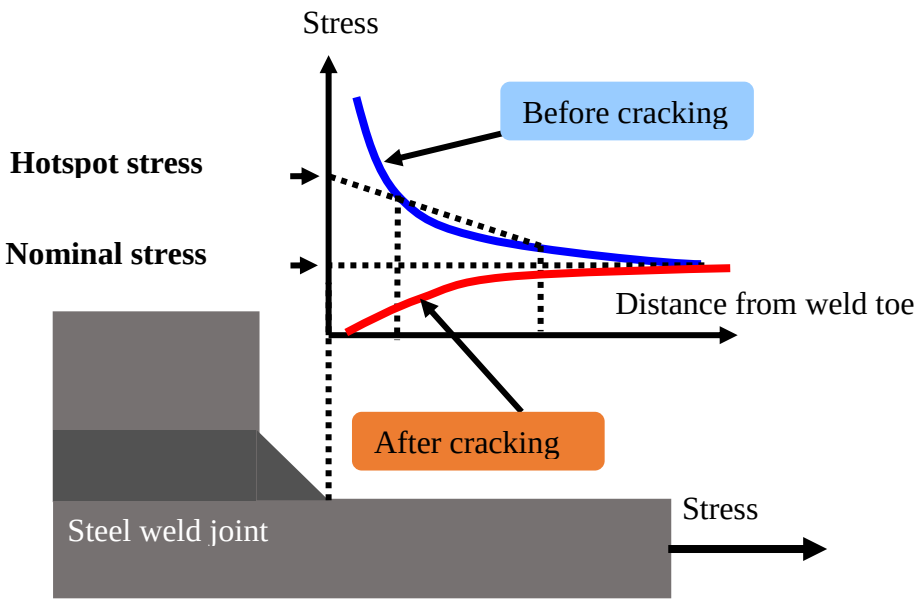

Figure 1.5 Stress variation near the weld toe before and after cracking.

As for the determination of bolt tension, the strain gauges are attached to the bolt body to measure the tensile strain change in the bolt [25, 26, 30], torque wrench technique is used to ensure sufficient torque to the bolt [30, 76]. In addition to the other non-destructive testing methods such as ultrasonic method [27, 30, 76], vibration based methods [24, 30, 37, 76], piezoelectric active sensing or impedance methods [30, 44, 76], sensors or smart systems specifically designed to measure bolt tension are used [77, 78]. However, the strain gauges need to be integrated into the bolts, which might not be the most time and cost efficient option, while the torque wrench technique shows large intrinsic errors in the estimation of actual bolt tension the torque applied is dissipated mostly by friction, and does not allow for the continuous monitoring. On the other hand, the specifically designed sensors and smart sensors are likely to be expensive for long-term monitoring, the vibration based methods lack repeatability, and the ultrasonic and piezoelectric methods require extensive surface preparation. Hence, in the present study, a more workable approach to measure the bolt tension using eddy current based stress measurement is proposed.

1.3 Purpose and objectives

Hence, the purpose of this study is to develop viable eddy current testing methods for quantifying corrosion when the only accessible side to the eddy current probe is rough and for stress change evaluation in steel members as a new, more workable approach for structural health monitoring, while testing their applicability via experimental campaigns. The objectives of the present study can be summarized as follows:

- Develop a methodology to conduct corrosion profile estimation of a corroded steel plate with and without a protective cover, when the only side accessible to the eddy current probe is rough,
- Develop a methodology to conduct eddy current based stress measurement by investigating the effect on the eddy current response due to change in stress of a steel plate, through numerical simulations, and
- Explore the applicability of eddy current based stress measurement in detection of fatigue cracking and determination of bolt tension through experimental works through stress change evaluation, supported by the numerical analysis.

1.4 Outline of dissertation

The dissertation is organized as follows:

Chapter 1: Introduction

Background, purpose and the objectives of the study, related research and need for more viable approaches for inspection and monitoring of these structures were discussed.

Chapter 2: Numerical study on corrosion profile estimation of a corroded steel plate using eddy current testing

The corrosion profile estimation is established as a viable method to quantify corrosion in a steel plate with corroded exterior with rough accessible to the eddy current probe, without having to remove the outer protective covering, by using a geometrically optimized probe.

Chapter 3: Eddy current based stress measurement on a steel plate using Phase diagram

The effect of change in stress of a steel plate, in addition to lift-off, excitation frequency, and probe size on the eddy current response was investigated using a concise representation termed as Phase diagram, which further facilitates the selection of excitation frequency and probe size.

Chapter 4: Experimental investigation on application of eddy current based stress measurement

The concept developed in Chapter 3 was used to detect the fatigue crack near the weld toe of the steel specimen and the remaining bolt tension based on the stress change evaluation.

Chapter 5: Conclusions and recommendations

This chapter summarizes the results from each chapter and provides further recommendations for extension of the present study.

Chapter 2. Numerical Study on Corrosion Profile Estimation of a Corroded Steel Plate using Eddy Current

This chapter presents corrosion profile estimation as a method to determine the extent of corrosion in steel members having corroded exterior, with or without protective cover, when the only side accessible to the eddy current probe is highly uneven. A high frequency eddy current method is proposed to estimate the corrosion profile of a steel plate directly from the probe lift-offs regardless of varying plate thickness. The three-dimensional, numerical simulations were carried out in a FEM software to verify the suitability of this method. A parametric study is conducted to determine the effect of coil height, diameter, their ratio, and tilt angle of reflection probe on the estimation accuracy of a triangular notched profile, representative of corrosion, whereby a geometrically optimized probe is obtained. It is then employed to determine the corrosion profile of a corroded steel plate with and without protective cover. The estimated corrosion profiles show good agreement with the actual profile measured by laser displacement meter, confirming the sufficiency of proposed method.

2.1 Overview

In this chapter, a method using high frequency eddy current is proposed to obtain the corrosion profile of a steel plate with and without protective cover, considering that the only side accessible to the eddy current probe is rough, by using a geometrically optimized, reflection probe. It is structured as follows. First, a method to obtain a unique detected voltage and lift-off relationship at a particular excitation frequency such that corrosion profile can be obtained directly from the probe lift-offs, regardless of the varying plate thickness, is elucidated. Then, finite element modeling of the eddy current problem is described. Next, a parametric study is conducted to investigate the influence of geometric parameters of the reflection probe namely, coil height, diameter, their ratio and tilt angle on estimating a triangular notched profile, representative of corrosion, whereby a reflection probe with optimized geometric parameters is obtained. Thus obtained geometrically optimized probe is used to determine the corrosion profiles of a corroded steel plate with and without the protective FRP or Titanium covers, and compared to the actual profile measured by laser displacement meter. Finally, the data obtained from corrosion profile is used to construct a corrosion severity histogram to evaluate the extent of corrosion.

2.2 Proposed method for corrosion profile estimation

In this study, the probe is moved above the corroded steel plate at a constant elevation from the base of the plate, greater than the highest point in the corroded surface, and continuously acquires lift-offs at each probe location. The probe lift-off at any location, being the distance from the bottom of probe to the corroded steel surface, can therefore be directly used to determine the corrosion profile. However, as mentioned earlier, the response of the probe is not only affected by lift-offs, but also thickness changes of the steel plate. Therefore, to eliminate the undesirable influence of continuously varying thickness of the corroded steel plate, frequency characteristics

of the eddy current probe is explored, and a method to obtain the lift-offs independent of thickness variation is established.

2.2.1 Detected voltage as an index

Reflection probe (Figure 2.1) considered in the present study consists of two concentric circular coils - an outer exciting coil and an inner detecting coil. The exciting coil, supplied with an alternating current of constant amplitude, induces eddy current in the steel plate, which is then picked up by the detecting coil. The voltage thus acquired by the detecting coil serves as a good indicator for changes in the eddy current due to change in probe lift-off and plate thickness. Hence, the detected voltage is taken as an index to determine the probe lift-offs and plate thicknesses.

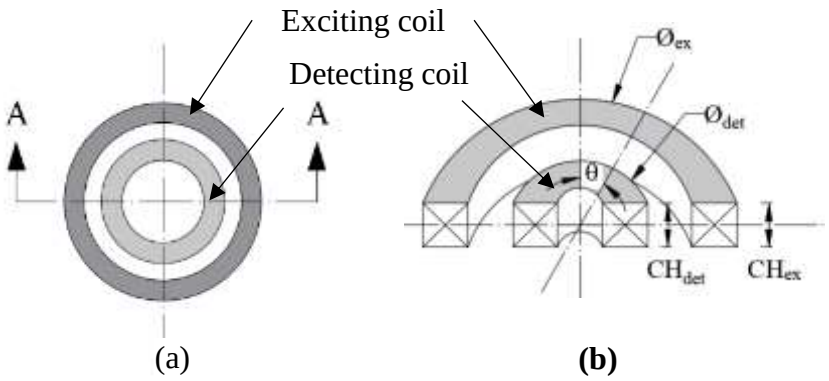

Figure 2.1 (a) Top view of the coils in the reflection probe, and (b) cross-section at A-A.

For a particular probe specification, the detected voltage has a unique relationship with lift-off for a given plate thickness; it decreases with the increase in lift-off. This is plausible since the coupling between probe and plate weakens as the lift-off becomes larger, consequently resulting in smaller induced eddy current and detected voltage. Therefore, the lift-off at a probe location can be calculated from the detected voltage values based on this relationship.

Nevertheless, the relationship is only for a single plate thickness and in case of a corroded steel plate with continuously differing plate thicknesses, a number of detected voltage versus lift-off relationships are to be obtained for each thickness, making the computation process extremely tedious. If this effect of thickness on detected voltage can be eliminated, then a single relationship can be established between detected voltage and lift-off, independent of plate thickness variation. For this, excitation frequency characteristics of the probe is investigated in relation to the penetration depth of the eddy current.

2.2.2 Standard penetration depth of eddy current

Standard penetration depth is the depth below the surface at which the eddy current density decreases to about 1/e or 37% of its surface value [79]. It gives an indication of how deep eddy currents can penetrate into the test specimen, and can be calculated as:

$$\delta = \sqrt{\frac{2}{\mu\omega\sigma}} \qquad (2.1)$$

where, δ is the standard penetration depth in meters, σ is the electrical conductivity of test material in S/m, μ is the magnetic permeability of test material in H/m, given by $\mu = \mu_r\mu_0$, where μ_r is the relative magnetic permeability and μ_0 is the magnetic permeability of the vacuum (4π x 10^{-7}H/m) and $\omega = 2\pi f$, where f is the excitation frequency in Hz.

It can be deduced from equation (2.1) that penetration depth of the eddy currents decreases as the frequency increases so that at higher frequencies, eddy currents are concentrated at the surface. Hence, the influence of thickness changes of the steel plate on the eddy current response at higher frequency will be minimal and can be neglected. The present study utilizes this

characteristic of high frequency to determine the excitation frequency of the probe that is, more or less, immune to the thickness variation.

2.2.3 Excitation frequency and lift-off estimation curve

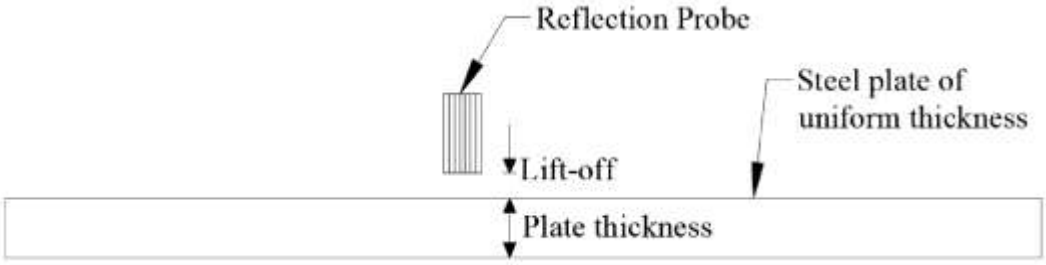

Figure 2.2 Calibration of the reflection probe.

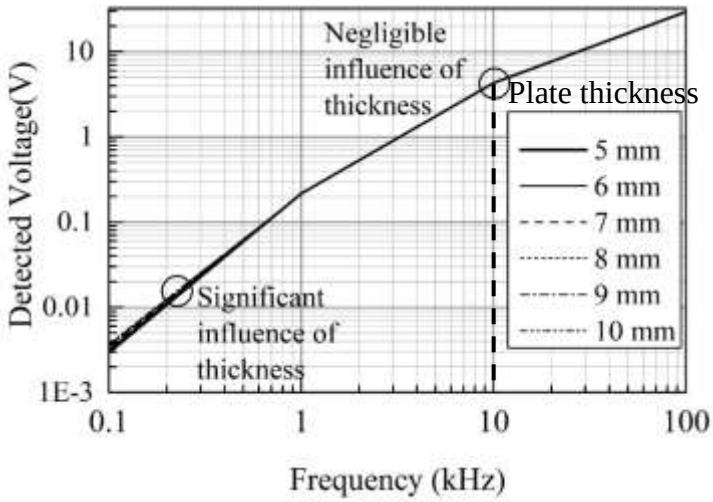

Figure 2.3 Log-log graph of detected voltage versus excitation frequency at a constant lift-off of 0 mm for different plate thicknesses.

First, calibration (Figure 2.2) is carried out through numerical simulations by using uniform steel plates of different thicknesses, simultaneously varying the probe lift-offs, for different excitation frequencies to determine the changes in detected voltage. An alternating current of constant amplitude is supplied to the exciting coil and the voltage detected by the probe for different plate

thicknesses for a constant lift-off at different excitation frequencies are plotted (Figure 2.3). It can be seen that at high frequency, the influence of thickness on the detected voltage is the least and can therefore be neglected.

This can also be clarified by plotting detected voltage versus lift-off for different plate thicknesses at a low frequency, whereby a number of curves were obtained indicative of thickness effect (Figure 2.4 (a)) whereas, all the curves converged into one at high frequency showing that the influence of thickness becomes insignificant (Figure 2.4 (b)). Thus, the frequency with negligible thickness effect is selected as the excitation frequency of the probe. Then, a single curve, henceforth termed as the lift-off estimation curve (Figure 2.5), is constructed at that frequency depicting the unique relationship between detected voltage and lift-off, independent of varying plate thickness. Hence, the lift-off at any probe location corresponding to the detected voltage of the probe can now be directly used to estimate the corrosion profile.

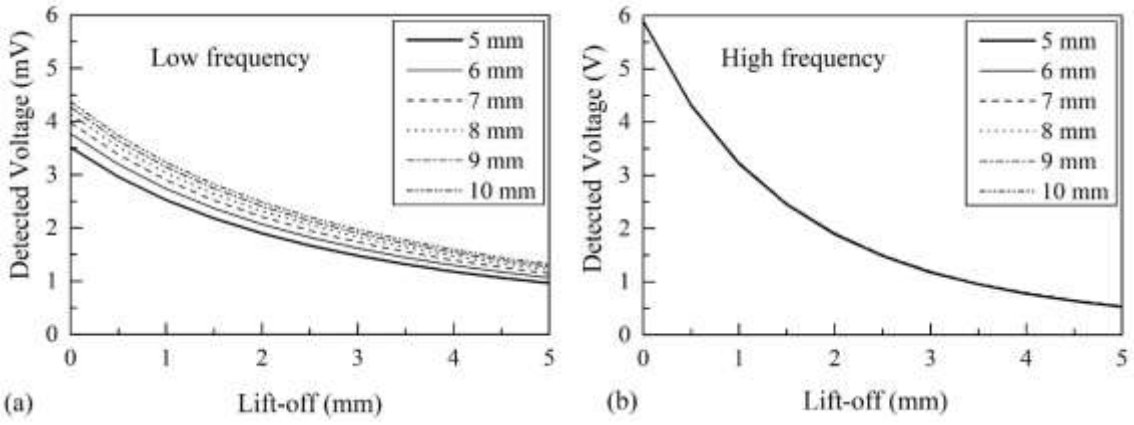

Figure 2.4 Detected voltage versus lift-off for different plate thicknesses at (a) low and (b) high frequencies with prominent and negligible thickness effects, respectively.

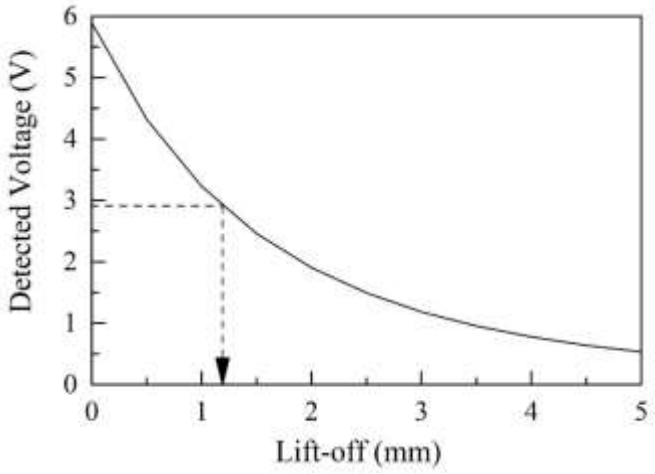

Figure 2.5 Lift-off estimation curve at the selected excitation frequency.

2.2.4 Approximation of lift-off estimation curve

The lift-off estimation curve (Figure 2.5) is non-linear and a suitable function is required to approximate it as closely as possible to determine lift-offs corresponding to the detected voltage precisely and preclude the accumulation of error in the corrosion profile estimation.

Firstly, a single exponential function $y = \alpha e^{-\beta x}$ was used to approximate the curve (Figure 2.6(a)), which highly underestimated and slightly overestimated the lift-offs at smaller and higher values, respectively, ultimately leading to the corresponding overestimation and underestimation of a profile. Secondly, to approximate lift-offs better at smaller values, the lift-off estimation curve was partitioned into two (Figure 2.6(b)) – $y = \alpha_1 e^{-\beta_1 x}$ for smaller lift-offs and $y = \alpha_2 e^{-\beta_2 x}$ for larger lift-offs. Lastly, after the single-line and two-line approximations, the multi-line approximation was used for representing the lift-off estimation curve (Figure 2.6(c)), where a line $y = m_i x + c_i$ was fitted to each stretch of 0.5 mm between the lift-offs such that it

followed the actual curve the closest.

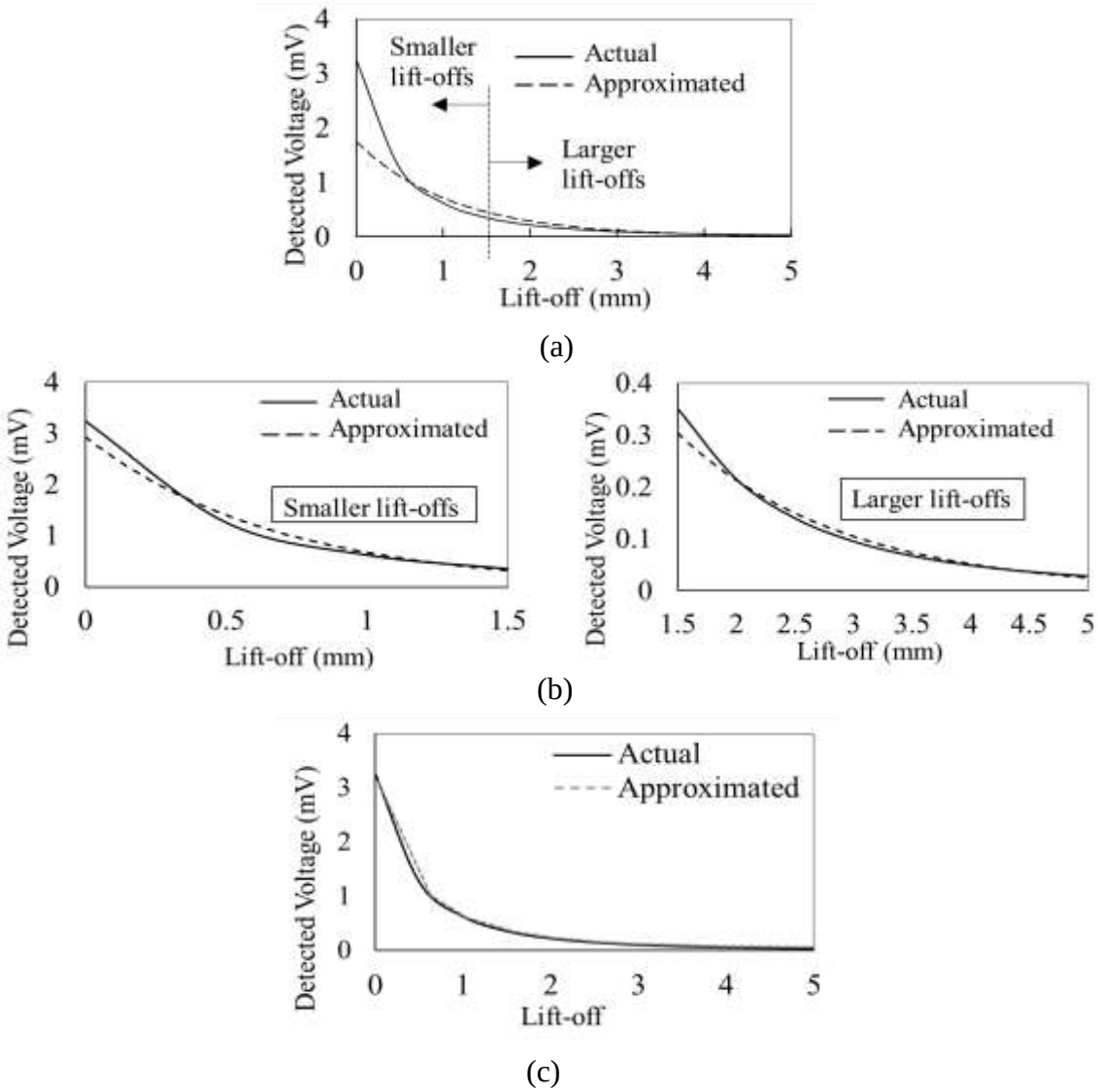

Figure 2.6 (a) Single-line, (b) Two-line, and (c) Multi-line approximations of the lift-off estimation curve.

The three approximations are used to assess the magnitude of error due to single line approximation and whether two-line approximation suffices or multi-line approximation is required to minimize the errors in corrosion profile estimation due to inexact representation of the lift-off estimation curve.

2.2.5 Triangular notched profile

Prior to employing a probe of any specification to estimate the corrosion profile, a parametric study is conducted to determine the influence of geometric parameters of the reflection probe on the estimation accuracy of the profile of a triangular notched steel plate (Figure 2.7). The triangular notch is representative of the change in surface profile due to corrosion. The 200 mm long and wide, 10 mm thick triangular notched plate consists of a 0.5 mm deep and 10 mm wide triangular notch at the center. The depth of the notch is taken to 0.5 mm as the average of the largest number of distance to the healthy steel layer, which lies between 0.4 - 0.6 mm, based on the corrosion distribution obtained from the laser displacement data for the surface of the corroded steel plate (Figure 2.8). And, the width is taken as 10 mm, corresponding to the diameter of the largest probe.

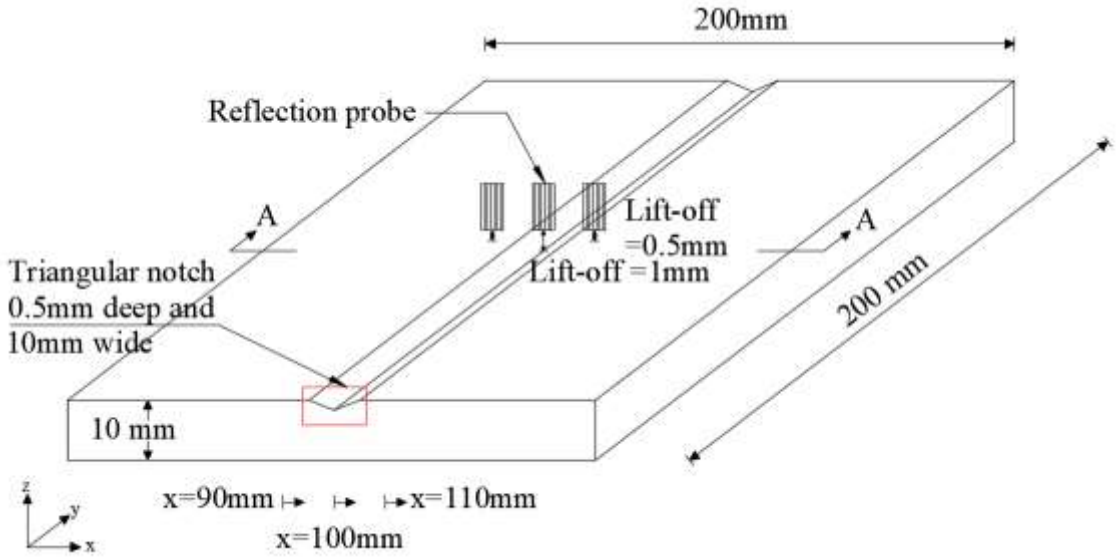

Figure 2.7 Triangular notched steel plate.

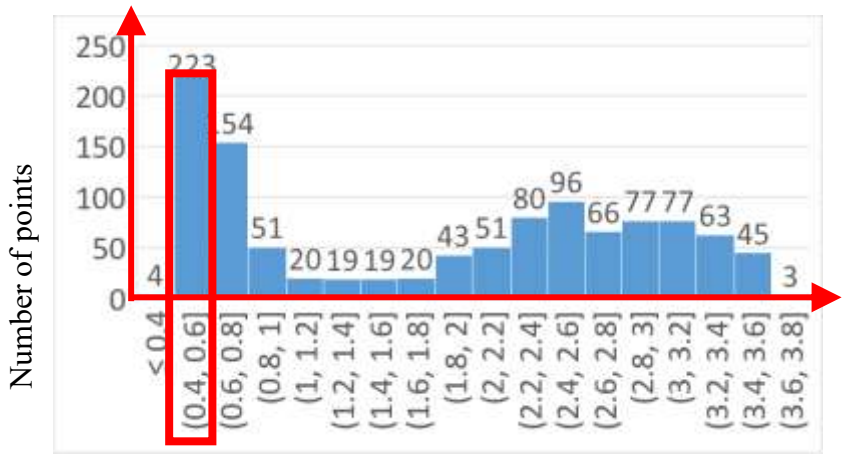

Figure 2.8 Corrosion distribution.

Each probe of differing geometric specification scans from x = 90 mm to x = 110 mm with the apex of triangular notch at x = 100 mm, as illustrated in Figure 2.7. The probe is held at a constant height of 10.5 mm from the base of plate as it moves, giving a minimum lift-off of 0.5 mm and a maximum lift-off of 1 mm. The lift-offs corresponding to the detected voltages are then calculated from the lift-off estimation curve and the triangular notched profile is constructed. Based on this parametric study, a geometrically optimized probe that gives the best estimation of triangular notched profile is obtained and is thereafter employed in tracing the corrosion profile of the corroded steel plate.

2.3 Finite element modeling

The numerical simulations are carried out in the frequency domain of the AC/DC module of the commercial software COMSOL Multiphysics 5.2a using three-dimensional, finite element models of the probes, uniform steel plates (for calibration), triangular notched steel plate, and corroded

steel plate with and without FRP or Titanium cover. The governing equation for the eddy current problem of electromagnetic induction [58] is

$$(j\omega\sigma - \omega^2\varepsilon)A + \nabla \times (\mu^{-1}\nabla \times A) = J_e \qquad (2.2)$$

where, ω=2πf is the angular frequency, with f being the excitation frequency of the probe, σ is the electrical conductivity, ε is the relative permittivity, μ is the magnetic permeability of the steel plate, A is the magnetic vector potential, and J_e is the external current density provided by the exciting coil. The symbol ∇ (Nabla operator) denotes the three-dimensional gradient operator, where ∇x denotes the curl operator.

The reflection probe is modelled using two concentric coils – the outer exciting coil and the inner detecting coil, each represented by a homogenized, multi-turn, cylindrical coil, as shown in Figure 2.9 (a). An alternating current of 1A is supplied to the exciting coil. The steel plates used for calibration are 200 mm long and wide, with varying thickness (Figure 2.9 (b)).

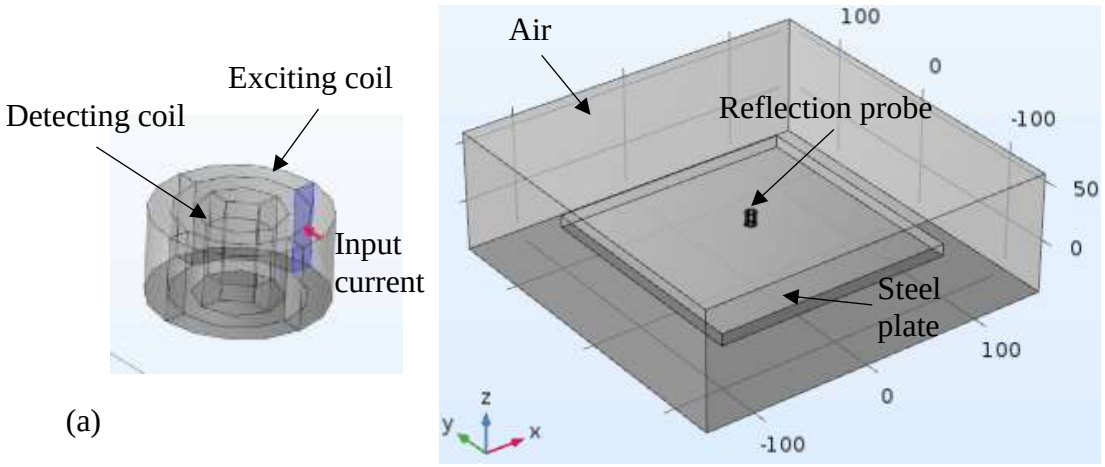

Figure 2.9 (a) Numerical model of the reflection probe and (b) its calibration using uniform steel plates.

Although the actual corroded specimen is 150 mm long and 30 mm wide (Figure 2.10 (a)), because the data measured by laser displacement meter is only for a length of 100mm, the numerical model of corroded steel plate, 100 mm long and 30 mm wide. The x-,y-, and z-coordinates of the surface obtained from the laser displacement meter was used to create the numerical model of the corroded steel plate in ABAQUS with a 100 x 300 mesh (Figure 2.10 (b)). The MeshLab software was then used to convert it to the *.STL format (Figure 2.10 (c)), which is importable into the COMSOL Multiphysics 5.2a (Figure 2.10 (d)). The protective FRP and Titanium covers (Figure 2.10 (e)) are also 100mm long, 30 mm wide, but are 2.5 mm and 1mm thick [17], respectively. The computational domain (air) for all the simulations is 300 mm x 300 mm x 100 mm, where the boundary condition was imposed such that the tangential component of the magnetic vector potential is zero.

The built-in materials available in COMSOL Multiphysics 5.2a namely *Air*, *Copper*, *Steel AISI 4340*, and *Titanium beta-21S* have been assigned to the air domain, coils, steel plates and the titanium cover. On the other hand, a *Blank Material* is created, to which appropriate properties are provided to represent FRP. Since the electrical conductivity of FRP is direction-dependent, separate electrical conductivities have been set in the longitudinal, transverse and thickness directions [80]. The material properties thus allocated are listed in Table 2.1. The *Free tetrahedral* mesh with the minimum and maximum element size of 0.1-0.5 mm to 10-40 mm was assigned to the steel plate, and air domain for smaller to larger probes. Whereas, a finer mesh with minimum and maximum element sizes of 0.001-0.5 mm to 1-10 mm was assigned to the coils corresponding to the smaller and larger probes. A very small value of electrical conductivity has been given to the air domain in view of the numerical stability of the three-dimensional problem.

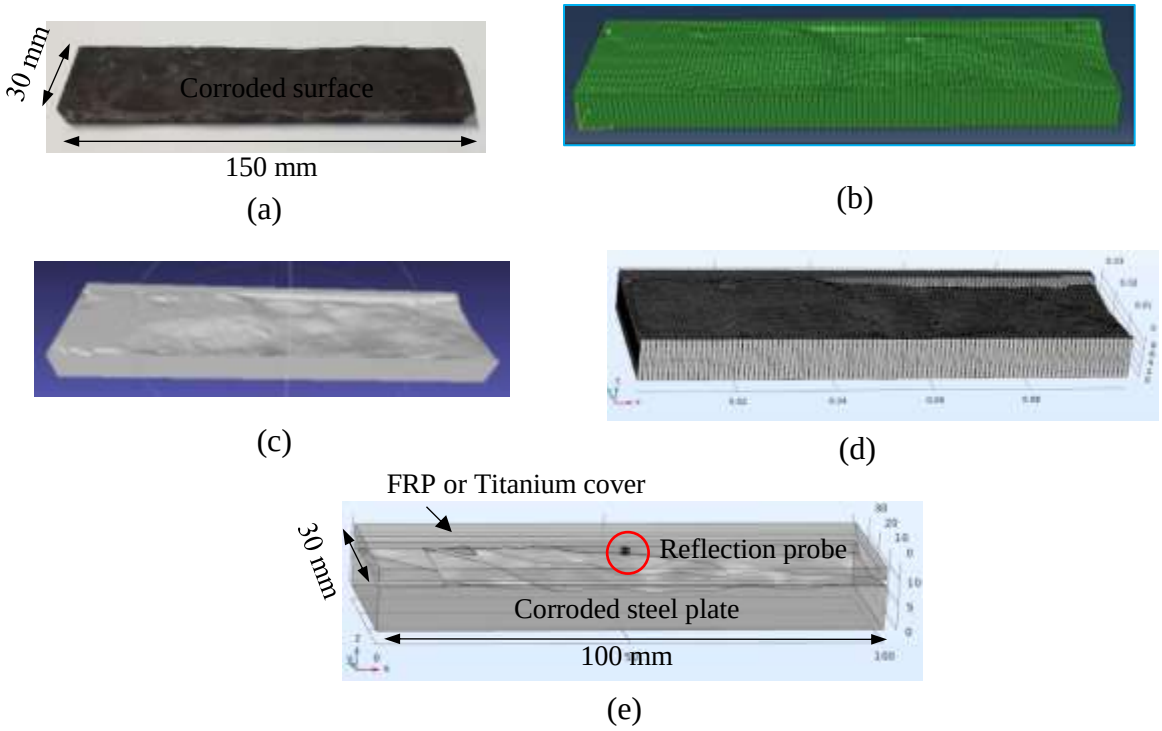

Figure 2.10 (a) Actual corroded steel plate, (b) 100x30 mesh model of the corroded steel plate in ABAQUS, (c) Conversion to *.STL format in MeshLab, (d) Mesh of the numerical model imported into COMSOL, and (e) Numerical model of the corroded steel plate with FRP or Titanium cover in COMSOL.

Table 2.1 Material properties

Domain	Air	Coils	Steel plates	FRP cover	Titanium cover
Relative permeability	1	1	1	1	1
Electrical conductivity [S/m]	0.1	5.998×10^7	4.032×10^6	1×10^5, 10, 5	7.407×10^5

2.4 Parametric study

The influence of geometrical parameters of the reflection probe namely, coil height, diameter, their ratio, tilt angle on the estimation accuracy of the triangular notched profile was investigated. The calibration was conducted for each probe, from which the excitation frequencies were determined, and the lift-off estimation curves were constructed. Numerical simulations were then carried out by moving the probes above the triangular notched plate at a constant elevation of 10.5 mm and the profiles were constructed using the corresponding lift-off estimation curves.

2.4.1 Probe specifications

Corrosion probes for general surface inspections by the eddy current manufacturers such as **b** ETHER NDE [81] and OLYMPUS NDT [82] have diameters ranging from 6.3 mm to 32 mm. Akutsu et al. (2017, 2018) [8, 9] and Tamura et al. (2015) [51] have used commercial probes of 16 mm and 7.5 mm diameter from GE Inspection Technologies [83], respectively. In the present study, 10mm is taken as the average diameter of a commercial probe based on the minimum available diameter and sizes of the commercial probes in the aforementioned studies, and reasonable values are assumed for the remaining parameters, which are then gradually changed to get the optimum values.

The specifications of eight reflection probes thus obtained are listed in Table 2.2, and a schematic is provided in Figure 2.1(b). Here, θ is the tilt angle of the probe, ϕ is the coil diameter, CH is the coil height, and N is the number of turns of wire in the coil. The subscripts *ex* and *det* correspond to the exciting and detecting coils. The letters L and S in the name of probes indicate that the probes are considered as large and small diameter probes, respectively.

Table 2.2 Probe specifications

Probe Name	θ(°)	ϕ_{ex} (mm)	ϕ_{det} (mm)	CH_{ex} (mm)	CH_{det} (mm)	N
0degLProbe1	0	10	6	10	10	1000
0degLProbe2		10	6	5	5	1000
0degSProbe1		4	2	1	1	100
0degSProbe2		2	1	1	1	100
90degLProbe1	90	10	6	10	10	1000
90degLProbe2		10	6	5	5	1000
90degSProbe1		4	2	1	1	100
90degSProbe2		2	1	1	1	100

2.4.2 Tilt angle of the probe

Four different tilt angles of the probes, θ = 0°, 30°, 60°, and 90° were examined for their influence on the distribution of eddy current densities on a uniform steel plate. Figure 2.11 presents the eddy current distribution due to probe tilt, red and blue indicating the highest and the lowest density. Furthermore, the 3D cut line graphs (bottom figures) of eddy current density obtained at the dotted line in the top figures illustrate the variation of magnitude of eddy current density.

The largest eddy current density is observed for θ = 90° probe and the smallest for θ = 0° probe. In addition, the distribution of eddy current is symmetric in θ = 0° and 90° probes, unlike the asymmetric distributions in θ = 30° and θ = 60° probes that are also the causes of errors in the measurement. Moreover, maximum value of eddy current density is at the probe center for θ = 90° probe whereas, for θ = 0° probe, the largest value is directly beneath the coil but minimal at the probe center. Thus, in view of the symmetric distribution of eddy current and the impact of eddy current being concentrated at the probe center or beneath the coil on estimation accuracy, only the tilt angles, θ=0° and 90° have been considered for analysis (Table 2.2).

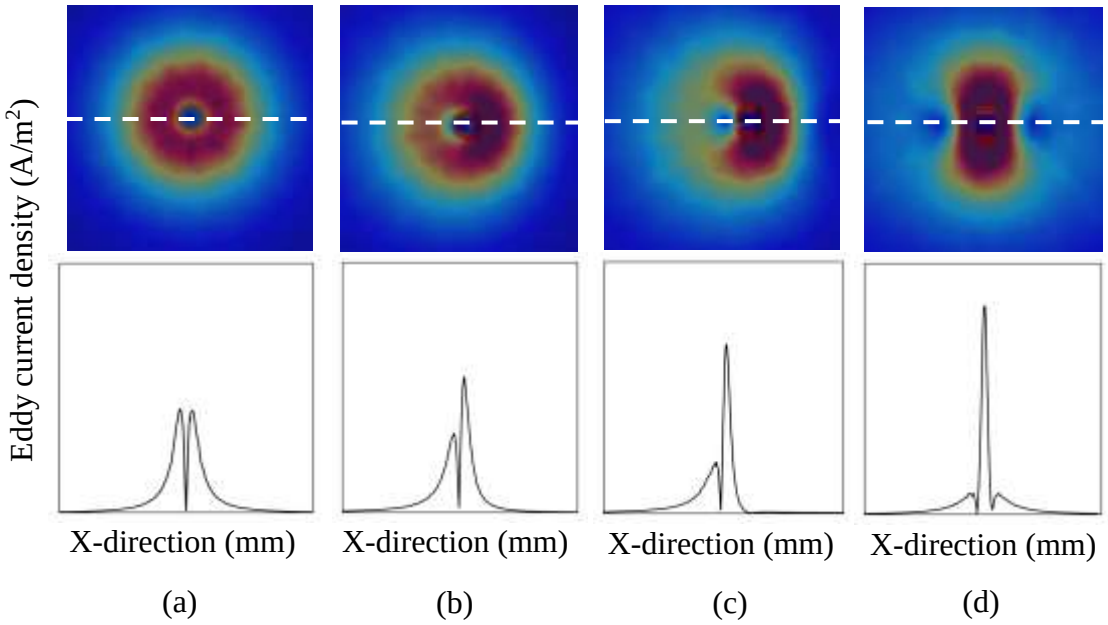

Figure 2.11 Eddy current distribution on a steel plate for different tilt angles of the probe: (a) θ = 0°, (b) θ = 30°, (c) θ = 60°, and (d) θ = 90°.

2.4.3 Calibration and selection of excitation frequency

Each probe was calibrated using steel plates of thickness 5, 6, 7, 8, 9, and 10 mm, while varying the lift-offs at an increment of 0.5mm, from 0 to 5mm, for excitation frequencies of 0.1, 1, 10, 20, 30, 50, 100, and 1000 kHz. Then, as explained in section 2.2.3, from the log-log graph of detected voltage versus frequency for different plate thicknesses at a constant lift-off, the excitation frequency for each probe was determined. It was found that at an excitation frequency of 10 kHz, the influence of thickness on the detected voltage becomes negligible for all the probes considered in the present study. The use of such higher frequency of 10 kHz, with a sampling rate of 10,000 samples per second results in minimal data acquisition time as well. Hence, the lift-off estimation curves were constructed and all the numerical simulations were carried out at an excitation

frequency of 10 kHz.

2.4.4 Effect of approximation of lift-off estimation curve

Next, the importance of approximation of lift-off estimation curve (section 2.2.4) for accurate estimation of corrosion profile is demonstrated in Figure 2.12 by using the large and small probes, 0degLProbe1 and 0degSProbe2 to trace the triangular notched profile from x = 90 mm to x = 110 mm, as shown in Figure 2.7.

The single-line approximation gives large errors in estimating the profile for both the large and small probes, while the two-line approximation gives a fair estimate for large probe, 0degLProbe1 (Figure 2.12 (a)) but is not satisfactory for small probe, 0degSProbe2 (Figure 2.12 (b)). On the other hand, multi-line approximation gives the best estimate of triangular notched profile for both probes. Hence, multi-line approximation is deemed necessary for representing the lift-off estimation curve.

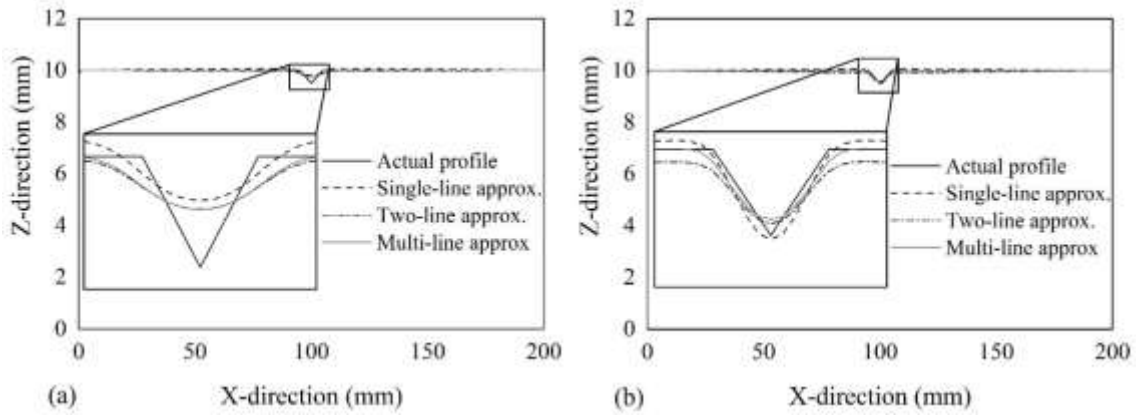

Figure 2.12 Effect of approximation of the lift-off estimation curve by using (a) 0degLProbe1 and (b) 0degSProbe2 in estimating the triangular notched profile.

2.4.5 Effect of geometric parameters on the estimation accuracy

2.4.5.1 Coil height

Four large probes were used to estimate the triangular notched profile as shown in Figure 2.13. The zero-degree tilted probes, 0degLProbe1 and 0degLProbe2 are not susceptible to the change in coil height whereas the ninety-degree tilted probes, 90degLProbe1 and 90degLProbe2, showed high sensitivity to the coil height reduction and gave much better estimation of both the profiles when the coil height was smaller.

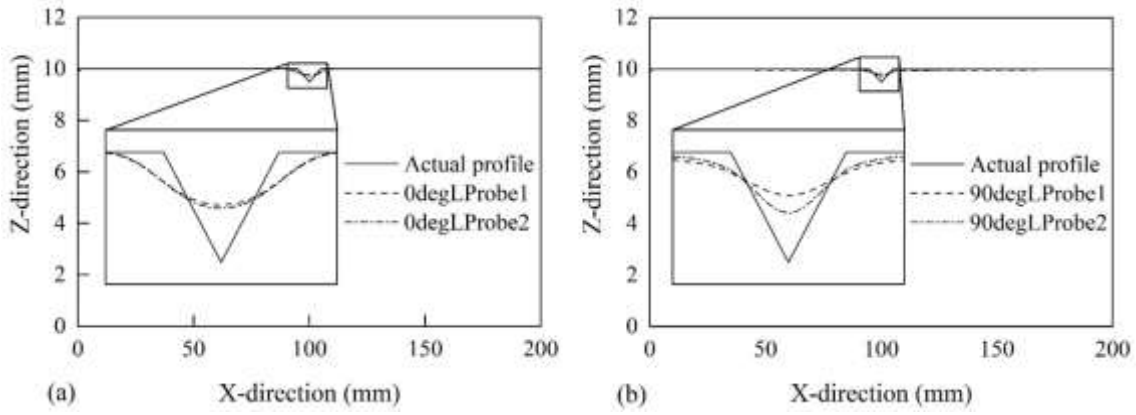

Figure 2.13 Effect of coil height in the estimation of the triangular notched profile for large probes with tilt angle: (a) $\theta = 0°$ and (b) $\theta = 90°$.

2.4.5.2 Coil diameter

Three $\theta = 0°$ and three $\theta = 90°$ probes were used to investigate the effect of coil diameter on the estimation accuracy of triangular notched profile. Figure 2.14 shows significant increment of accuracy on reducing the coil diameter from 10mm (0degLProbe1 and 90degLProbe1) to 4mm (0degSProbe1 and 90degSProbe1). Nonetheless, further reduction in the coil diameter from 4 mm to 2 mm (0degSProbe2 and 90degSProbe2) showed only slight improvement in the estimation,

and further reduction in the coil diameter is assumed not to give any considerable rise in the estimation accuracy. Hence, two probes with the smallest coil diameter and height but different tilt angles, 0degSProbe2 and 90degSProbe2, were further evaluated for tilt angle.

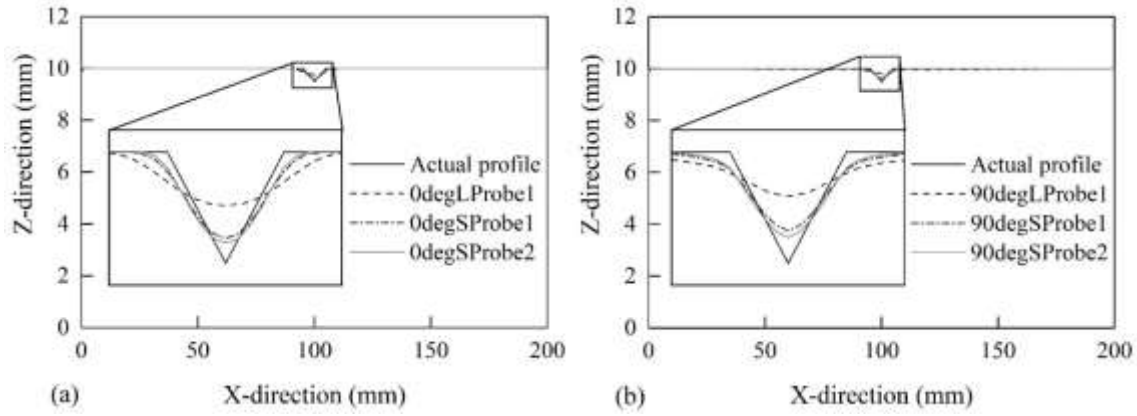

Figure 2.14 Effect of coil diameter in the estimation of the triangular notched profile for probes with tilt angle: (a) $\theta = 0°$ and (b) $\theta = 90°$.

2.4.5.3 Coil diameter to height ratio

Before evaluating for tilt angle, the effect of coil diameter to height ratio was also examined by employing all eight probes in estimating the triangular notched profile. Figure 2.15 (a) shows that 0degLProbe1 gives better estimation of the shape and apex of the notch than 90degLProbe1, whereas 90degLProbe2 estimates the triangular notched profile better than 0degLProbe2 (Figure 2.15 (b)).

Hence, coil diameter to height ratio plays an important role in the performance of large probes, the influence of which however diminishes as the probe gets smaller (Figure 2.16). For both sets of $\theta=0°$ (0degSProbe1 and 0degSProbe2) and $\theta=90°$ (90degSProbe1 and 90degSProbe2) probes, the former estimate shape and apex of triangular notch better than the latter.

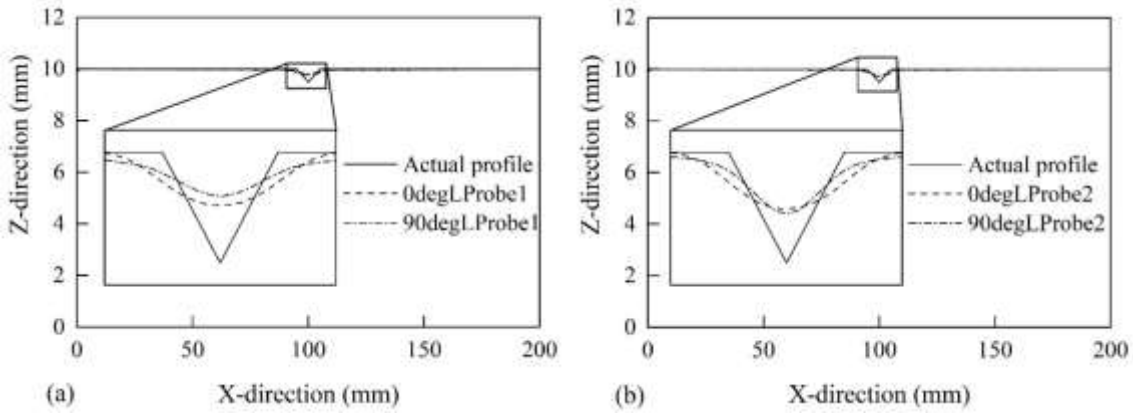

Figure 2.15 Effect of coil diameter to height ratio in the estimation of the triangular notched profile for large probes: (a) 0degLProbe1 and 90degLProbe1, and (b) 0degLProbe2 and 90degLProbe2.

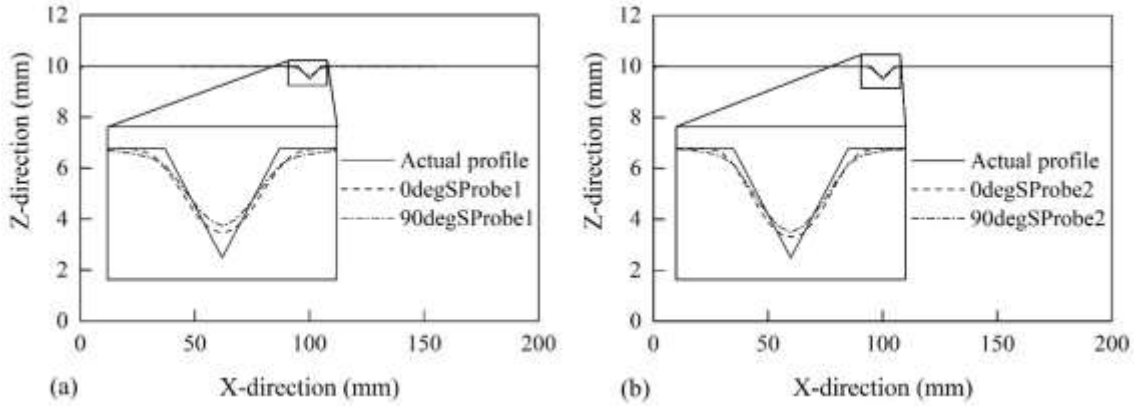

Figure 2.16 Effect of coil diameter to height ratio in the estimation of the triangular notched profile for small probes: (a) 0degSProbe1 and 90degSProbe1, and (b) 0degSProbe2 and 90degSProbe2.

2.4.5.4 Tilt angle of the probe

It can be deduced from Figures 2.13, 2.15, and 2.16 that tilt angle governs the estimation accuracy

of the probe. Also, from Figure 2.16 (b), the θ = 0° probe, 0degSProbe2, gives better approximation of the shape and apex of the triangular notch than its θ = 90° counterpart, 90degSProbe2.

Hence, 0degSProbe2 is obtained as the best optimization of geometric parameters of a reflection probe from the parametric study. It also highlights the importance of optimization of probe geometry for better estimation of detailed corrosion profile over using a commercial probe of fixed dimensions, primarily targeted for general surface inspections.

2.5 Numerical results and discussion

All the numerical simulations are carried out in 3D, AC/DC module of COMSOL Multiphyscis 5.2a. The corrosion profile of a steel plate with and without FRP or Titanium cover is estimated by using the geometrically optimized probe, 0degSProbe2, along y = 10 mm, 15 mm and 20 mm from x = 0 mm to x =100 mm, as shown in Figure 2.17. The 0degSProbe2 probe was maintained at a constant elevation of z = 9.7mm, which is slightly greater than the highest point in the corroded surface, as it moves above the steel plate without cover. For the corroded steel plate with the cover, the probe was kept at a constant elevation of z = 10 mm plus the thickness of the cover, where 10mm is assumed as the initial thickness of the steel plate prior to corrosion.

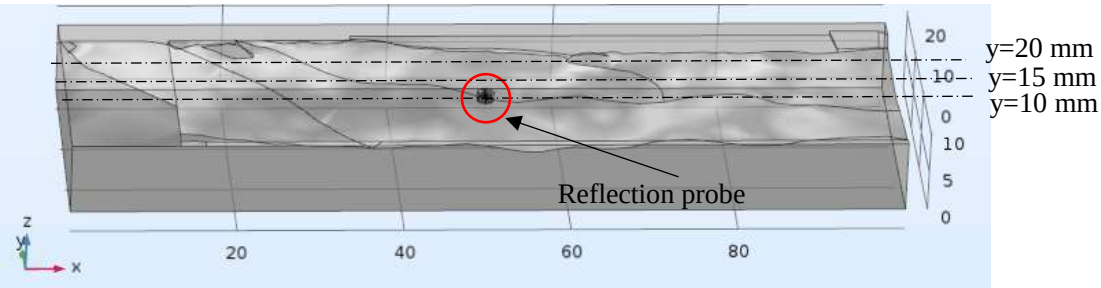

Figure 2.17 Numerical model of the corroded steel plate, the dotted lines showing the profiles traced along y = 10, 15, and 20 mm.

First, the merit of geometric optimization of probe over the use of commercial probe of as is manufactured dimensions is distinguished by using corresponding, representative probes 0degSProbe2 and 0degLProbe1 to estimate the corrosion profile of the corroded steel plate. Then, the corrosion profiles of the plate without protective cover are estimated by 0degSProbe2 probe along y = 10 mm, 15 mm and 20 mm. As a comparison of estimation accuracy, the profiles estimated by 90degSProbe2 probe are also provided, whereby the reduced edge effect is observed. Finally, the corrosion profiles of the steel plate with protective FRP or Titanium covers estimated by 0degSProbe2 probe is presented.

2.5.1 Comparison of geometrically optimized and commercial probes

The enlarged view of the corrosion profiles estimated by 0degLProbe1 and 0degSProbe2 representative of commercial and geometrically optimized probes, respectively are shown adjacent to the full-size, actual corrosion profile estimated by laser displacement meter at y = 10 mm (Figure 2.18 (a)) in Figure 2.18 (b).

Furthermore, for quantitatively evaluating the accuracy of estimation, graphs of actual values obtained from laser displacement meter versus estimated values by 0degLProbe1 and 0degSProbe2 probes are plotted in Figures 2.18 (c) and (d), respectively, and the percentage average error are also shown. It can be seen that the error reduced from 3.6% to 1.44% from 0degLProbe1 to 0degSProbe2 and the latter gives better estimation of the actual profile. Hence, geometric optimization of probe is deemed prudent for better estimation of detailed corrosion profile.

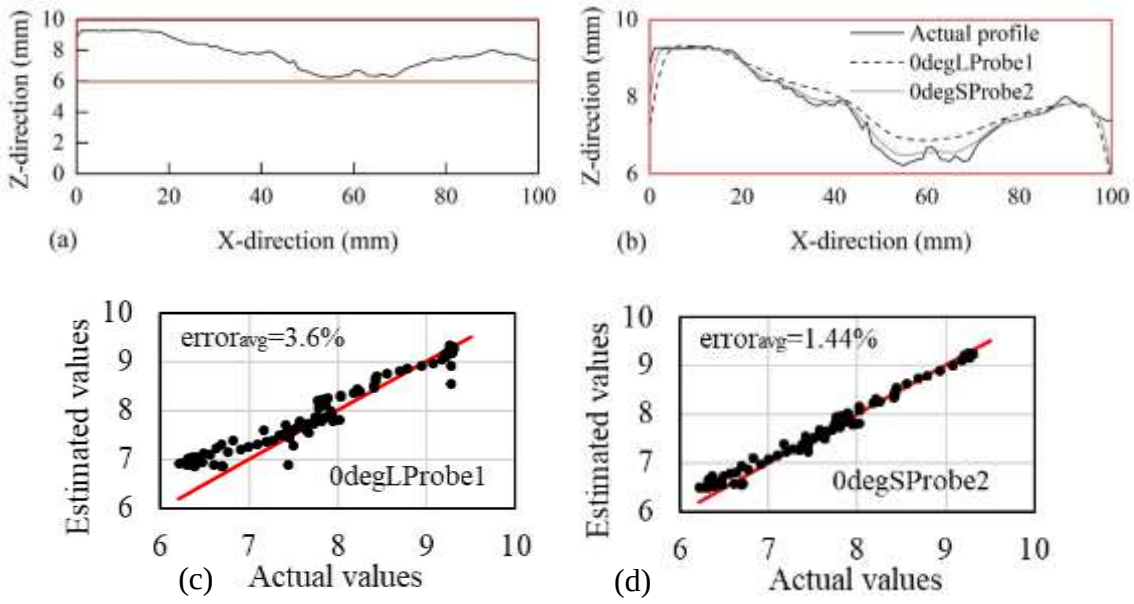

Figure 2.18 (a) Corrosion profile obtained by laser displacement meter, (b) Enlarged view of the corrosion profiles estimated by commercial probe, 0degLProbe1 and optimized probe, 0degSProbe2, and plot of actual versus estimated values by (c) 0degLProbe1 and (d) 0degSProbe2, respectively, at y = 10 mm.

2.5.2 Corrosion profile of steel plate without protective cover

2.5.2.1 0degSProbe2

Figure 2.19 presents the enlarged view of corrosion profiles estimated by 0degSProbe2, adjacent to the full-scale, actual profiles along y = 10, 15 and 20 mm. The estimated profiles follow the actual profiles closely except for the edges, where the probe is inherently subjected to the edge effect caused by the distortion of eddy current flow at the edges. In addition, the percentage average errors shown in the graphs of actual versus estimated values were found to be 1.44%, 1.6% and 1.68%, respectively for y =10, 15 and 20 mm, respectively (Figure 2.20), indicating that the corrosion profile is estimated with good accuracy.

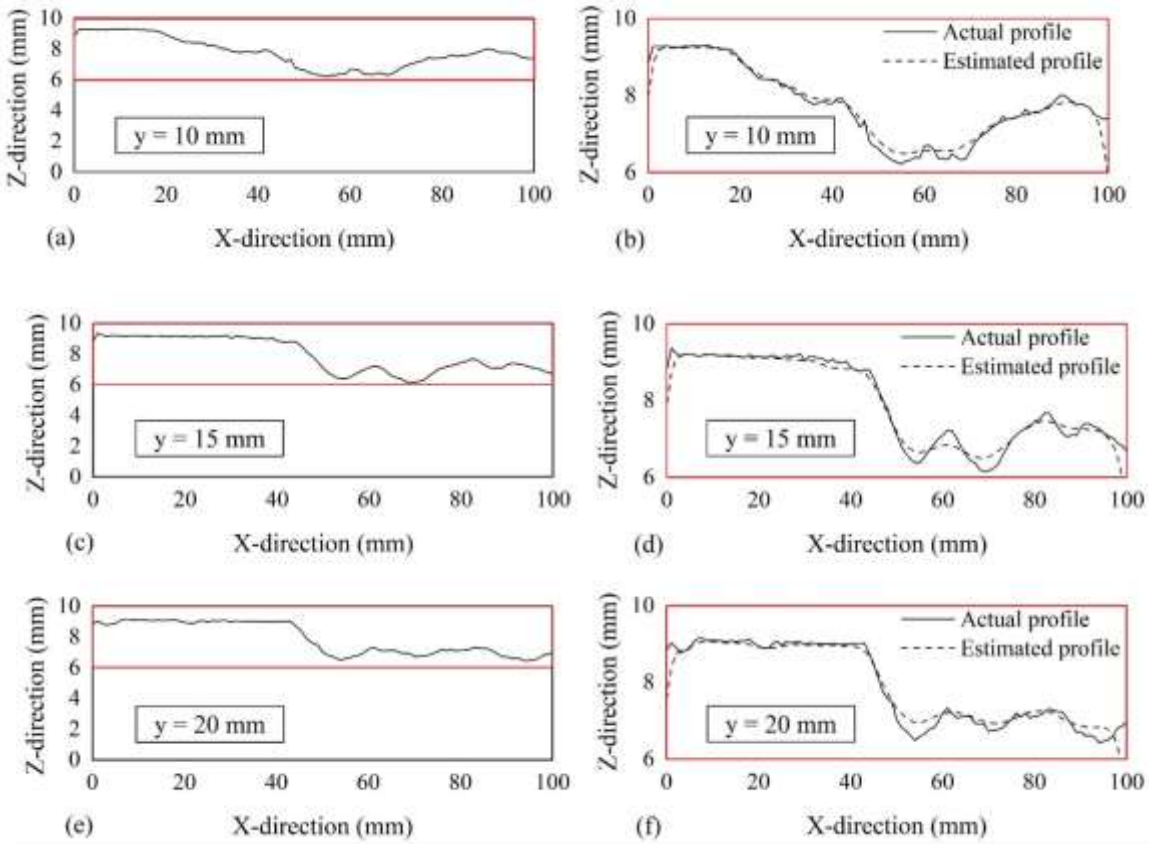

Figure 2.19 Full-size corrosion profile of the steel plate at (a) y = 10 mm, (c) y = 15 mm, and (e) y = 20 mm obtained by laser displacement meter and enlarged view of the corrosion profile estimated by 0degSProbe2 at (b) y = 10 mm, (d) y = 15 mm, and (f) y = 20 mm.

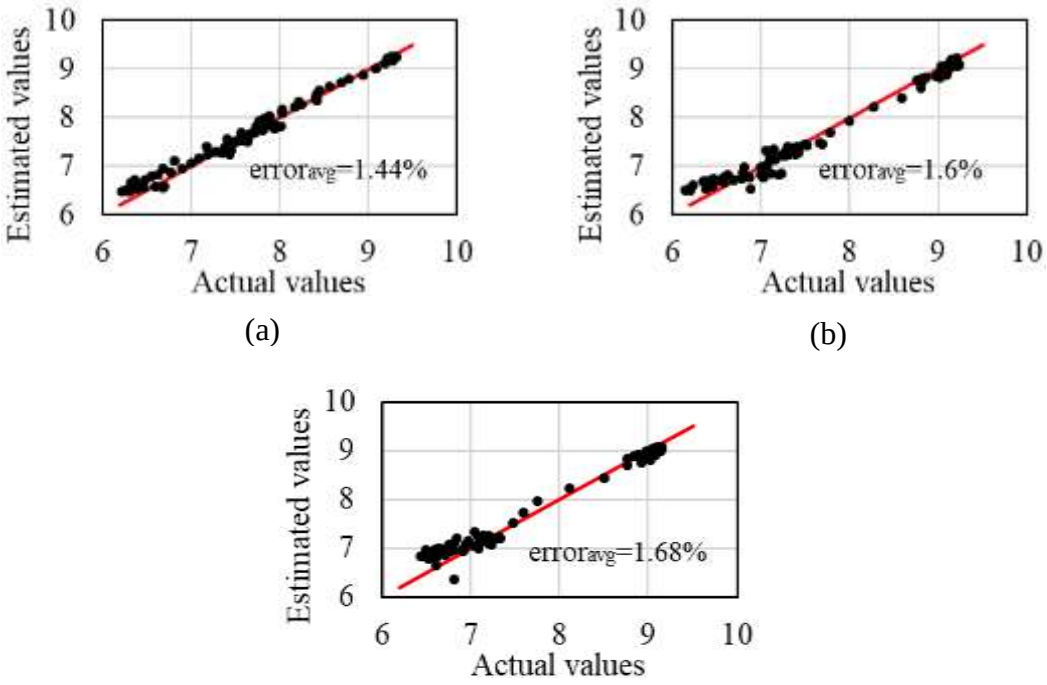

Figure 2.20. Plot of actual versus estimated values of the corrosion profile of the steel plate by 0degSProbe2 at (a) y = 10 mm, (b) y = 15 mm, and (c) y = 20 mm.

2.5.2.2 90degSProbe2

The magnified corrosion profiles estimated by 90degSProbe2 probe along y = 10, 15, and 20 mm with a comparison to 0degSProbe2 probe are shown in Figure 2.21, adjacent to the full-size, actual profiles. The percentage average errors in the actual versus estimated values at y = 10, 15, and 20 mm were found to be 2.09%, 2.06%, and 1.86%, respectively (Figure 2.22). Hence, 90degSProbe2 probe also gives good estimate of the corrosion profiles albeit lesser accurate than 0degSProbe2.

However, the edge effect is much less in 90degSProbe2 than 0degSProbe2, which is due to the smaller distortion of eddy current at the edge of a uniform steel plate in $\theta = 90°$ probe than its $\theta = 0°$ counterpart (Figure 2.23). Hence, 90degSProbe2 can also be used for fair estimation of

corrosion profile if reduced edge effect is preferred over lesser estimation accuracy.

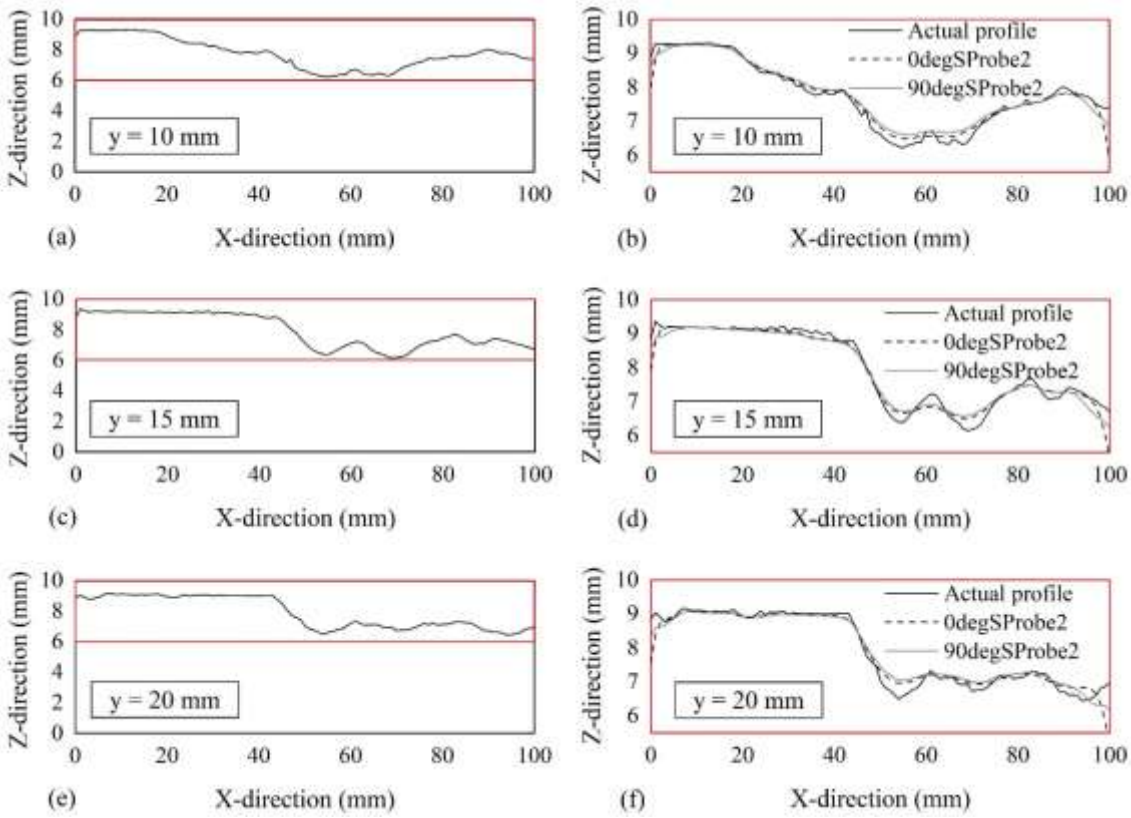

Figure 2.21 Full-size corrosion profile of the steel plate at (a) y = 10 mm, (c) y = 15 mm, and (e) y = 20 mm obtained by laser displacement meter and magnified view of the corrosion profile estimated by 90degSProbe2 with a comparison to 0degSProbe2 at (b) y = 10 mm, (d) y = 15 mm, and (f) y = 20 mm.

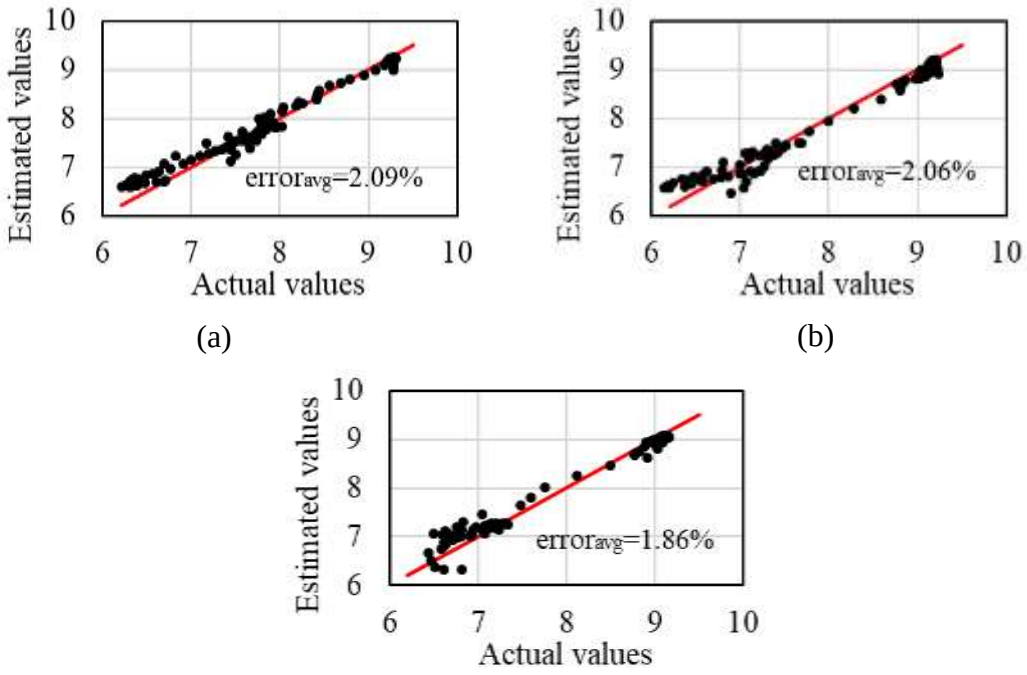

Figure 2.22 Plot of actual versus estimated values of the corrosion profile of the steel plate by 90degSProbe2 at (a) y = 10 mm, (b) y = 15 mm, and (c) y = 20 mm.

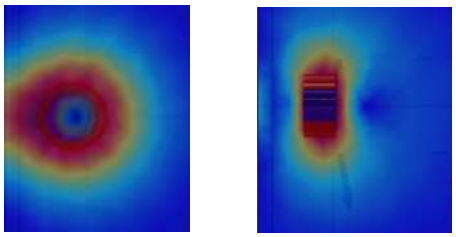

Figure 2.23 Distortion of eddy current at the edge of a uniform steel plate by (a) 0degSProbe2 and (b) 90degSProbe2 probes.

2.5.3 Corrosion profile of steel plate with protective cover

2.5.3.1 FRP cover

First, calibration was conducted using uniform steel plates with 2.5 mm thick FRP cover, whereby a new lift-off estimation curve is obtained. Then, the corrosion profiles were traced along y = 10, 15, and 20 mm by moving 0degSProbe2 over the FRP cover. Figure 2.24 shows the enlarged, estimated corrosion profiles with and without FRP cover, adjacent to the corresponding full-size, actual profiles. The percentage average errors for estimated and actual values of the corrosion

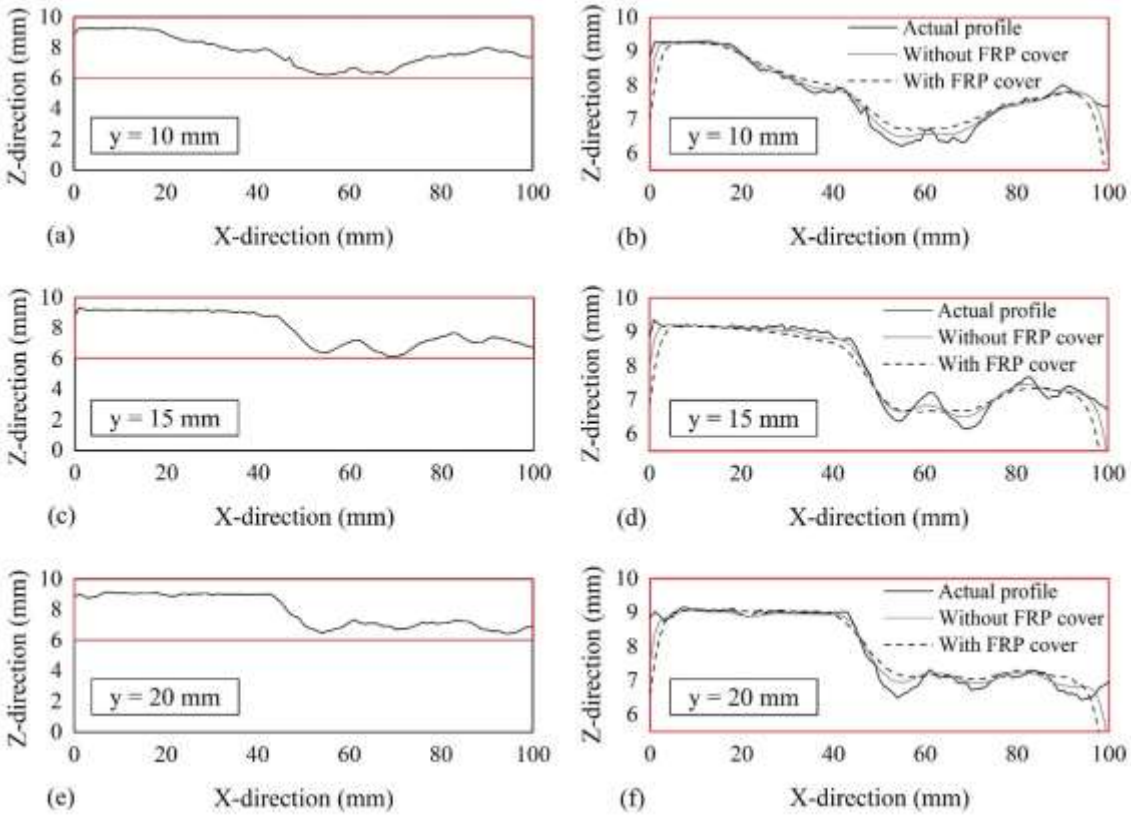

Figure 2.24 Full-size corrosion profile of the steel plate at (a) y = 10 mm, (c) y = 15 mm, and (e) y = 20 mm obtained by laser displacement meter and enlarged view of the corrosion profile with and without FRP cover estimated by 0degSProbe2 at (b) y = 10 mm, (d) y = 15 mm, and (f) y = 20 mm.

profiles at y =10, 15, and 20 mm are 2.63%, 2.73%, and 2.22%, respectively (Figure 2.25). Although the accuracy is slightly diminished in presence of FRP cover, a reasonable estimation of the corrosion profile beneath the cover can still be obtained without having to remove the cover.

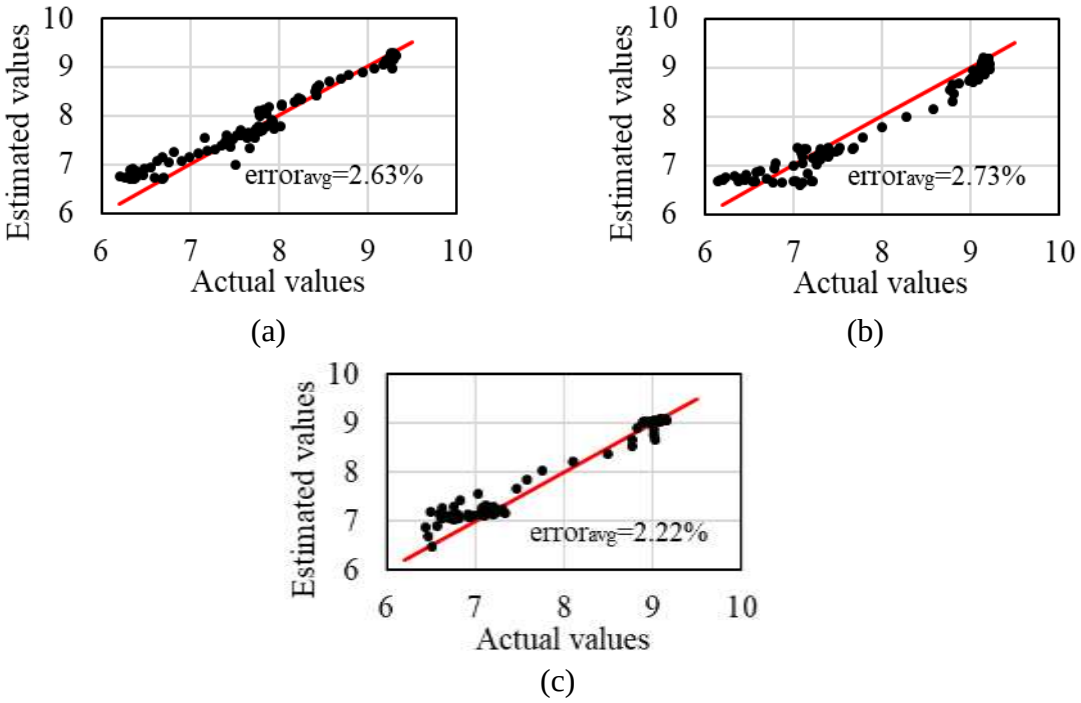

Figure 2.25 Plot of actual versus estimated values of the corrosion profile of the steel plate beneath the FRP cover by 0degSProbe2 at (a) y = 10 mm, (b) y = 15 mm, and (c) y = 20 mm.

2.5.3.2 Titanium cover

Similarly, for the case of Titanium (Ti) cover, a new lift-off estimation curve was constructed through calibration of uniform steel plates with 1 mm thick Ti cover. Although Titanium is a conducting material, the effective penetration depth of the eddy current in Ti cover is more than the thickness of the cover. As a result, the eddy current penetrates through the cover and is induced in the steel plate below as illustrated in Figure 2.26.

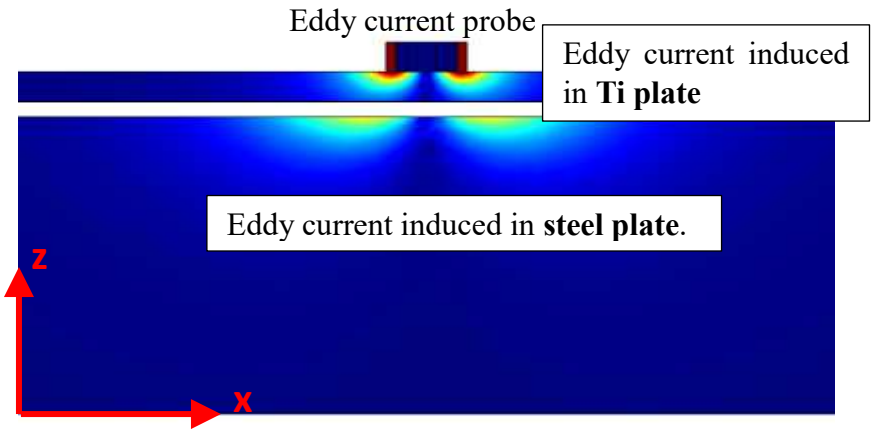

Figure 2.26. Induction of eddy current in steel plate beneath the Ti cover.

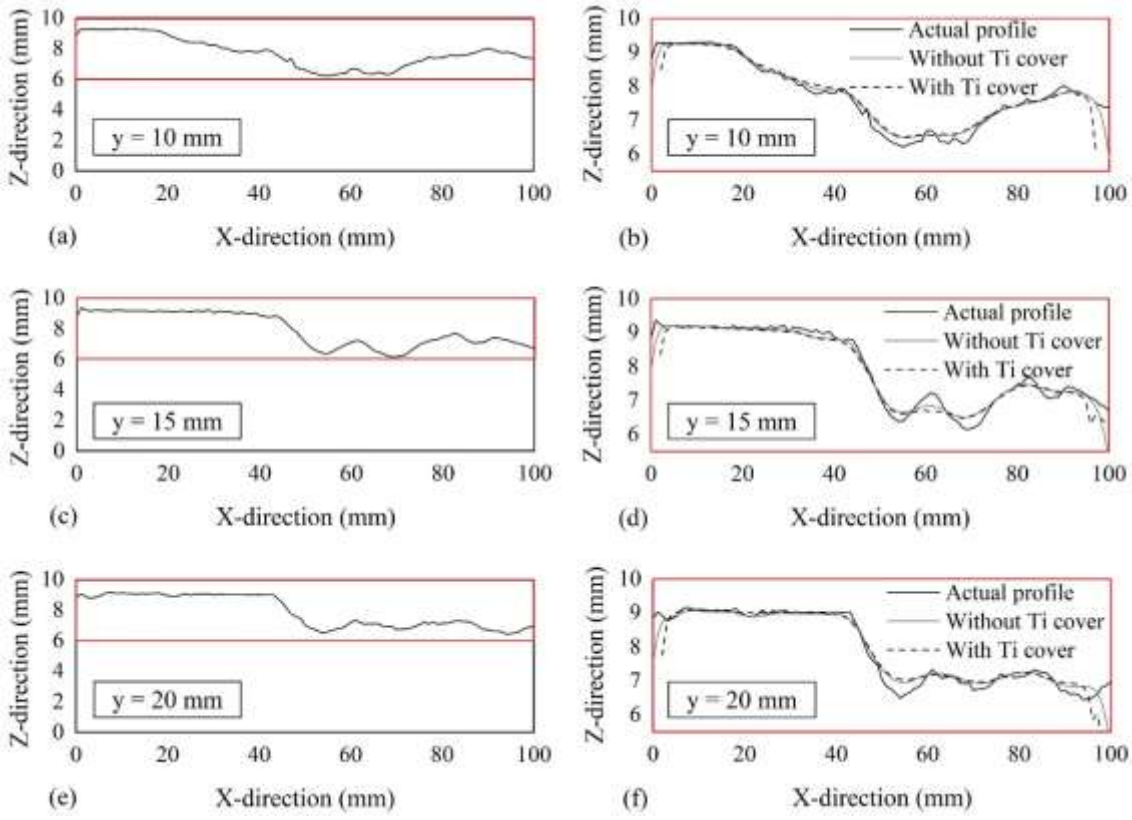

Figure 2.27 Full-size corrosion profile of the steel plate at (a) y = 10 mm, (c) y = 15 mm, and (e) y = 20 mm obtained by laser displacement meter and expanded view of the corrosion profile with and without Ti cover estimated by 0degSProbe2 at (b) y = 10 mm, (d) y = 15 mm, and (f) y = 20 mm.

The corrosion profiles were then estimated by moving the probe, 0degSProbe2, over the Ti cover along y = 10, 15, and 20 mm. Figure 2.27 shows the expanded, estimated corrosion profiles with and without Titanium cover, adjacent to the corresponding full-size, actual profiles. The percentage average errors in the plot of estimated versus actual values of the corrosion profiles at y = 10, 15, and 20 mm are 1.73%, 1.9%, and 1.7%, respectively, indicating good estimation of the profile (Figure 2.28).

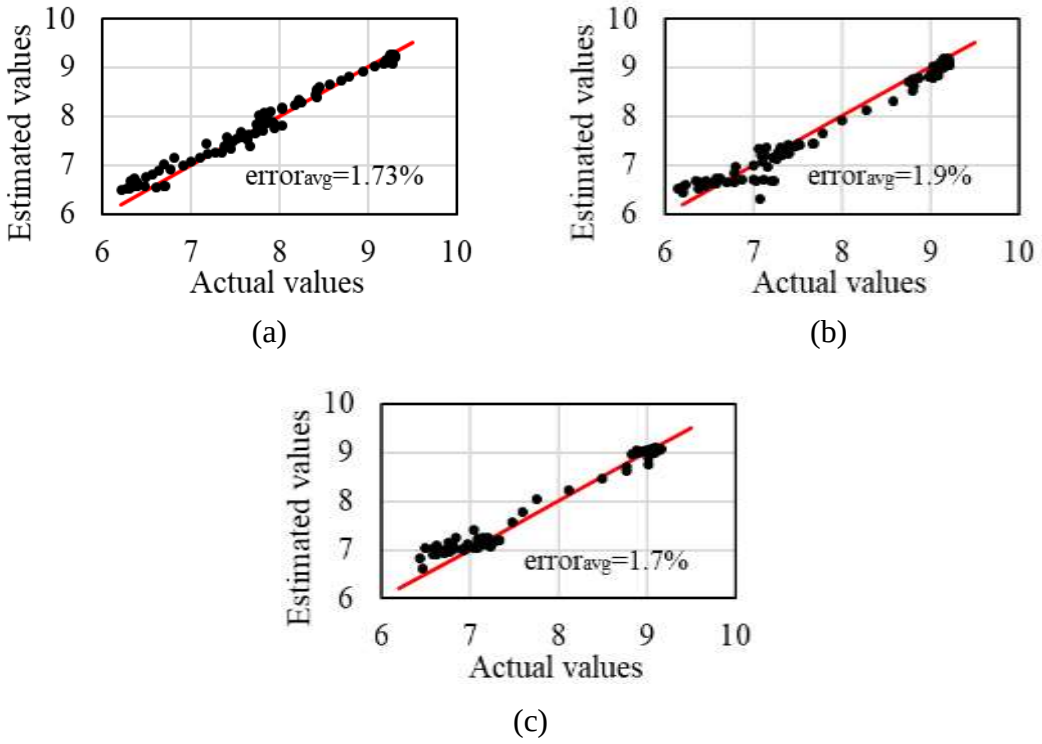

Figure 2.28. Plot of actual versus estimated values of the corrosion profile of the steel plate beneath the Ti cover by 0degSProbe2 at (a) y = 10 mm, (b) y = 15 mm, and (c) y = 20 mm.

2.5.4 Corrosion severity evaluation

The estimation of the corrosion profiles can then be further used in the evaluation of severity of the corrosion of the steel plate as shown schematically in Figure 2.29 (a). For an un-corroded,

steel, the distance to the healthy steel layer is equal to the nominal distance, shown by green block, while the distance to the healthy layers increase due to the loss of material due to corrosion and a distribution is seen showing the spread of corrosion. This can be used in evaluating the severity of corrosion as light, moderate, and severe as demonstrated as follows. A corrosion severity evaluation histogram is plotted as shown in Figure 2.29 (b) for the collective data points of three corrosion profiles y =10 mm, 15 mm, and 20 mm to observe the distribution of corrosion, based on the distance to the healthy layer.

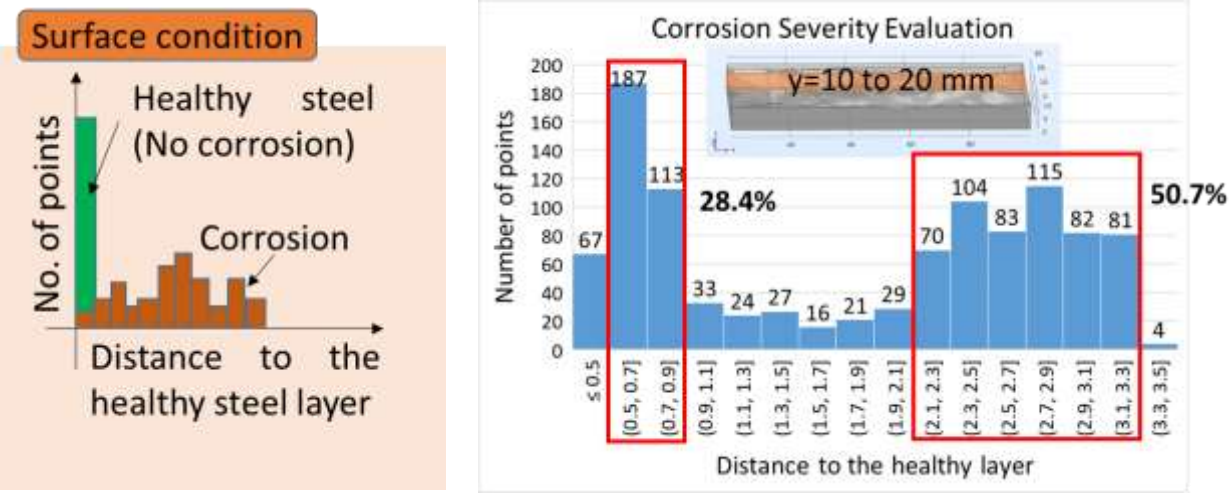

(a) (b)

Figure 2.29 (a) Schematic of un-corroded and corroded surface represented in the histogram, and (b) Corrosion severity evaluation histogram showing the corrosion distribution of the given steel plate.

It can be seen that although the highest loss of material, equivalent to the largest distance to the healthy layer is in the range of 0.5-0.9mm loss, it comprises only 28.4 % of the total. On the other hand, 50.7 % of total of the distance to the healthy layer comprises the high values of corrosion from 2.1 – 3.3 mm. Hence, it can be concluded that severe corrosion has occurred in the given corroded steel plate.

2.6 Summary

In the present study, a high frequency eddy current method was used to estimate the corrosion profile of a steel plate directly from the lift-offs, independent of the varying thickness of the corroded plate. Eight reflection probes were employed for the parametric study of the influence of geometric parameters namely coil height, diameter, their ratio, and tilt angle of the probes on the estimation accuracy of a triangular notched profile, representative of corrosion. The three-dimensional numerical simulations were carried out in COMSOL Multiphysics 5.2a, yielding a geometrically optimized probe, 0degSProbe2, which was then used to trace the corrosion profiles of a steel plate with and without FRP or Titanium covers along y = 10, 15, and 20 mm. The estimated profiles showed good agreement with the actual corrosion profile obtained by laser displacement meter. Furthermore, corrosion severity evaluation histogram constructed from the estimated corrosion profiles is used to determine the severity of corrosion as light, moderate, or severe.

The following findings can be summarized from this chapter:

(1) Multi-line approximation of the non-linear lift-off estimation curve is deemed necessary in order to preclude the accuracy reduction in estimation of corrosion profile.
(2) Coil height, diameter and tilt angle of the probes mainly govern the estimation accuracy of the probe. The influence of coil diameter to height ratio was prominent in larger probes but became negligible as the probes became smaller.
(3) The geometrically optimized, reflection probe, 0degSProbe2 probe gives good estimation of the corrosion profiles except at the edges owing to the edge effect. On the other hand, 90degSProbe2 probe was found less susceptible to the edge effect, albeit lesser accurate

than 0degSProbe2. Hence, 90degSProbe2 can also be used for estimation of the corrosion profile with slight compromise in the accuracy if lower sensitivity to edge effect is desired.

(4) In addition, fair estimation of the corrosion profiles beneath protective FRP or Titanium cover was achieved by 0degSProbe2 probe. This proves highly convenient in field inspections of covered steel members, saving time and labor.

(5) Moreover, corrosion severity evaluation histogram constructed from the estimated corrosion profile offers a convenient way to evaluate whether the corrosion is light, moderate, or severe.

Hence, a methodology to conduct corrosion profile estimation of a corroded steel plate without having to remove the outer protective covering was devised and its applicability was verified numerically with comparison to the corrosion profiles of the actual steel specimen obtained from laser displacement meter. In addition, the importance of selection of method of approximation of the lift-off estimation curve and a deeper understanding of the optimization of the probe geometry for accuracy was gained, while corrosion severity evaluation histogram was obtained as a tool to evaluate the degree of corrosion.

Chapter 3. Eddy Current Based Stress Measurement on a Steel Plate using Phase Diagram

This chapter investigates the determination of the stress change by using eddy current testing as a new, viable approach applicable for structural health monitoring of steel structural members. The effect of change in stress in a steel plate on the eddy current response is evaluated through three-dimensional numerical simulations carried out COMSOL Multiphysics 5.2a. A reflection probe, comprising of an outer exciting coil and an inner detecting coil, is used to characterize the eddy current indices - real, imaginary, and absolute voltages, and phase with respect to the change in relative permeability (representative of stress), lift-off, exciting frequency, and probe size. Phase diagram is then devised as a new concise method of simultaneously representing the effects of relative permeability and lift-off at an excitation frequency, which is further used in the selection of suitable probe size and excitation frequency for eddy current based stress measurement.

3.1 Overview

In this chapter, the stress change evaluation is presented as a new, viable approach in the structural health monitoring of the steel structures in service, for which a suitable method to conduct eddy current based stress measurement is explored. To characterize the eddy current response, three-dimensional numerical simulations are carried out for a steel plate subjected to uniaxial tensile stress, using a reflection probe, in the AC/DC module of general-purpose FE software, COMSOL Multiphysics 5.2a. For the simplicity of formulation of the numerical model, only applied stresses have been taken into account in the present study to represent the change in stress state. It is to be noted that owing to the limitations of the module, the direct of effect of stress on the eddy current signal could not be modelled, and the effect of relative permeability, which is highly dependent on stress, is modelled instead, as in Schoenekess et al. (2007) [74]. In addition, the robustness of eddy current based stress measurement is evaluated by verifying that the eddy current indices can detect the concurrent changes in the relative permeability in multiple directions. Then, the effects of other influential eddy current parameters such as lift-off, excitation frequency, and probe size are investigated, which incurred a number of graphs for the evaluation of eddy current response. Therefore, Phase Diagram incorporating the simultaneous effect of relative permeability and lift-off, at a particular excitation frequency for a specific probe, in a single graph has been proposed as a new, concise way of ascertaining the effects of influential eddy current parameters. Moreover, it was used in the selection of suitable excitation frequency and probe size in the eddy current based stress measurement.

3.2 Stress measurement using eddy current

The physical phenomenon that enables eddy current to detect the change in stress in a steel plate

is explained first, followed by the evaluation of influential parameters affecting the eddy current response that are to be investigated in the present study. Then, the eddy current indices that can be used in the characterization for stress measurement are discussed.

3.2.1 Working principle

Eddy current testing is based on the principle of Faraday's law of electromagnetic induction, where an alternating current passed through a coil generates varying magnetic field, and induces eddy currents on a conducting material when brought to its vicinity. Any changes in the test specimen such as presence of cracks, change in thickness, electrical conductivity, and magnetic permeability affect the eddy current response, and therefore make it possible to detect or quantify these changes.

Stress measurement using eddy current is based on the Villari effect or inverse magnetostrictive effect exhibited by the magnetic materials, whereby the applied stress causes change in the magnetic permeability of the material, which in turn affects the magnetic flux penetrating the material thus changing the eddy current response [46, 68, 69]. The magnetic materials are comprised of many magnetic domains (Figure 3.1 (a)), the magneto-elastic energy of which are affected by the stress, resulting in the domain wall movement and thus the stress-induced domain reorientation as shown schematically in Figure 3.1 (b) [69].

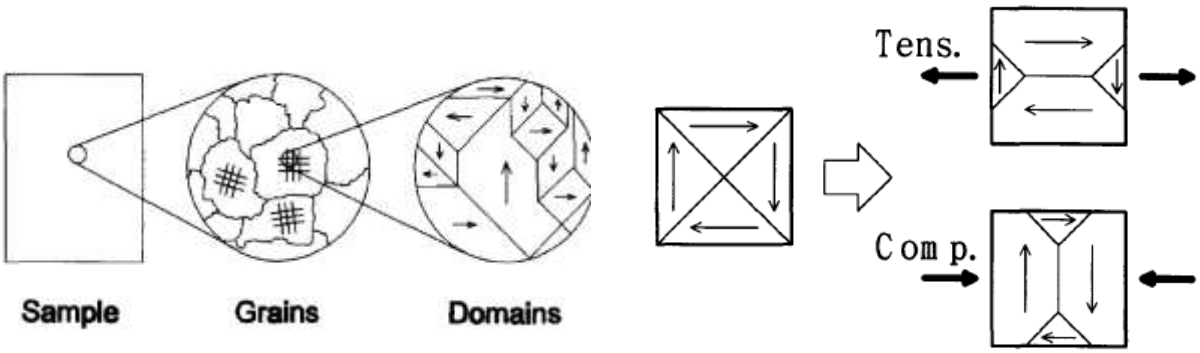

(a) (b)

Figure 3.1 (a) Magnetic domains, (b)Domain reorientation due to applied stress[69].

This can also be represented in the equation for linear magnetostriction [70, 84] shown below:

$$S = s^{H}\Psi + dH \tag{3.1a}$$

$$B = d^{*}\Psi + \mu^{\Psi}H \tag{3.1b}$$

where, S and Ψ are strain and stress, and B and H are magnetic flux density and the applied magnetic field, respectively. The magneto-mechanical coupling between applied magnetic field and induced strain (equation 3.1a) or applied stress and change in magnetic flux density (equation 3.1b) are accounted for by piezo-magnetic cross coupling coefficients, d and d^{*}. Here, s^{H} is the compliance matrix at constant magnetic field strength, and $\mu^{\Psi}$is the magnetic permeability at constant stress. It can be seen from equation 3.1b that the change in stress affects the magnetic permeability and the magnetic flux penetrating the test material, which in turn affects the eddy current response.

This has also been experimentally verified by Jiles et al. (2002) [85], from the changes in hysteresis loop in application of stress as shown below in Figure 3.2; the effect of tensile stress are exactly the opposite. It is seen that the application of stress affects the magnetic permeability of the material, given by the slope of the relationship between B and H. The magnetic permeability increases as the tensile stress increases, i.e. positive magnetostriction. This is the qualitative relationship between stress and permeability for a positive magnetostrictive material like steel. Hence, the increase in magnetic/relative permeability can be used to denote the increase in applied tensile stress.

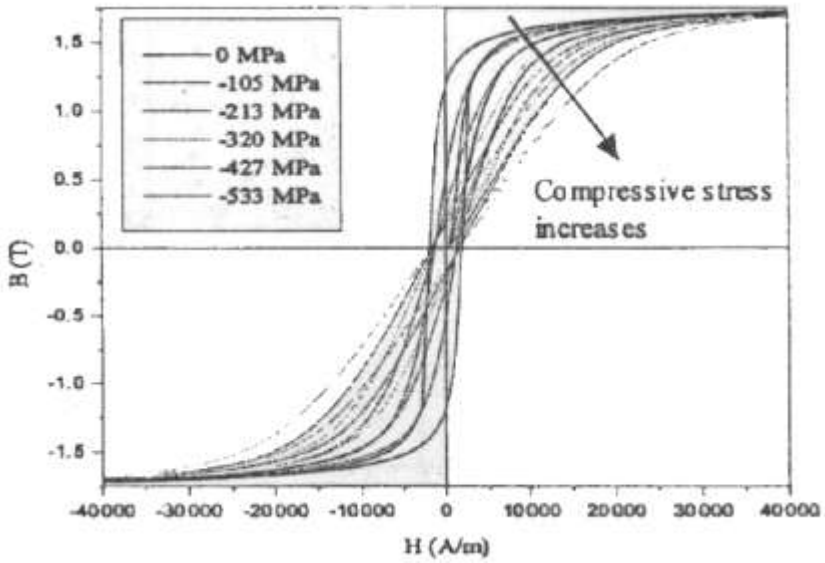

Figure 3.2 Hysteresis showing the change in magnetic permeability due to applied stress.

However, the quantitative relationships between the magnetic/relative permeability and stress are available in the literature only for Iron-Cobalt alloy [46], electrical steel [86], Terfenol-D [87], etc., as shown in Figures 3.3 (a), (b), and (c) respectively. Since these are not applicable for structural steel, the relative permeability has been increased accordingly during the FE simulation to represent the increase in applied tensile stress in the steel plate.

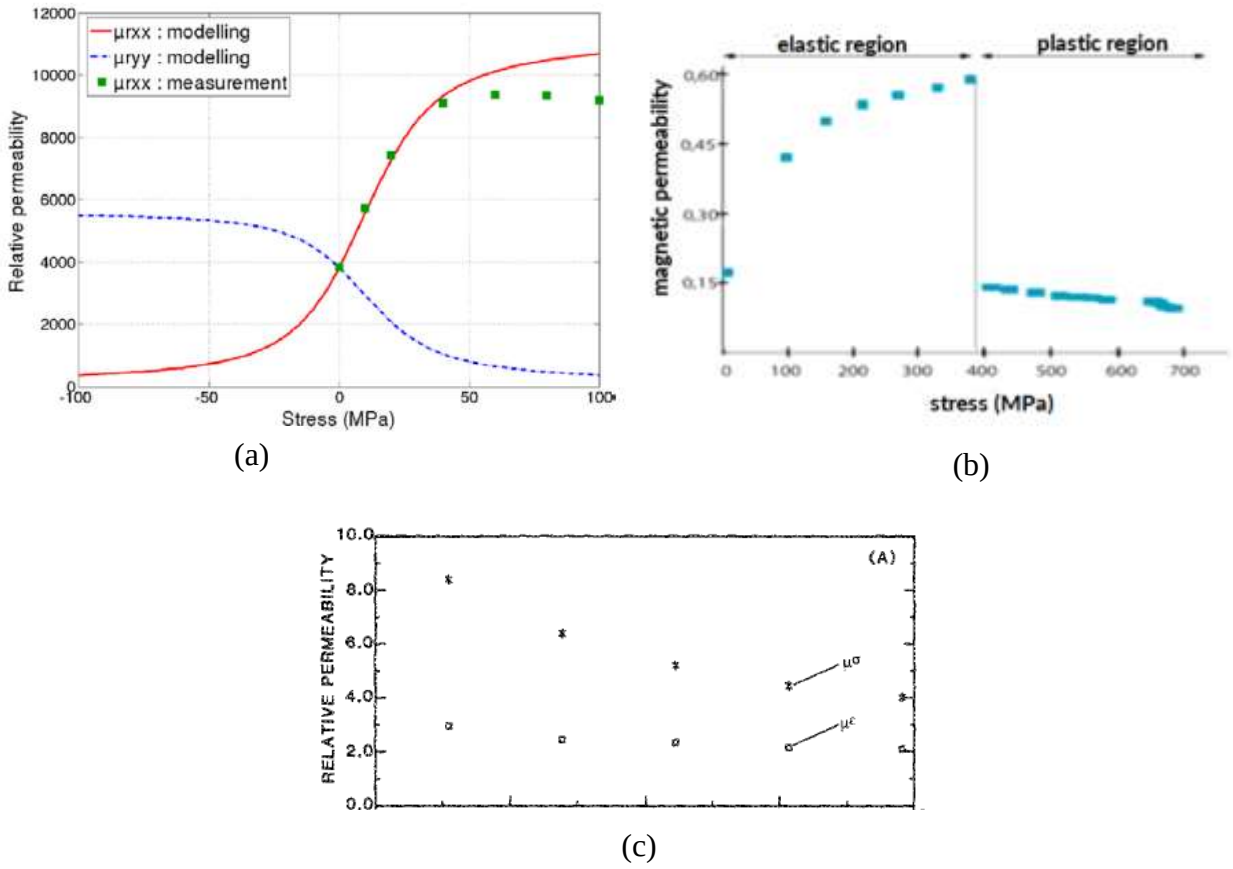

(a) (b)

(c)

Figure 3.3 Quantitative relationships between magnetic/relative permeability and stress for (a) Iron-Cobalt alloy [46], (b) Electrical steel [86], and Terfenol-D [87].

3.2.2 Influential parameters in eddy current based stress measurement

The parameters affecting eddy current response can also be observed in the expression for skin depth, which is the depth below the surface at which the eddy current density decreases to about 1/e or 37% of its surface value [33], and gives an indication of how deep eddy currents can penetrate into the test specimen:

$$\delta = \sqrt{\frac{2}{\mu\omega\sigma}} \tag{3.2}$$

where, δ is the standard penetration depth in meters, σ is the electrical conductivity of test material in S/m, μ is the magnetic permeability of test material in H/m, given by $\mu = \mu_r \mu_0$, where μ_r is the relative permeability and μ_0 is the magnetic permeability of the vacuum ($4\pi x 10^{-7}$H/m) and $\omega = 2\pi f$, where f is the excitation frequency in Hz. The equation 3.2 shows that change in the magnetic permeability or relative permeability affects the depth of penetration of eddy current and alters the eddy current response.

In addition to the relative permeability, excitation frequency, f and electrical conductivity, σ also affect the eddy current response. Although applied stress causes change in both relative permeability and electrical conductivity, the change in electrical conductivity is negligible (<1%) [46]. Hence, only the change in relative permeability due to the applied stress is considered in the present study. The two other parameters that have not been incorporated into the equation for standard depth of penetration but affect the eddy current response are the lift-off, distance between eddy current probe and test specimen, and the probe size. Although miniaturization of the probe has been found to provide better sensitivity in the stress estimation [71], it might not hold true for determining the stress over the corroded surface of a steel girder with large lift-offs. This is because the coupling between the eddy current probe and the test surface decreases as the lift-off increases, consequently reducing the probe's sensitivity. Since probe size affects the strength of eddy current response and sensitivity to lift-off, in addition to the relative permeability and excitation frequency, the effect of lift-off and probe size in the eddy current response are also investigated in the present study.

3.2.3 Eddy current indices

Depending upon the type of eddy current probe considered, varied eddy current indices such as normalized impedance of the coil [46], inductance and resistance of the single coil sensor [71, 72], and change in inductivity [73] have been used to quantify the changes due to stress variation. In the present study, real voltage (V_{real}), imaginary voltage (V_{imag}), absolute voltage (V_{abs}), and phase (θ) obtained from the detecting coil of the reflection probe are used as eddy current indices, which can be expressed as:

$$V_{abs} = \sqrt{V_{real}^2 + V_{imag}^2} \tag{3.3a}$$

$$\theta = \tan^{-1}\left(\frac{V_{imag}}{V_{real}}\right) \tag{3.3b}$$

The variation of each of these eddy current indices with respect to the change in influential parameters namely, relative permeability, lift-off, and excitation frequency are used to characterize the eddy current response. First, the relative permeability is changed only along X-direction to ascertain that the eddy current indices reflect the change and then in both X- and Y- directions to confirm that eddy current indices can detect the change due to variation of relative permeability in multiple directions, as would be expected in real life conditions. Then, the plot of imaginary voltage versus real voltage, hereby termed as Phase diagram, is proposed to depict the simultaneous changes due to relative permeability and lift-off at a particular excitation frequency in a concise way compared to a number of plots for each eddy current index for representing the same amount of information.

3.3 Finite element modeling

The three-dimensional numerical simulations of a steel plate subjected to a uniaxial tensile stress are conducted in the FE software COMSOL Multiphysics 5.2a, the finite element formulation of which would require modeling of two phenomena. Firstly, the inverse magnetostrictive effect should be modeled, where the magnetic permeability of the steel plate in a particular direction is changed due to the application of stress in that direction. Secondly, the eddy current problem of electromagnetic induction should be modeled, which obtains the change in eddy current indices due to the changed magnetic permeability. However, owing to the limitations of the available AC/DC module in the FE software COMSOL Multiphysics 5.2a, the inverse magnetostrictive effect could not be modeled. Nevertheless, as mentioned in section 3.2.1, based on the qualitative relationship between applied stress and relative permeability for a positive magnetostrictive material like steel, the relative permeability values in X-direction are increased to represent the effect of the increasing tensile stress applied in that direction. Therefore, the whole problem is formulated only as the eddy current problem in the frequency domain of the AC/DC module, whereby the effect of change in relative permeability along X-direction, lift-off, excitation frequency, and probe size on the eddy current indices are investigated.

The governing equation solved for eddy current problem of electromagnetic induction is as follows [58]:

$$(j\omega\sigma - \omega^2\varepsilon)A + \nabla \times (\mu^{-1}\nabla \times A) = J_e \qquad (3.4)$$

where, $\omega=2\pi f$ is the angular frequency, f being the excitation frequency of the probe, σ is the electrical conductivity, ε is the relative permittivity, μ is the magnetic permeability of the steel plate, A is the magnetic vector potential, and J_e is the external current density provided by the

exciting coil. The symbol ∇ (nabla operator) denotes the three-dimensional gradient operator, where ∇x denotes the curl operator.

The reflection probe (Figure 2.1) is modeled using two concentric coils – an outer exciting coil and an inner detecting coil, each represented by a homogenized, multi-turn cylindrical coil. Two reflection probes 2D1CH and 10D10CH of 2mm and 10mm diameter respectively have been considered to demonstrate the effect of probe size, and their specifications are given in Table 3.1. Here, ϕ is the diameter of the coil, CH is the coil height, N is the no. of turns in the coil, and the subscripts *ex* and *det* denote exciting and detecting coils, respectively. The size of the computational domain (air) is 300 x 300 x 100 mm (Figure 3.3) and the steel plate made up of carbon steel is 200 mm x 200mm x 10mm, and the boundary condition is imposed such that the tangential component of the magnetic vector potential is zero. The built-in materials *SteelAISI4340, Copper, and Air* are assigned to the steel plate, coils, and air and their material properties are listed in Table 3.2.

Table 3.1 Probe specifications

Probe Name	ϕ_{ex} (mm)	ϕ_{det} (mm)	CH_{ex}(mm)	CH_{det}(mm)	N
2D1CH	2	1	1	1	100
10D10CH	10	6	10	10	1000

Table 3.2 Material properties

Domain	Air	Coils	Steel plate
Relative permeability along X-direction (μ_{rX})	1	1	100 - 200
Relative permeability along Y-direction (μ_{rY})	1	1	100
Electrical conductivity (σ)	0.1	5.998×10^7	4.032×10^6

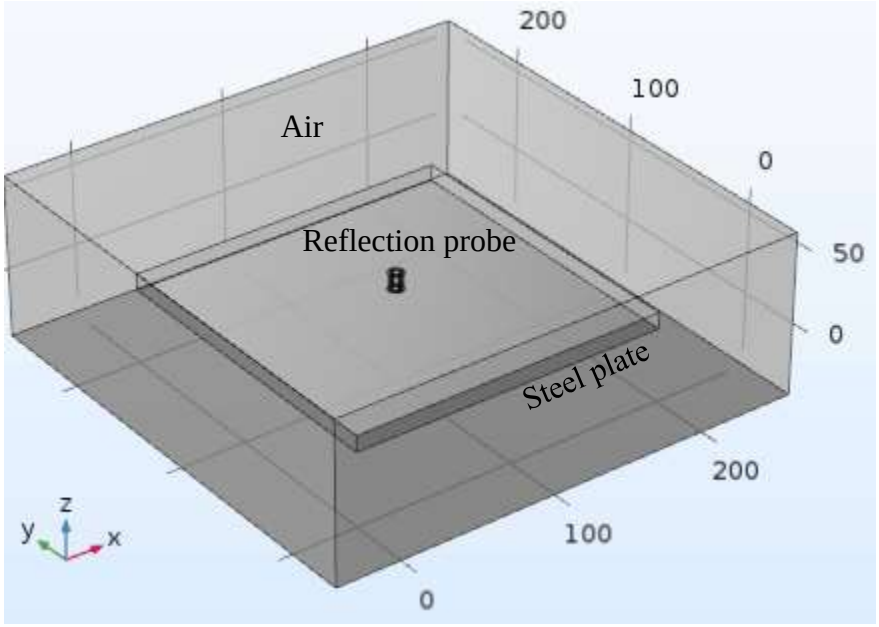

Figure 3.3 Computational domain.

The *Free tetrahedral* mesh with the minimum and maximum element size of 0.1-0.5 mm to 10-40 mm was assigned to the steel plate, and air domain for 2D1CH and 10D10CH probes, respectively. Whereas, a finer mesh with minimum and maximum element sizes of 0.001-0.5 mm to 1-10 mm was assigned to the coils corresponding to the 2D1CH and 10D10CH probes. A very small value of electrical conductivity has been assigned to the air domain in view of numerical stability.

Since uniaxial tensile stress is considered to be applied along X-direction of the steel plate, the relative permeability in X-direction (μ_{rX}) is increased from 100 to 200 at step of 10, while that in Y-direction (μ_{rY}) is kept constant at 100, to determine the effect on eddy current indices due to change in relative permeability. The parametric studies are then conducted for lift-offs of 0, 0.2,

0.6, 0.8, 1, 1.5, 2, 2.5, and 3mm, and excitation frequencies of 0.1, 1, 5, and 10 kHz to determine the effect of lift-off and excitation frequency variation on the eddy current indices

3.4 Numerical results and discussion

Firstly, the effect of change in eddy current indices namely real voltage, imaginary voltage, absolute voltage, and phase due to change in lift-off is evaluated for the smaller reflection probe 2D1CH in order to verify the known behavior of eddy current and the formulation of numerical model. Then, the trend of change of eddy current indices due to changed relative permeability along X-direction is investigated, with illustrations of the change in shape of eddy current distribution. Furthermore, the effect of excitation frequency on the variation of one of the eddy current indices, real voltage, with respect to relative permeability at different lift-offs is examined. Because a number of graphs were required to characterize the variation, a new concise method of representing the effect of relative permeability and lift-off in a single graph, termed as Phase Diagram, for a particular excitation frequency is proposed in section 3.4.5. In doing so, the trend of change of eddy current indices due to the change in relative permeability and lift-off, at an excitation frequency, can be observed simultaneously from a single, Phase Diagram. Therefore, the phase diagram is further used to demonstrate the effect of probe size and excitation frequency on the eddy current indices using the reflection probes 2D1CH and 10D10CH of 2 mm and 10 mm diameter, respectively, which ultimately provides criteria for selection of suitable probe size and excitation frequency for the eddy current based stress measurement.

3.4.1 Effect of lift-off

Figure 3.4 depicts the relationship between the eddy current indices – real, imaginary, and absolute voltages, and phase detected by the reflection probe 2D1CH, with respect to increasing lift-offs,

at an excitation frequency of 1 kHz. It can be seen that the detected voltages decrease with the increasing lift-off, while the phase increases with increase in lift-off. The trend that detected voltage decreases with the increase in lift-off as the electromagnetic coupling between the probe and the specimen decreases is a well-known behavior of eddy current, thus implying that the numerical model has been correctly formulated.

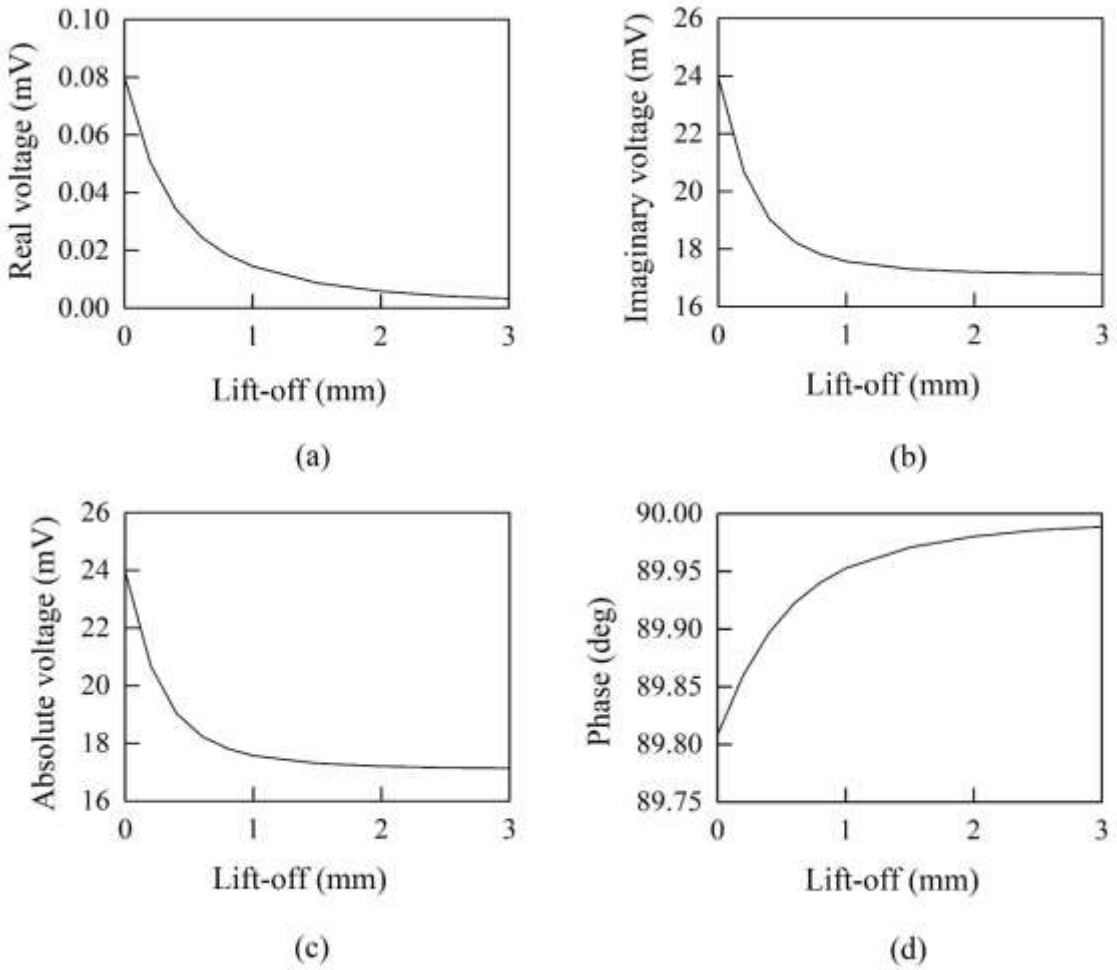

Figure 3.4 Variation of eddy current indices – (a) Real voltage, (b) Imaginary voltage, (c) Absolute voltage, and (d) Phase with respect to lift-off at an excitation frequency of 1 kHz for the reflection probe 2D1CH.

3.4.2 Effect of change in relative permeability along X-direction

The effect of varying the relative permeability of the steel plate along X-direction (μ_{rX}) from 100 to 200, at an excitation frequency of 1 kHz and lift-off of 0 mm, is investigated for the reflection probe 2D1CH. Figure 3.5 shows the change in shape of eddy current distribution due to the change of relative permeability along X-direction. When relative permeability in both X- and Y-directions of the steel plate are equal, i.e. μ_{rX} and μ_{rY} =100 (Figure 3.5 (a)), the shape of eddy current is a perfect circle. As the relative permeability along X-direction (μ_{rX}) is increased to 150 and 200, the shape of eddy current becomes more and more elliptical (Figures 3.5 (b) and (c), respectively). Therefore, eddy current response is affected due to the change in relative permeability and the eddy current indices can be used to determine the change in relative permeability.

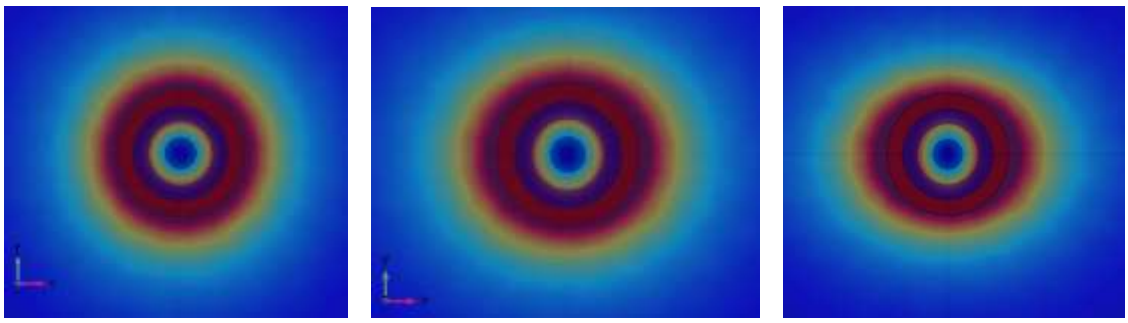

(a) (b) (c)

Figure 3.5 Shape of eddy current distribution for the reflection probe 2D1CH at an excitation frequency of 1 kHz and 0 mm lift-off: (a) when relative permeability in both X- and Y- directions are equal (μ_{rX} =μ_{rY} =100) and when relative permeability along X- and Y- directions are: (b) μ_{rX} =150, μ_{rY} =100, and (c) μ_{rX} =200, μ_{rY} =100.

Figure 3.6 shows the change in eddy current indices – real, imaginary, and absolute voltages and phase detected by the reflection probe 2D1CH, due to change in relative permeability of the steel plate along X-direction (μ_{rX}), at an excitation frequency of 1 kHz and lift-off of 0 mm. The real voltage decreases non-linearly, whereas the imaginary voltage, absolute voltage, and phase increase non-linearly with the increase in relative permeability.

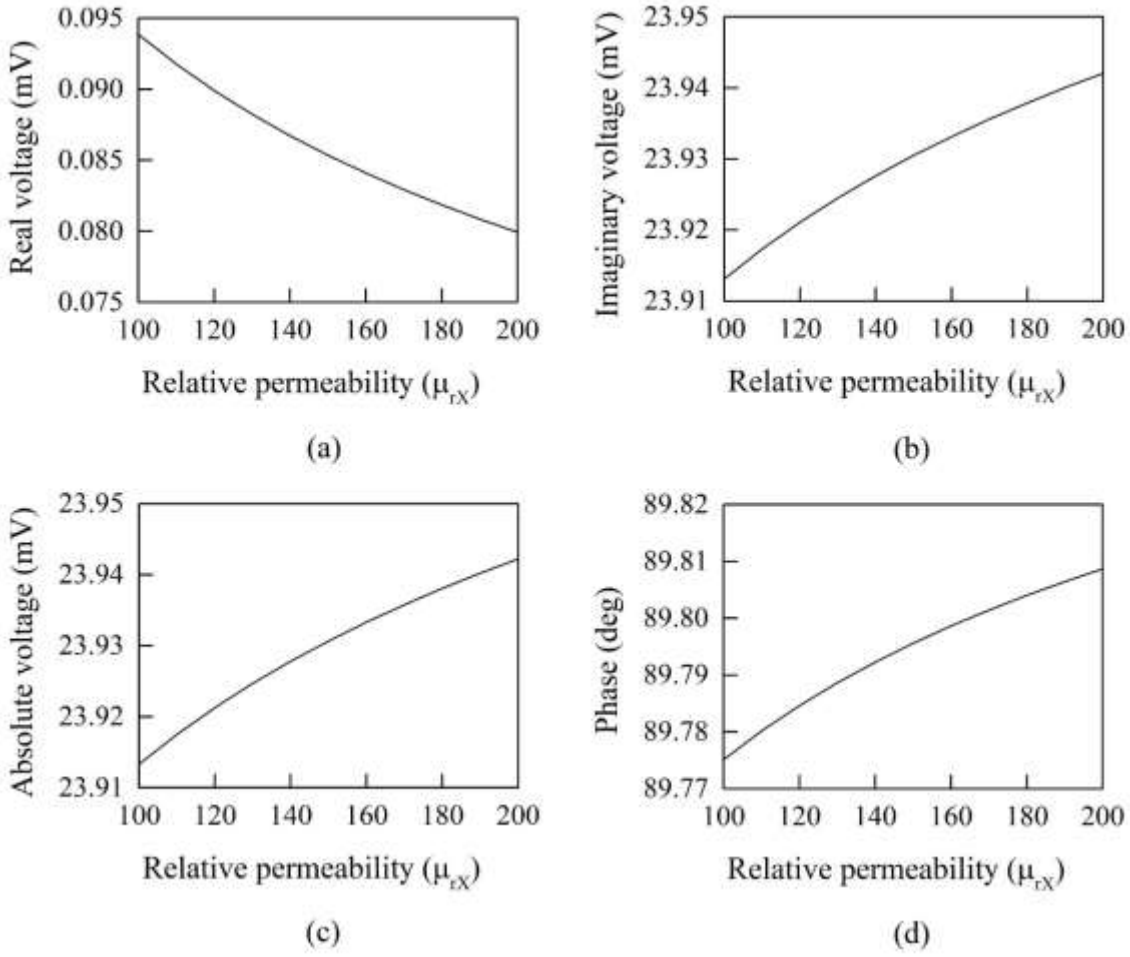

Figure 3.6 Variation of eddy current indices – (a) Real voltage, (b) Imaginary voltage, (c) Absolute voltage, and (d) Phase with respect to relative permeability along X-direction (μ_{rX}) at an excitation frequency of 1 kHz and lift-off of 0 mm for the reflection probe 2D1CH.

3.4.3 Effect of lift-off for a given relative permeability change

It can be noted from Figure 3.4 that the sensitivity of eddy current indices decreases significantly at large lift-offs, particularly at values greater than 1 mm, for a given change in relative permeability along X-direction (μ_{rX} =200μ_{rY} =100). This is because the characteristic elliptical shape of eddy current distribution due to change in relative permeability in X-direction becomes somewhat circular for lift-offs larger than 1mm, as shown in Figure 3.7, therefore diminishing the sensitivity. Hence, it is preferable to limit the lift-offs to a minimal value for stress measurement using eddy current for sufficient sensitivity.

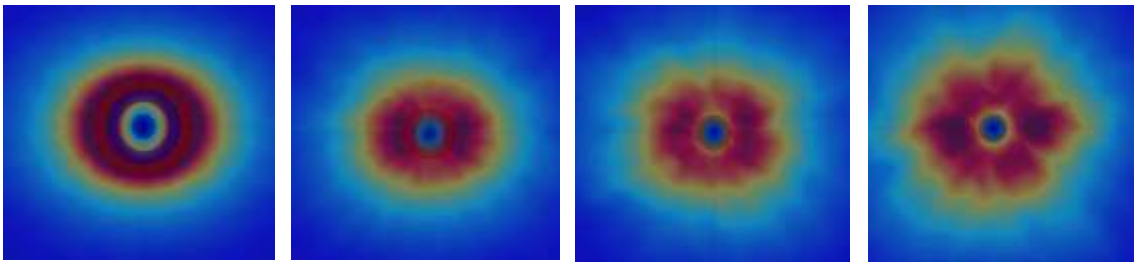

(a) (b) (c) (d)

Figure 3.7 Variation in the shape of eddy current induced in the steel plate at lift-offs of (a) 0 mm, (b) 1 mm, (c) 2 mm, and (d) 3 mm at an excitation frequency of 1 kHz and relative permeability along X- and Y-directions of 200 and 100, respectively for the reflection probe 2D1CH.

3.4.4 Effect of excitation frequency

Figure 3.8 shows the trend of change in real voltage as the relative permeability varies in X-direction (μ_{rX}) at excitation frequencies of 1, 5, and 10 kHz, for lift-offs of 0.6 mm, 2 mm, 2.5 mm, and 3 mm for the reflection probe 2D1CH. The trend is observed to be similar for all the lift-offs

at relatively lower excitation frequencies of 1 and 5 kHz. Whereas, at the higher frequency of 10 kHz, the trend changes drastically at larger lift-offs, and therefore is not desirable for the calibration of eddy current indices with respect to the change in relative permeability of a steel plate due to applied stress. Hence, lower frequencies of 1 kHz and 5 kHz are suitable for the eddy current based stress measurement using 2D1CH probe.

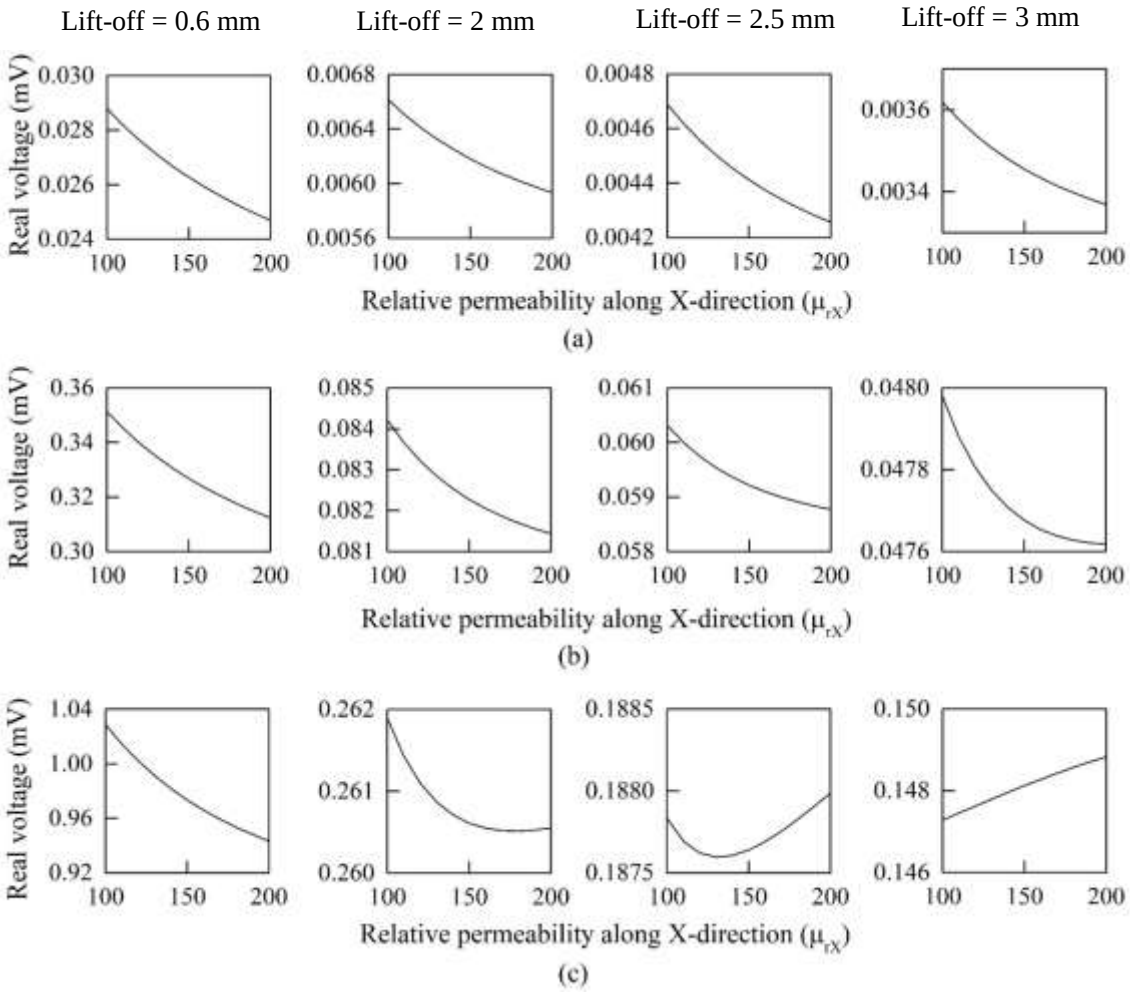

Figure 3.8 Variation of Real voltage with respect to relative permeability along X-direction (μ_{rX}) at excitation frequencies of (a) f = 1 kHz, (b) f = 5 kHz, and (c) f = 10 kHz at lift-offs of 0.6 mm, 2 mm, 2.5 mm, and 3 mm for the reflection probe 2D1CH.

3.4.5 Phase diagram

As seen from figure 3.8, a number of plots are required to ascertain a uniform trend of change in an eddy current index due to the variation of relative permeability at different lift-offs to facilitate the selection of a suitable excitation frequency. Therefore, a new concise way of representing the effect of relative permeability and lift-off in a single graph simultaneously, termed as Phase diagram, is proposed in the present study, where the real and imaginary voltages detected by the reflection probe are plotted along X- and Y-axes, respectively.

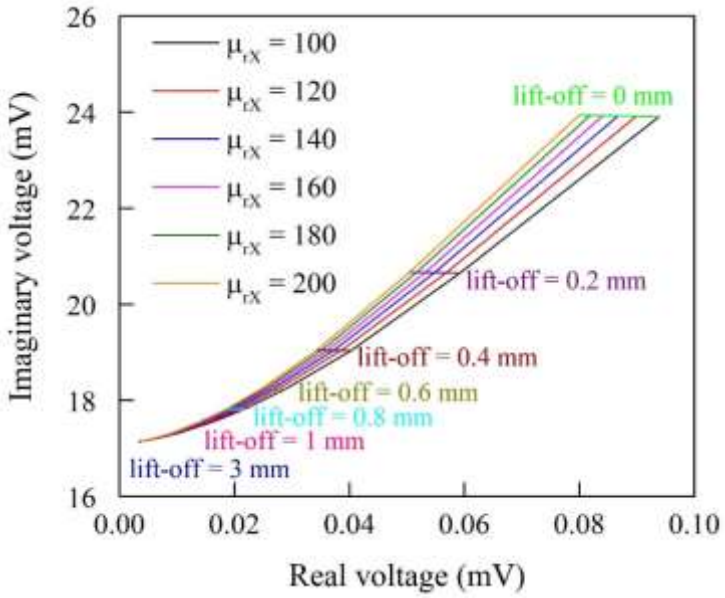

Figure 3.9 Phase diagram for reflection probe 2D1CH showing the trend of change of relative permeability along X-direction (μ_{rX}) and lift-offs at an excitation frequency of 1 kHz.

Figure 3.9 depicts the phase diagram for the reflection probe 2D1CH at an excitation frequency of 1 kHz for different relative permeability along X-direction and lift-offs, whereby the changes due to relative permeability and lift-off can be easily distinguished from their distinct phase differences. It can also be observed that the sensitivity of probe 2D1CH to change in relative permeability diminishes drastically as the lift-off increases, and is negligible for lift-offs greater

than 1mm, implying that lift-offs should be maintained at a minimal value for sufficient sensitivity in detecting the change in relative permeability. Hence, the same information can be represented in a concise and convenient way using a phase diagram. It is to be noted that the phase diagram in Figure 3.9 is for a single probe at an excitation frequency; therefore, the evaluation of effect of probe size, the selection of excitation frequency, and their interrelated effect is further investigated in the following sub-sections using phase diagram.

3.4.5.1 Effect of probe size

The two reflection probes 2D1CH and 10D10CH of 2 mm and 10 mm diameter, respectively, are used to demonstrate the effect of probe size on the eddy current indices using phase diagrams as shown in Figures 3.10 and 3.11. It can be seen that the sensitivity of smaller probe 2D1CH became negligible for lift-offs greater than 1 mm while the larger probe 10D10CH is sensitive to the change in relative permeability even at the larger lift-off of 3 mm. Furthermore, the trend of change of relative permeability is consistent at different lift-offs for all the excitation frequencies of 1, 5, and 10 kHz for the smaller probe 2D1CH, indicating that any of the above frequencies is suitable for the measurement, despite Figure 3.8 showing the non-uniform trend for lift-offs greater than 2 mm. This is because the sensitivity of smaller probe 2D1CH becomes negligible for lift-offs greater than 1 mm and the inconsistent trend observed at higher lift-offs of 2 or 3 mm could not be observed in the phase diagram. On the other hand, the trend of change for the larger probe 10D10CH was found to be inconsistent at frequencies of 1, and 5 kHz, while uniform change in relative permeability at different lift-offs was observed at a frequency of 100 Hz, which is lower than that for the 2D1CH probe. Hence, the probe size has a significant effect not only on the lift-off sensitivity but also on the selection of excitation frequency for the eddy current based stress measurement.

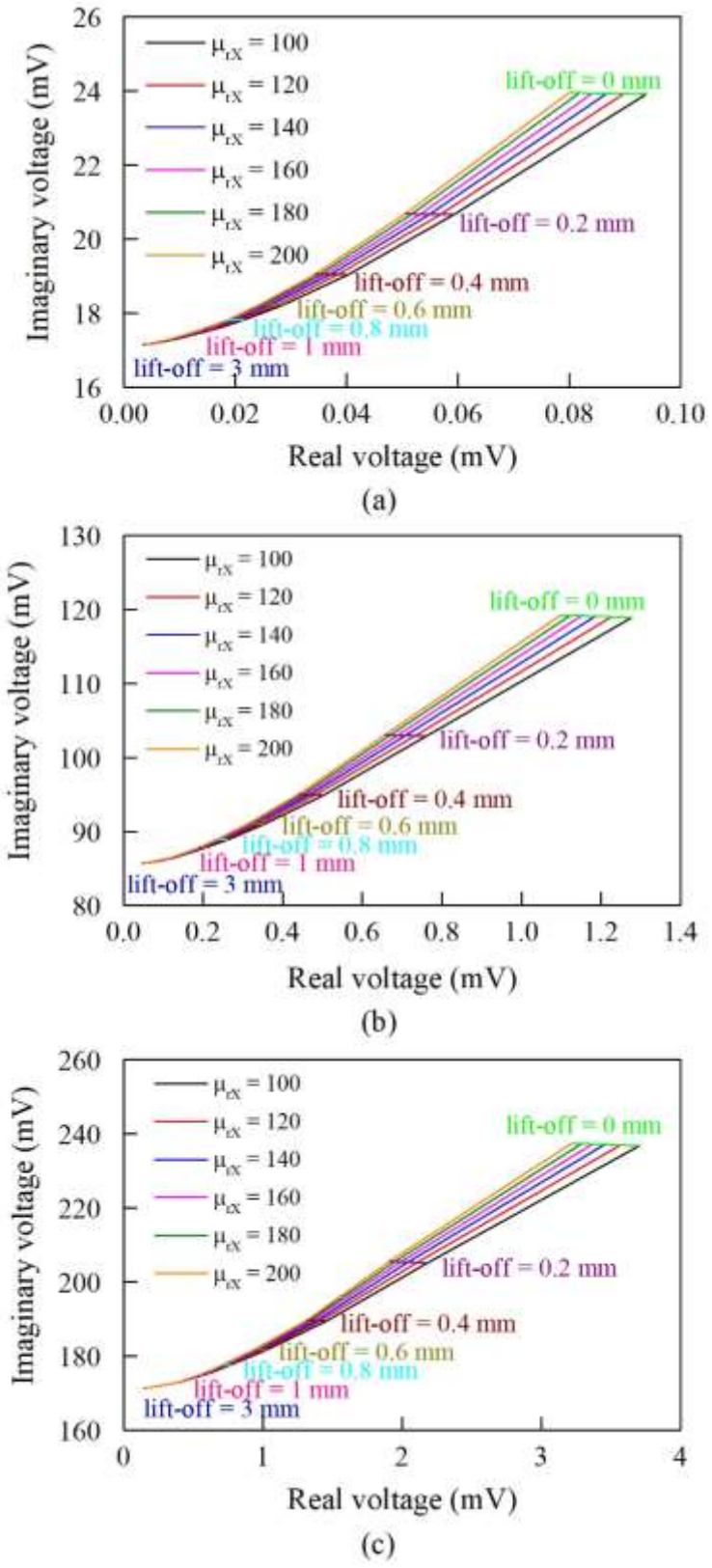

Figure 3.10 Phase diagram for the smaller probe 2D1CH at different excitation frequencies of (a) 1 kHz, (b) 5 kHz, and (c) 10 kHz.

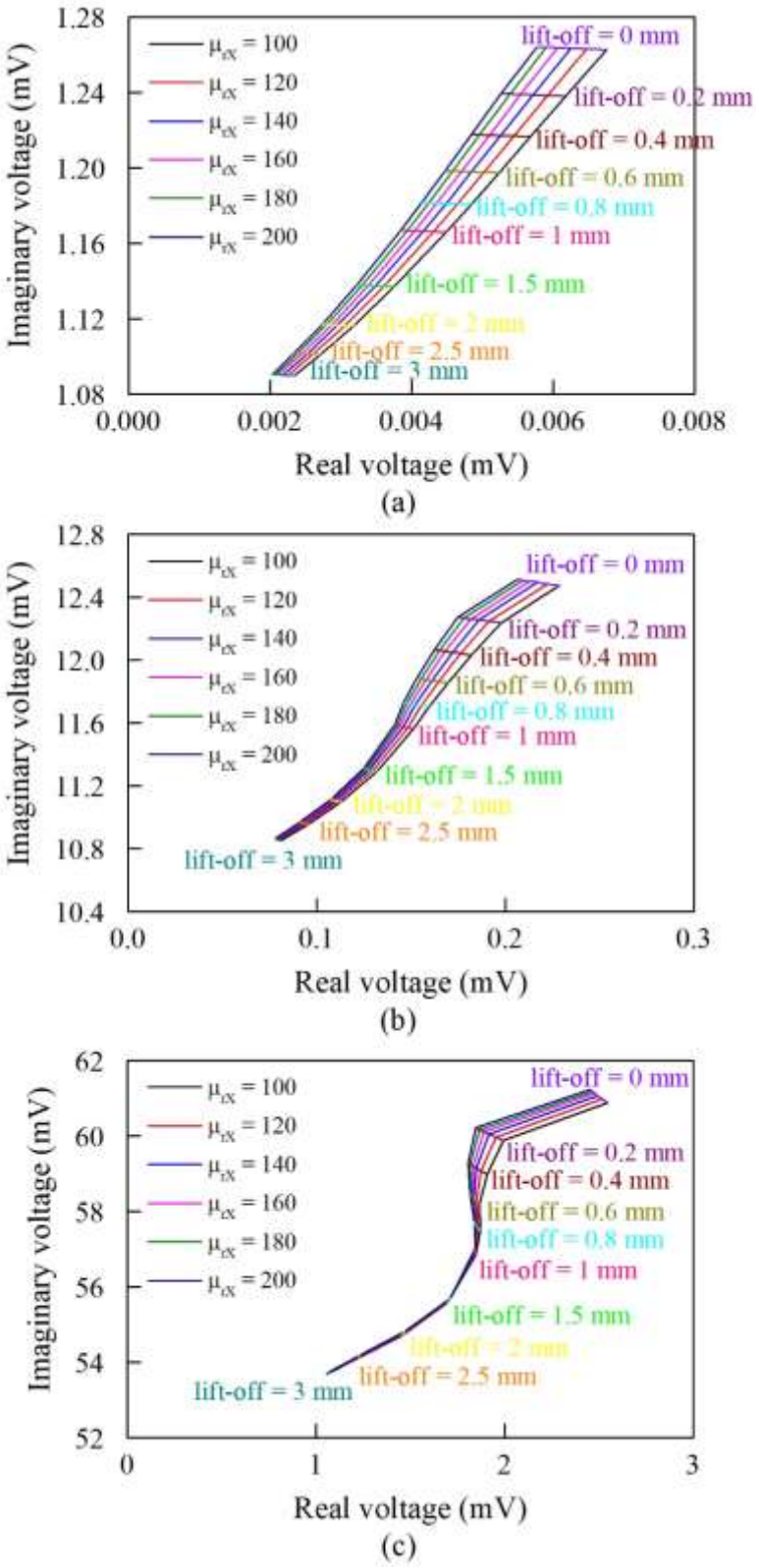

Figure 3.11 Phase diagram for the larger probe 10D10CH at different excitation frequencies of (a) 100 Hz, (b) 1 kHz, and (c) 5 kHz.

3.4.5.2 Selection of probe size and excitation frequency

Based on the numerical results obtained for the reflection probes 2D1CH and 10D10CH, it can be concluded that larger probe provides better sensitivity to lift-offs and, therefore, is desirable for the inspection of a corroded steel plate girder having significant lift-offs, unlike the smaller probe where the lift-off has to be limited to a minimal value for sufficient sensitivity. Moreover, the probe size also governs the selection of excitation frequency for stress measurement as concluded in the previous section. The criteria for selection of excitation frequency is the consistent trend of change of relative permeability at different lift-offs so that it can be used for the calibration of stress using eddy current indices. According to the phase diagrams of probe 10D10CH at different excitation frequencies, the lower excitation frequency of 100 Hz shows the consistent trend of change and, therefore, should be selected for stress measurement. Hence, larger probe size and lower excitation frequencies are preferable in the eddy current based stress measurement owing to the sufficient sensitivity to the lift-offs and consistent trend of change in relative permeability at different lift-offs required for the calibration, respectively.

3.4.6 Effect of change in relative permeability along all three directions

Therefore, after the selection of probe 10D10CH at an excitation frequency of 100Hz, the robustness of the eddy current based stress measurement is investigated for the behavior of eddy current index, absolute voltage, for change in relative permeability along all three directions – X, Y, and Z, denoted by μrX, μrY, and μrZ, respectively as shown in Figure 3.12. It can be clearly observed that the changes due to relative permeability in different directions have distinct effects on the absolute voltage value detected by the eddy current probe 10D10CH. Hence, eddy current based stress measurement is feasible in determining the effect of multi-directional stress variation.

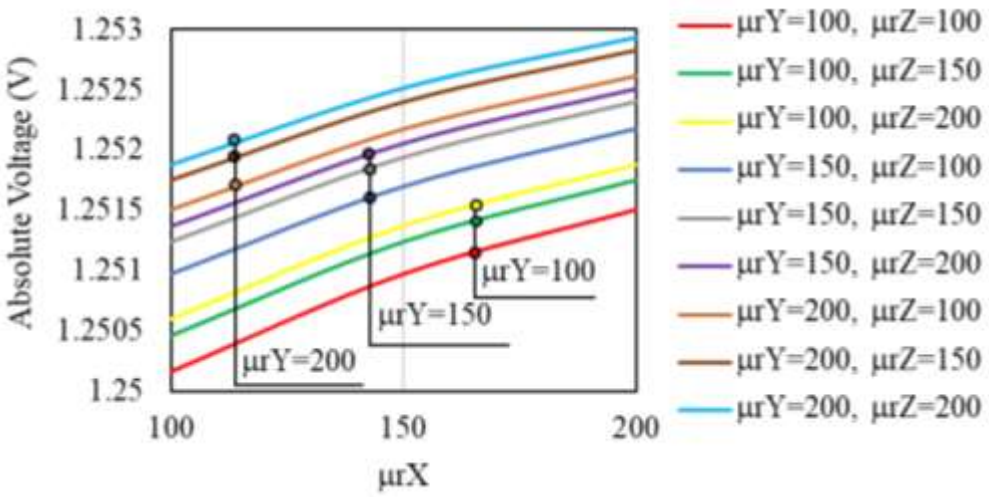

Figure 3.12 Variation of absolute voltage with respect to the relative permeability along X, Y, and Z -directions for 10D10CH probe at an excitation frequency of 100 Hz.

3.5 Summary

In this chapter, three-dimensional numerical simulations were conducted in the AC/DC module of FE software, COMSOL Multiphysics 5.2a for a steel plate, the relative permeability along X-direction of which was varied to denote the change in stress state brought about by inevitable factors such as corrosion and cracking. The eddy current indices – real voltage, imaginary voltage, absolute voltage, and phase obtained from the reflection probe were utilized to characterize the eddy current response due to change in influential parameters namely, relative permeability, lift-off, and excitation frequency. Phase diagram, constructed by plotting the real and imaginary voltages along X- and Y- directions, respectively, is then proposed as a new concise way to represent the trend of change of relative permeability and lift-offs. Furthermore, Phase Diagram played a pivotal role in providing the criteria for the selection of suitable probe size and excitation frequency, i.e. sufficient sensitivity with respect to lift-offs, and uniform trend of change for calibration during the stress measurement, respectively. Hence, the findings of the present study

are as follows:

(1) The effect of change in relative permeability, which is dependent on the stress, lift-offs, and excitation frequency can be determined using the eddy current indices – real, imaginary, and absolute voltages, and phase detected by the reflection probe.

(2) Phase diagram condensed a multiple number of graphs into a single graph thus providing a much concise way of representing the effect of variation of relative permeability and lift-off on the eddy current indices simultaneously, at a particular excitation frequency, which can be distinguished based on their phase differences. It is then used for the evaluation of effect of probe size and selection of excitation frequency.

(3) The probe size not only governs the sensitivity to lift-offs, but also the selection of excitation frequency for the stress measurement. The larger probes are desirable for the field inspections of a corroded steel plate girder with significant lift-offs due to their greater sensitivity to the change in relative permeability even at significant lift-offs of 3 mm, as deduced from the comparison of phase diagrams for reflection probes 10D10CH and 2D1CH having 10 mm and 2 mm diameter, respectively.

(4) In addition, uniform trend of change of relative permeability at different lift-offs was observed for the smaller probe 2D1CH at different excitation frequencies, indicating a wider range of suitable frequencies for the stress measurement. On the other hand, the trend of change was found to be inconsistent at higher frequencies for the larger probe 10D10CH. Hence, the probe size also affects in the further selection of excitation frequency.

(5) The excitation frequency is selected based on the consistent trend of change of relative permeability at different lift-offs for facilitating the calibration during stress measurement

using eddy current. It is found that higher excitation frequencies give inconsistent trend of change, while the smaller frequency showed uniform trend of change, as seen in the phase diagram for 10D10CH probe. Hence, lower frequencies are preferable in eddy current based stress measurement owing to the need of consistent trend of change for calibration.

Hence, the viability of the eddy current testing to stress measurement has been investigated through numerical simulations factoring in the influential eddy current parameters such as lift-off, excitation frequency, and probe size. Whereby, phase diagram was devised as a new method that proffers a concise way to determine the change due to relative permeability and lift-off, and for the selection of suitable probe size and excitation frequency for the eddy current based stress measurement.

Chapter 4. Experimental Investigation on Application of Eddy Current Based Stress Measurement

This chapter explores the feasibility of application of eddy current based stress measurement in two different scenarios – detection of fatigue crack in a butt-welded tensile specimen and measurement of bolt tension and its variation. The eddy current index is first characterized to the known values of applied tensile stress and the stress values are back calculated from this calibration data to obtain the stress values near the weld toe, which provides the stress behavior change due to crack formation and propagation. On the other hand, the eddy current index obtained at the bolt head are used to characterize different bolt tensions, confirming that eddy current based stress measurement can be applied in measuring the remaining bolt tension.

4.1 Overview

In the previous chapter 3, eddy current based stress measurement was investigated through numerical simulations on a steel plate subjected to change in relative permeability, to characterize the change in eddy current indices to the applied stress. In this chapter, the application of this concept is tested out for the following 2 cases:

Case 1. Detection of the fatigue crack in a butt-welded tensile specimen subjected to fatigue, based on the change in stress near the weld toe due to the formation of crack, and

Case 2. Characterization of eddy current index to the variation of bolt tension in a high-strength bolt.

For Case 1, a tensile test is first conducted with the available eddy current probe 700P11A, where the calibration of the eddy current indices is carried out corresponding to the applied stress on a tensile specimen. Parametric study is conducted for different excitation frequencies and lift-offs to construct the Phase diagram using the detected real and imaginary voltage values. Using the concept derived from Chapter 3, a suitable excitation frequency is selected to construct the calibration data of voltage versus stress to determine the stress values near the weld for the following fatigue test based on the detected voltage values. Sensitivity analysis regarding the input voltage supply to the eddy current probe was also conducted to ensure discernible changes in the eddy current indices to the change in applied stress. Then, from the calibration data thus obtained, the stress near the weld toe is determined for the butt-welded tensile specimen subjected to fatigue loading. The eddy current based stress measurements are carried out after each loading cycle so that the variation in stress observed near the weld toe can be evaluated to understand how the stress varies as the crack forms and propagates into the specimen, thus proffering the possibility of crack

detection. This change in the stress behavior due to crack formation and propagation are also investigated through numerical simulations.

For Case 2, Skidmore-Wilhelm bolt tension calibrator (MZ-100) was used to determine the tensile load induced into a high-strength bolt of M22 grade using a torque, while eddy current probe 700P11A was concurrently used to characterize the eddy current response to the bolt tension. While doing so, the applicability of the eddy current based stress measurement in correlation to the varying bolt tension is affirmed. The numerical simulations are carried out beforehand to ascertain the variation of stress in the bolt head at different bolt tensions, providing a basis that bolt tension can be correlated with the eddy current response at the top of bolt head. Furthermore, the mutual effects of the corrosion, simulated by reduced bolt-head thickness and the bolt tension is also investigated using the eddy current based stress measurement.

4.2 Detection of fatigue crack in a butt-welded tensile specimen using eddy current based stress measurement

As explained in section 1.3.3, there is accessibility problem in detection of the fatigue cracks in the welded structures since they generally originate near the weld toe and beneath the rust layer of weathering steel. To counter this, eddy current based stress measurement is used to determine the stress change behavior near the weld toe due to the formation of crack and propagation, which can then be used as a benchmark for future detection of cracks. To this end, the tensile test is first carried out to characterize the eddy current index – absolute voltage against the applied tensile stress, which is then used to determine the stress near the weld toe based on the absolute voltage values detected by the probe at different weld locations.

4.2.1 Tensile test

4.2.1.1 Experimental procedure

The experimental setup for the tensile test is shown in Figure. 4.1 (a), where the tensile specimen is clamped between the fixed lower jack and the movable upper jack of the Hydraulic Servo Fatigue Testing Machine (Model LST-30) by Sagniomiya, with a maximum dynamic loading capacity of 300 kN. A strain gauge is pasted on the middle of one side of the tensile specimen to measure the stress applied, while an eddy current probe, 700P11A (Figure 4.1 (b)), is placed on the converse side of the specimen to obtain the eddy current response to the applied tensile load.

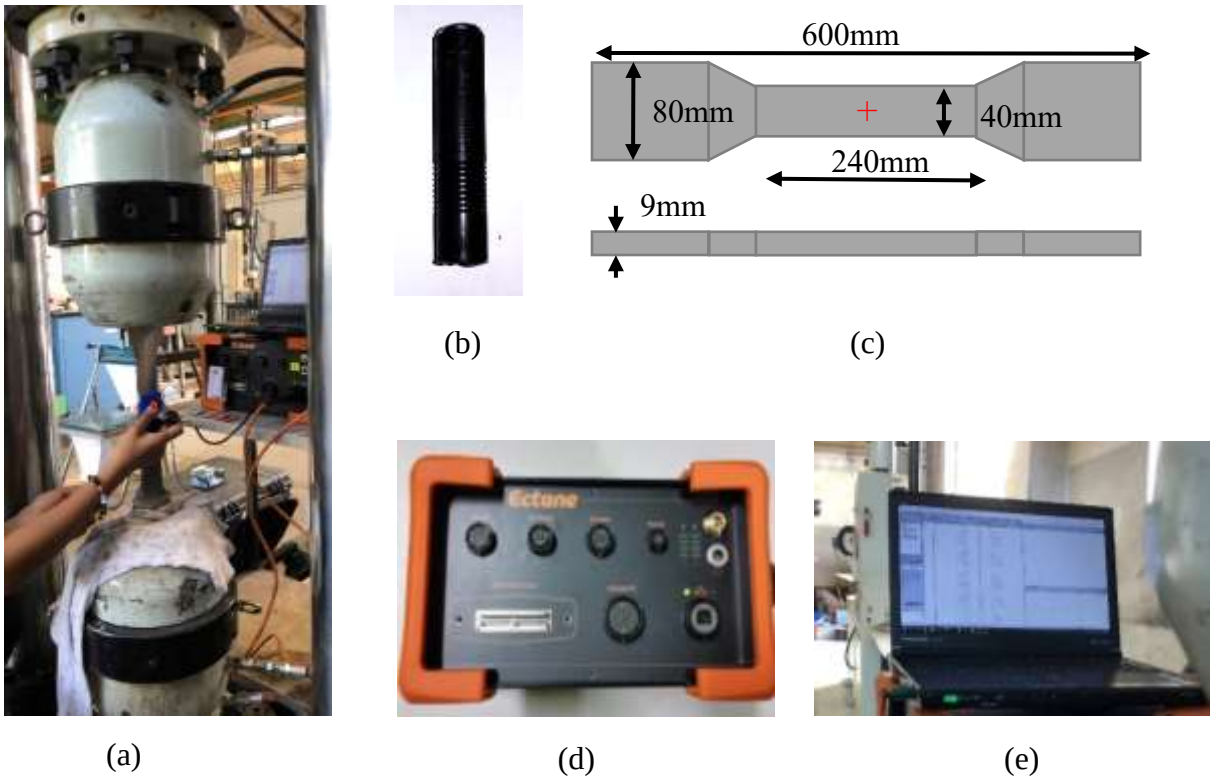

Figure 4.1 (a) Experimental setup for tensile test conducted in a Hydraulic Servo Fatigue Testing Machine (Model LST-30), (b) Eddy current probe 700P11A, (c) Dimension of the tensile specimen, (d) Ectane, and (e) Magnifi.

The commercially available probe sizes for surface probes from GE Inspections are 7 mm, 11 mm, and 24 mm. But since we need to detect stress changes along the weld line due to the formation of cracks, smaller probe size are preferable. However, it has been found from the FE analysis that the larger probe size shows better sensitivity to change in stress. Keeping in view these two contrasting criteria, the 11 mm diameter probe 700P11A has been selected in the present study.

The dimension of the tensile specimen is shown in Figure 4.1 (c); the red cross shows the location of the strain gauge or the eddy current probe measurement point. The load is applied statically as 0, 18, 36, 54, and 72 kN equivalent to a tensile stress of 0, 50, 100, 150, and 200 MPa, respectively. The eddy current probe, 700P11A, is a reflection probe of 11 mm diameter with the frequency range of 300 Hz to 100 kHz, manufactured by GE Inspection & Technologies [84]. It is connected to the Ectane (Figure 4.1 (d)), the signal generator that supplies the input voltage to the probe and is linked to the Magnifi software on a laptop (Figure 4.1 (e)), providing the GUI and post processing abilities of the data obtained from the eddy current probe.

Based on the concept of chapter 3, the variation of eddy current indices – real, imaginary, and absolute voltages with respect to the change in excitation frequency for various lift-offs was investigated for the probe 700P11A. The four, excitation frequencies of 1, 5, 10, and 15kHz were used for the probe and lift-offs of 0, 0.025, 0.051, 0.102, 0.254, 0.508, and 0.762 mm were simulated by using thin strips of known thickness. A new setup file was created that can take into account all four frequencies at once, instead of using previous setup file that can handle only a single frequency; thus the measurement was made more time efficient. It is to be noted that the probe 700P11A was first balanced to zero at the center of the tensile specimen and the detected

voltages were obtained for the subsequent changes in the tensile stress. However, the input voltage supplied in the experiment set to 1V was found to be insensitive to the change in applied stress to the tensile specimen. Hence, input voltage or current was obtained as an additional factor to be taken into account for the application of the eddy current based stress measurement. Consequently, a sensitivity study was conducted additionally to confirm sufficient variation of the eddy current indices to change in applied stress, whereby an input voltage of 5V was found to give discernible changes in the eddy current indices and therefore was used to conduct the eddy current based stress measurement for the tensile test.

4.2.1.2 Results and discussion

The phase diagram is constructed for the probe 700P11A for stress variation from 0 to 200 MPa and lift-off from 0 to 0.762 mm at an excitation frequency of 1kHz, as shown in Figure 4.2. As was observed in Chapter 3, the phase diagram thus obtained from the experimental results also offered a concise representation of change in the eddy current indices due to both stress and lift-off, while the effect of lift-off could be distinguished from that of stress based on their distinct phase differences.

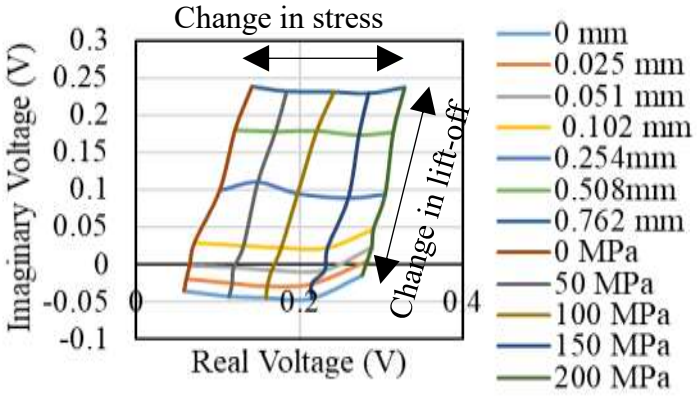

Figure 4.2 Phase diagram for eddy current probe 700P11A at an excitation frequency of 1 kHz

Next, phase diagrams were plotted for all four excitation frequencies of 1, 5, 10, and 15kHz to evaluate the sensitivity of different excitation frequencies to the change in detected voltages due to stress and lift-off (Figure 4.3). It can be seen that the lower excitation frequencies of 1 and 5 kHz have higher sensitivity to change in stress than the larger excitation frequencies of 10 and 15 kHz. Furthermore, a non-uniform trend of change due to stress was observed at higher frequencies of 10 and 15 kHz, along with the overlapping lines implying non-unique values of stress corresponding to a detected voltage value, which is highly undesirable for calibration purpose.

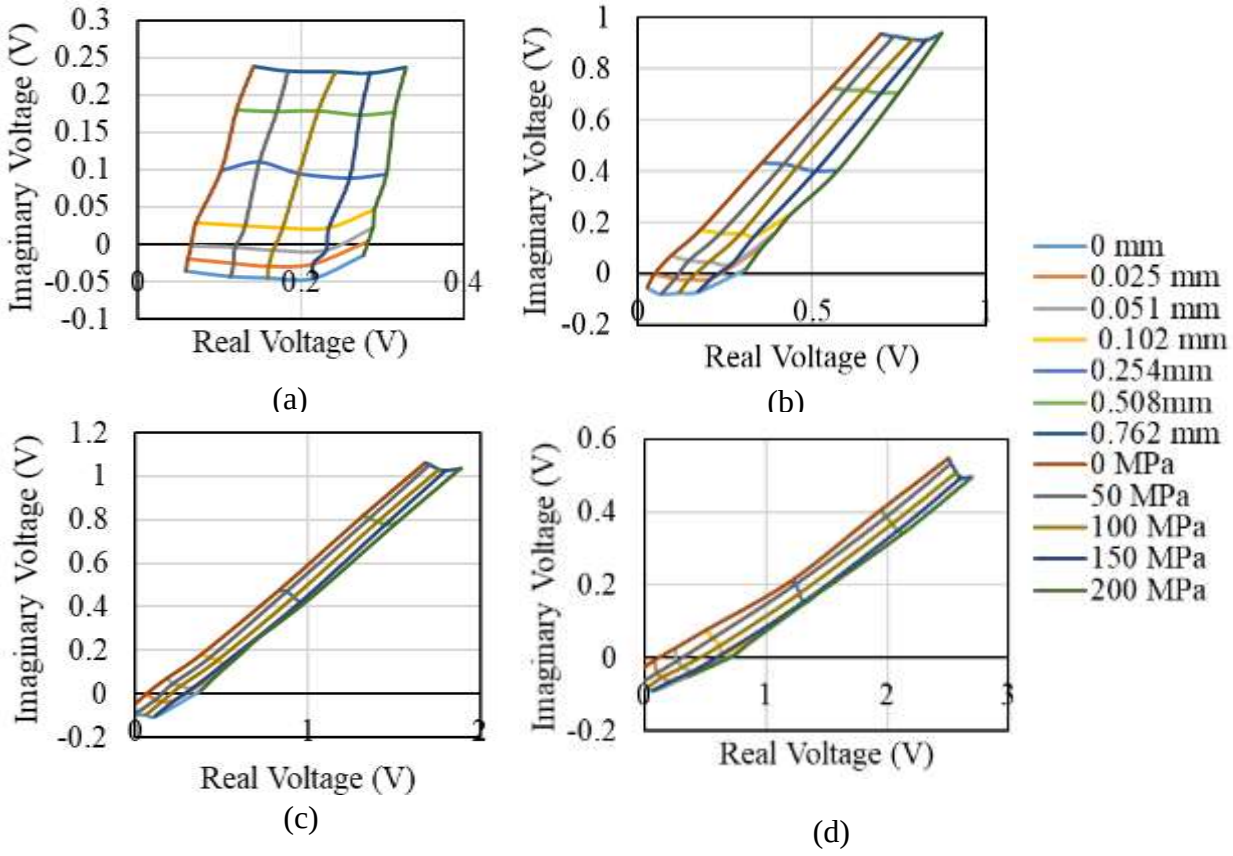

Figure 4.3 Phase diagram for eddy current probe 700P11A at excitation frequencies of (a) 1 kHz, (b) 5 kHz, (c) 10 kHz, and (d) 15 kHz, respectively.

Since the excitation frequency of 5 kHz shows larger variation in the values of detected voltages, it is selected to conduct further eddy current based stress measurement in the fatigue test, in addition to its sufficient sensitivity and uniform trend of change due to stress. In addition, the excitation frequency of 5kHz with a sampling rate of 5,000 samples per second also capitalizes on the minimal data acquisition time.

The calibration data is now constructed by plotting the change in eddy current indices – real, imaginary, and absolute voltages for the eddy current probe 700P11A at an excitation frequency of 5kHz, input voltage 5V, and 0 mm lift-off for variation of tensile stress from 0 to 200 MPa as shown in Figure 4.4. The real and absolute voltages show good sensitivity to the change in applied stress, while the imaginary voltage seems to be more or less insensitive to the change in applied stress. Therefore, absolute voltage has been selected in the present study as a suitable eddy current index to calibrate the applied stress to, for the eddy current based stress measurement.

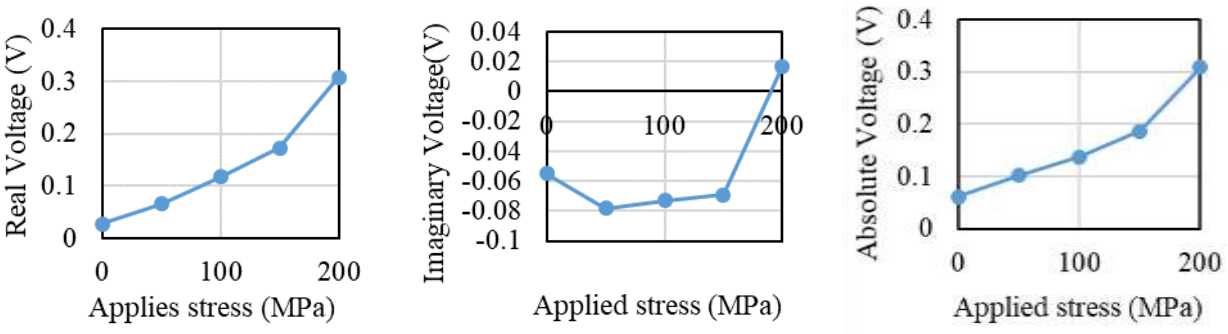

(a) (b) (c)

Figure 4.4 Variation of eddy current indices (a) Real Voltage, (b) Imaginary Voltage, and (c) Absolute voltage with respect to the applied stress for 700P11A, eddy current probe, at an excitation frequency of 5kHz, at 0 mm lift-off.

To this end, an exponential curve is fitted to describe the relationship between the absolute voltage and applied stress, as shown in Figure 4.5, for the eddy current probe 700P11A at an excitation frequency of 5kHz, input voltage 5V, and 0 mm lift-off. This exponential relationship is utilized in the fatigue test to back calculate the value of stress near the weld toe of the butt-welded tensile specimen corresponding to the absolute voltage value obtained from the eddy current probe, 700P11A, at the same operating conditions of 5 kHz excitation frequency, input voltage 5V, and 0 mm lift-off.

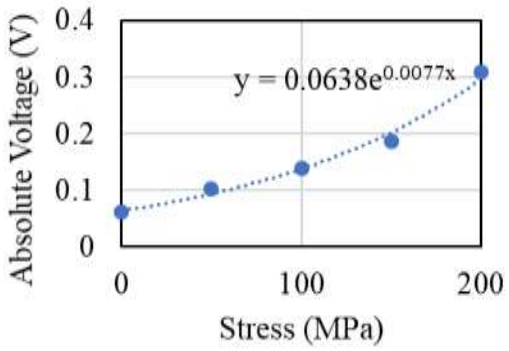

Figure 4.5 Calibration data with the best-fit exponential curve for 700P11A, eddy current probe, at an excitation frequency of 5 kHz, input voltage 5V, and 0 mm lift-off.

4.2.2 Fatigue test

4.2.2.1 Experimental procedure

Next, the fatigue test is conducted for the butt-welded tensile specimen, the experimental setup for which is shown in Figure 4.6. The specimen is fit between the lower fixed jack and the upper moving jack of the Hydraulic Servo Fatigue Testing Machine (Model LST-30), a strain gauge is attached to one side of the butt-welded tensile specimen to get the nominal stress, and the eddy current probe, 700P11A, is used to obtain the detected voltage values for the stress occurring near the weld.

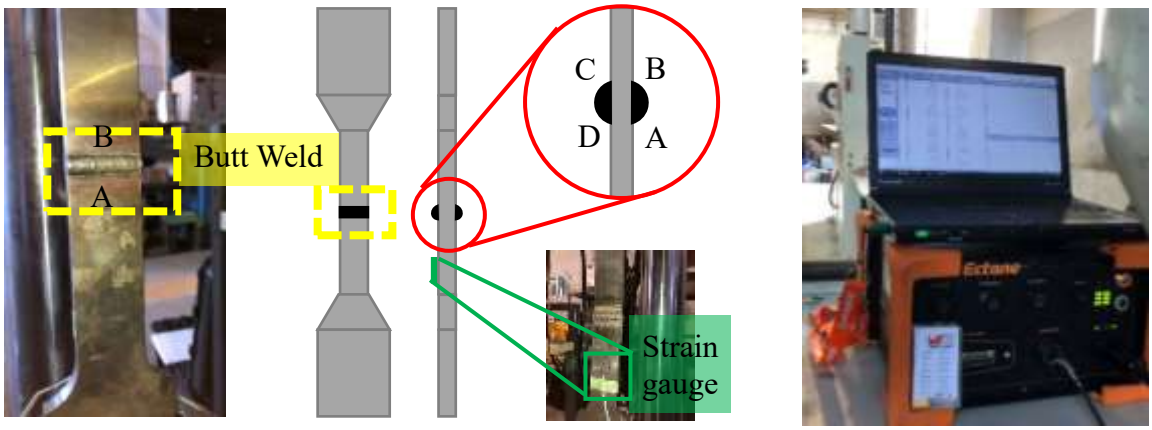

(a) (b) (c)

Figure 4.6 (a) Butt-welded tensile specimen, (b) Front and side views of the tensile specimen showing the four locations of eddy current measurement – A, B, C, and D, and the location of strain gauge, and (c) Ectane and laptop for Magnifi

The Ectane serves as the signal generator and receiver to the eddy current probe, while Magnifi software provides the GUI, links to the Ectane and the eddy current probe, and collect and store data for further processing. Since the exact location of formation of crack in a butt weld cannot be predicted, the eddy current based stress measurements are carried out at four, equally likely locations of crack formation, near the weld toe as shown in Figure 4.6 (b).

The cyclic load is applied in the form of a sine wave, varying from 5 -78 kN with an amplitude of 36.5 kN and a frequency of 5 Hz, to the specimen at an increment of 50,000 cycles, generating a maximum stress of 200MPa in the specimen (Figure 4.7). Beach marks tests are conducted alternately in between the main tests, also for 50,000 cycles, with a cyclic loading in the form of sine wave, varying from 41.5 to 78 kN, with an amplitude of about 18 kN with the

same loading frequency of 5 Hz. It is essential to conduct the beach marks test in order to arrest the crack, thus providing a physical insight as to how the crack propagates into the specimen.

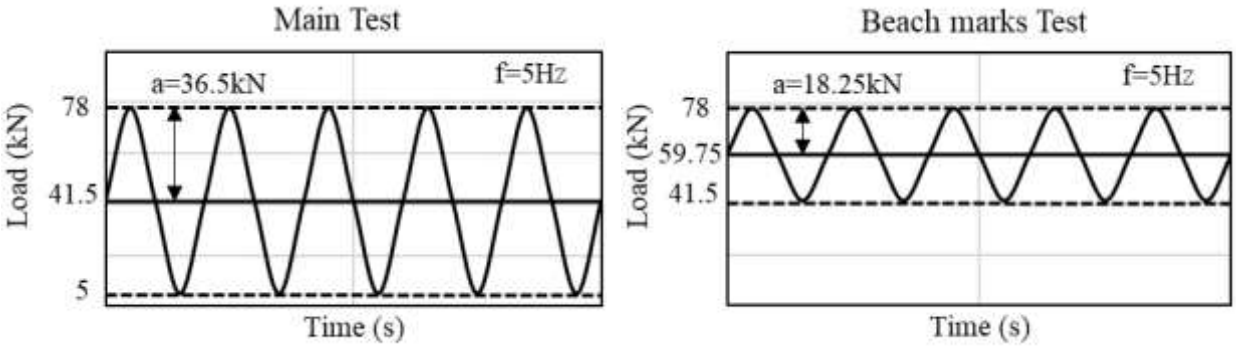

(a) (b)

Figure 4.7 Cyclic loading for (a) Main test and (b) Beach marks test.

The butt weld is of the category D based on Japanese Standard, and its fatigue strength curve is shown in Figure 4.8. For the loading variation from 5 – 78kN, corresponding to a stress variation of 15 – 200 MPa, the change in stress is 185 MPa and the number of loading cycles until fatigue for the stress change of 185 MPa is obtained to be around 500,000 cycles from Figure 4.8 (b). The detail dimension of the tensile specimen with butt weld is shown in Figure 4.9; it has a weld of 3 mm height and 11 mm width. The red, cross shows the location of strain gauge for nominal stress measurement and the dashed yellow circles are two of the four selected measurement locations of eddy current probe, 700P11A for the eddy current based stress measurement described as follows.

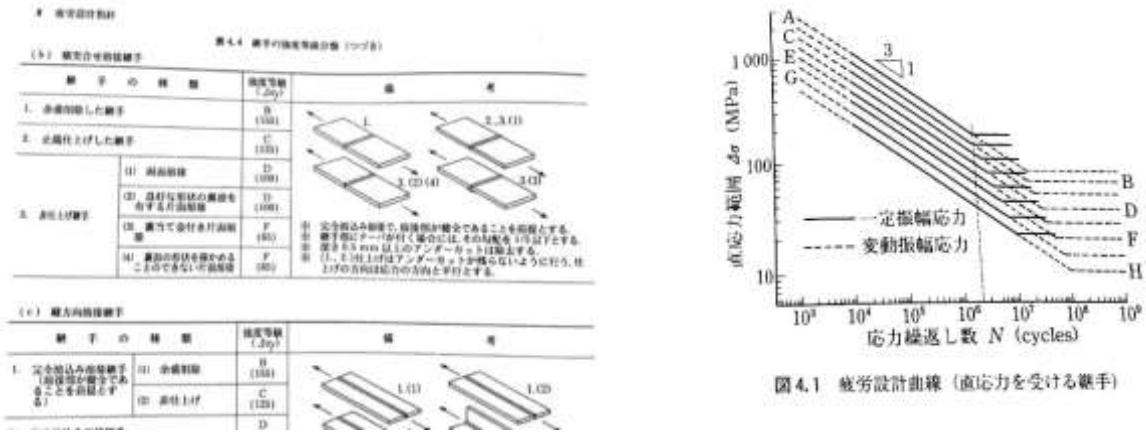

(a) (b)

Figure 4.8 (a) Butt weld category and (b) Fatigue strength curve for category D butt weld.

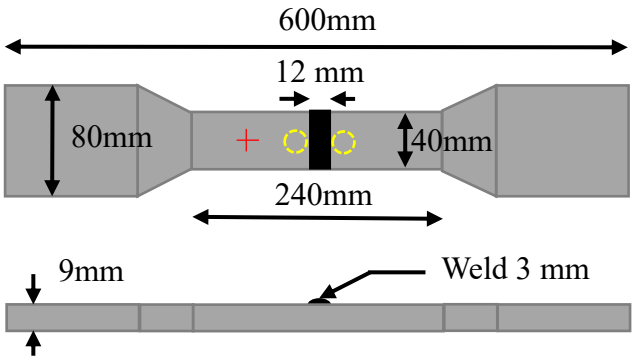

Figure 4.9 Top and side views of the tensile specimen with butt weld

The eddy current based stress measurement is carried out at four locations A, B, C, and D of the specimen near the weld toe as show in Figure 4.9 (b), after every 50,000 cycles, for both the main tests and the beach marks test, up until the specimen cracks due to fatigue. The eddy current probe 700P11A with an excitation frequency of 1kHz and 5V input, maintained at the lift-off at 0 mm is used to conduct the measurement. The probe is first balanced to zero at 0mm lift-off in the weld-free zone of the specimen and then the voltages are obtained at the four locations A, B, C, and D. The detected voltages at these four locations are then converted to their corresponding

stress values based on the calibration curve obtained in section 4.2.1.2 from the tensile test.

4.2.2.2 Results and discussion

The tensile specimen fractured at a total of 1,000,000 cycles of load, including the beach marks test, as seen in Figure 4.10, which is about 550,000 cycles of main test, and is comparable to the no. of cycles until fracture obtained from the fatigue strength curve in Figure 4.8 (b). The beach marks formed due to the crack arrest after 450, 000, 500,000 main cycles and the fracture line before it completed 550, 000 main cycles indicate that the crack originated from the weld toe at location C and propagated through the base metal into the side B until fracture occurred. Another point to be noted is that the crack is not formed at the center of the weld toe, but is oblique. Furthermore, based on the first, discernible crack observed in the fracture surface, two miniature cracks formed separately, which then coalesced to form one larger crack.

The stress behavior changes at the location C at different stages of crack formation and propagation until fracture occurs is then evaluated using the eddy current based stress measurement, as shown in Figure 4.11. The detected voltage values from the eddy current probe were converted to their corresponding stress values based on the calibration curve in Figure 4.5, and normalized to show the change in stress level due to the crack formation and propagation. It is to be noted that the stress obtained in the experimental measurement is the average stress value of the area beneath the probe at the location of measurement and not the stress at the crack tip.

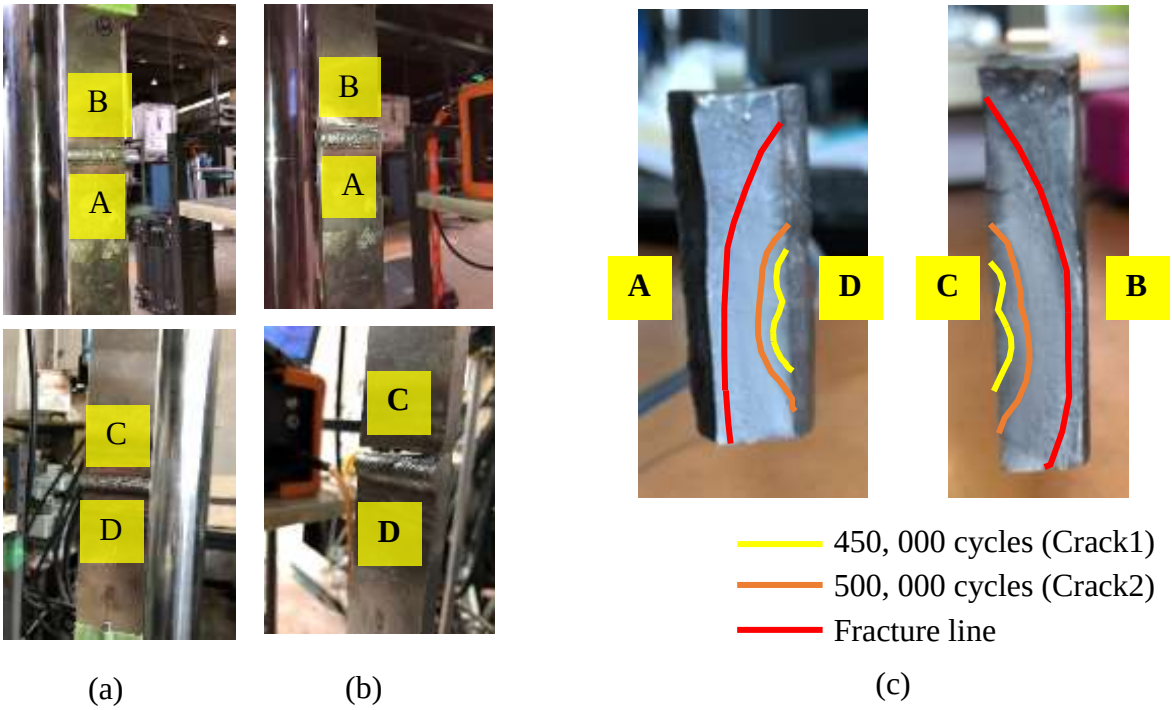

Figure 4.10 Tensile specimen with butt weld (a) before and (b) after cracking, and (c) Beach marks and fracture surface observed in the cracked specimen.

The formation of cracks 1 and 2 can be identified in Figure 4.11 from the beach marks formed after 450,000 and 500,000 main cycles. On the other hand, the stress fluctuation was observed during the formation and propagation of crack. In the experimental work conducted by Itami et al. (2017) [88] for the stress change near the weld of a gusset joint, a continuous decrease in the stress at the location of crack formation and propagation was observed (Figure 4.12 (a)). However, it is to be noted that in case of gusset joint, the location of crack formation is known, i.e. at the center of the weld. The probe can be placed such that it lies central to the crack as shown in the schematic representation in Figure 4.12 (a) and the high stress concentration areas near the crack edge can be avoided. The black circle shows the probe location, the green line indicates the crack, and red circles, the crack edges. A decrease in stress due to the formation of crack and its propagation is seen in Itami's work. This is because the stress near the crack decreases due to its

formation since there is no contact between crack faces and stress is not transferred from one face to the other, whereas the stress concentrates at the crack edges. On the other hand, the crack can initiate at any location along the weld toe for the butt-welded joint as shown in Figure 4.12 (b). When the probe is placed towards the center, along the weld toe, it is likely to encounter the high stress concentration zones at or near the crack edge instead of the decreased stress zone along the crack length.

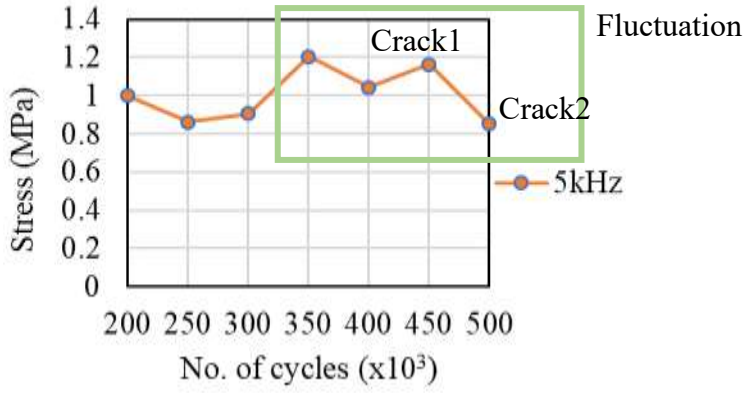

Figure 4.11 Stress level change at different stages of crack formation and propagation during the fatigue test at location C.

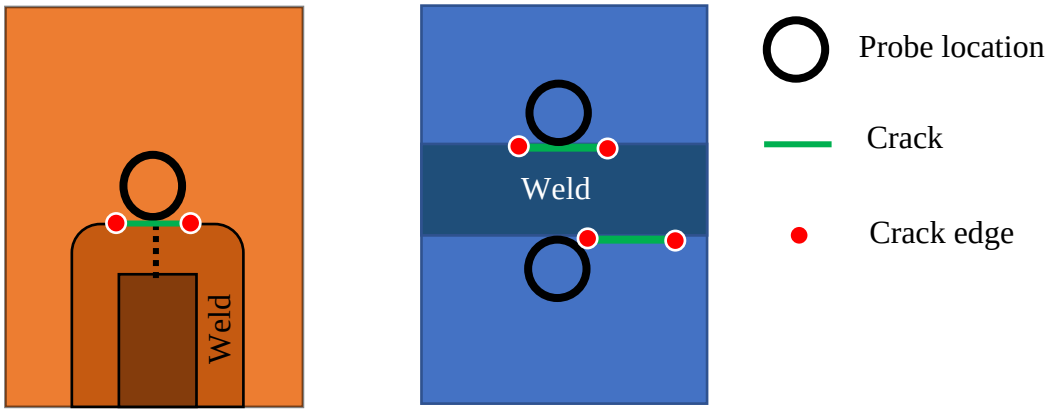

Figure 4.12 Crack formation and location of eddy current probe in (a) Gusset joint, and (b) Butt-welded joint.

In the present experimental study, the probe was generally placed at the center of the specimen at the weld toe while the crack formed was off-center. Consequently, the fluctuation of stress is observed as shown in Figure 4.11 implying that the probe picked up the data from high stress concentration zones near the crack edges. This fluctuation in the stress change behavior is further explored through numerical simulations in the following section.

4.2.3 Numerical verification

4.2.3.1 Finite element modeling

The three-dimensional numerical simulations are carried out in the *Solid Mechanics* interface under Structural Mechanics Module in the FE software COMSOL Multiphysics 5.4a. A butt-welded tensile specimen is constructed replicating the dimensions of the specimen used in the experiment as shown in Figure 4.13. A fixed constraint is provided at one end, while a load is applied at the free end to generate a stress of 200MPa, the largest stress applied in the experiment.

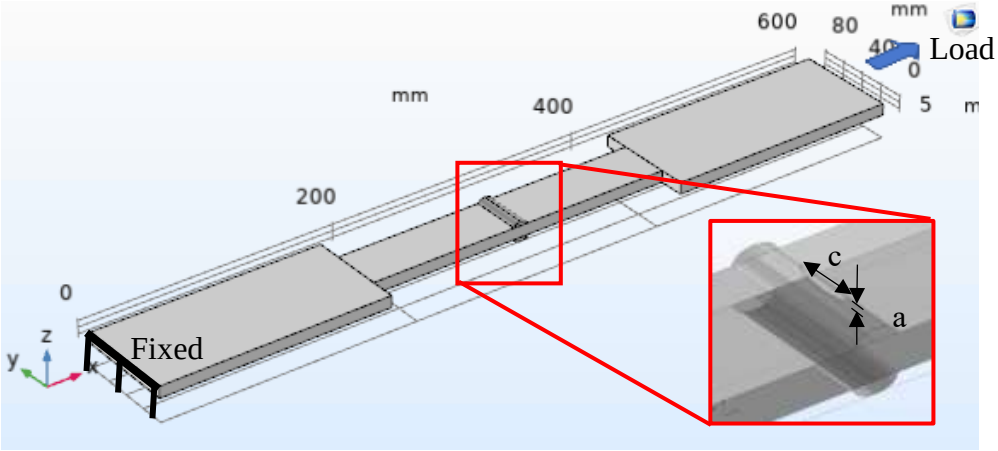

Figure 4.13 Numerical model of the butt-welded tensile specimen with cracks

Then, three cracks of elliptical shape, which resemble the real cracks from the experiment the most, are introduced into the specimen near the weld toe at a location equivalent to the location

C in the experiment as shown in the embedded picture in Figure 4.12. The crack is also offset from the center of the specimen, as was formed in the experiment. The cracks were modelled with an elliptical shape with a uniform width as in Wang et al. (2013) [58], which similarly models the thermal fatigue cracks, also in COMSOL. It is to be emphasized that the purpose of the current study is to obtain the stress change at the surface near the weld toe by using eddy current testing due to the presence of crack rather than the fracture mechanics modeling of crack formation and propagation. Therefore, singularity at the crack tip has not been considered in the present study. The cracks-1, 2, and 3 are simply the representation of three different crack sizes that will form during the crack propagation.

The letters *c* and *a*, denoting the crack length and depth, respectively, are given in Table 4.1, while a crack width of 0.1 mm is adopted. The Crack-1 and Crack-2 are the cracks formed after the 450, 000 and 500,000 main cycles, respectively, while Crack-3 corresponds to the fracture surface formed before reaching 550,000 main cycles. The built-in material property *Steel AISI-4340* with Young's modulus of 2.05×10^5 MPa, density of 7,850 kg/m^3, and Poisson's ratio of 0.28 has been assigned to the tensile specimen domain. The *Free tetrahedral* mesh with the minimum and maximum element size of 0.1 mm to 10 mm was assigned to the entire domain.

Table 4.1 Crack dimensions

	c (mm)	**a(mm)**
Crack-1	15.85	2.3
Crack-2	22.25	3.5
Crack-3	36.45	8.35

4.2.3.2 Results and discussion

Figures 4.14 and 4.15 corresponding to the top and cross-sectional view along the center of the specimen depict the stress distribution change near the weld toe at location C, the red and blue shading indicating high and low stresses, respectively. It can be seen from Figures 4.14 (b) and 4.15 (b) that the maximum stress occurs at the weld toe in absence of any crack and decreases as the distance from the weld toe increases, which is a known phenomenon. However, after the formation of Crack-1, the stress at the surface at location C is reduced drastically and increases with the distance from the weld toe. This has been illustrated in Figure 4.16, summarizing the difference between the stress distribution along the weld toe before and after the formation of crack. This agrees with the stress distribution change shown in Figure 1.5 and thus verifies that the numerical model of the butt-welded tensile specimen has been properly formulated.

When Crack-1 is introduced (Figure 4.14 (c) and 4.15 (c)), the stress at location C decreases drastically to low stress condition indicated by the blue shading, and the stress seem to be concentrated at the crack edges. As the crack continues to grow from Crack-1 to Crack-2 (Figures 4.14 and 4.15 (d-e)), it is seen that the stress at location C is still in low stress region but shows a significantly large increase as the crack size grows from Crack-2 to Crack-3. This can be depicted quantitatively by plotting the stress values at location C, at the center of the specimen, as shown in Figure 4.17.

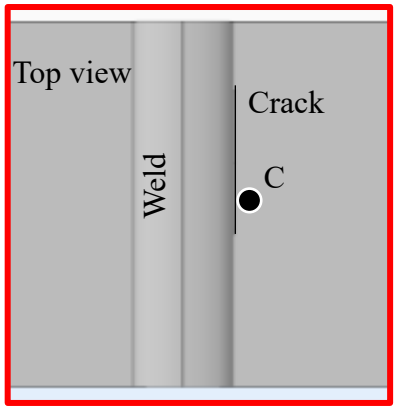

(a)

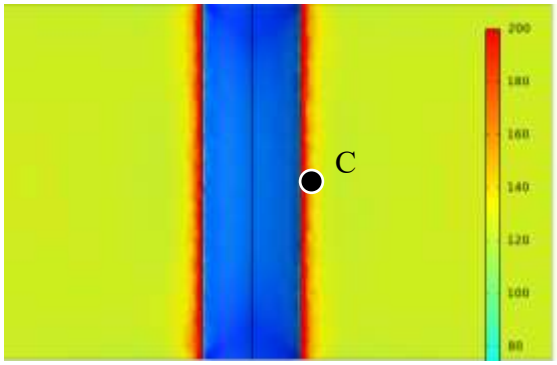

(b)

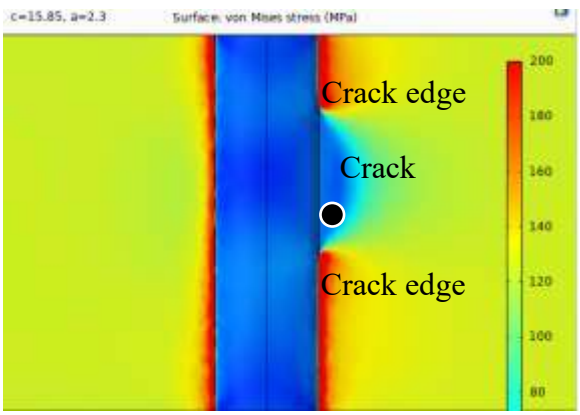

(c)

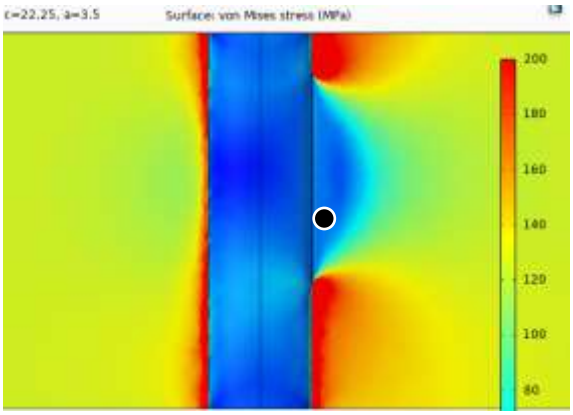

(d)

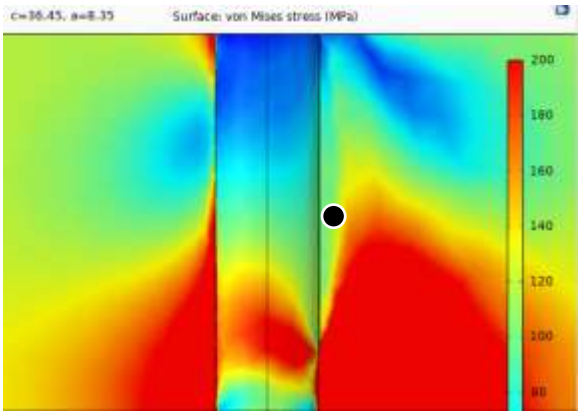

(e)

Figure 4.14 (a) Top view of the specimen with crack and location C near the weld toe, Stress distribution at location C (b) in absence of crack and due to the presence of cracks (c) Crack-1, (d) Crack-2, and (e) Crack-3.

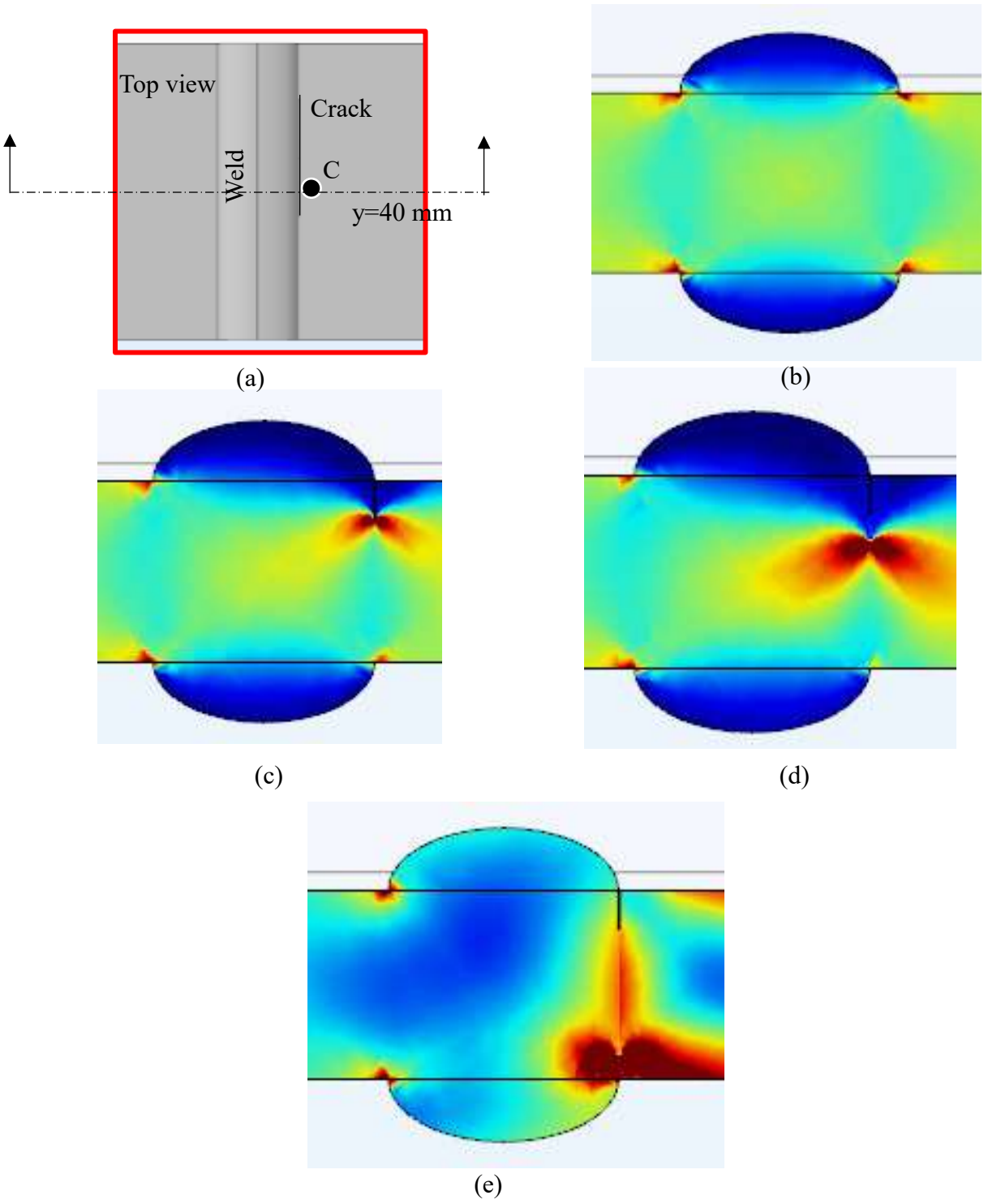

Figure 4.15 (a) Cross-section through the specimen center, i.e. y=40mm showing Stress distribution (b) in absence of crack and due to the presence of cracks (c) Crack-1, (d) Crack-2, and (e) Crack-3.

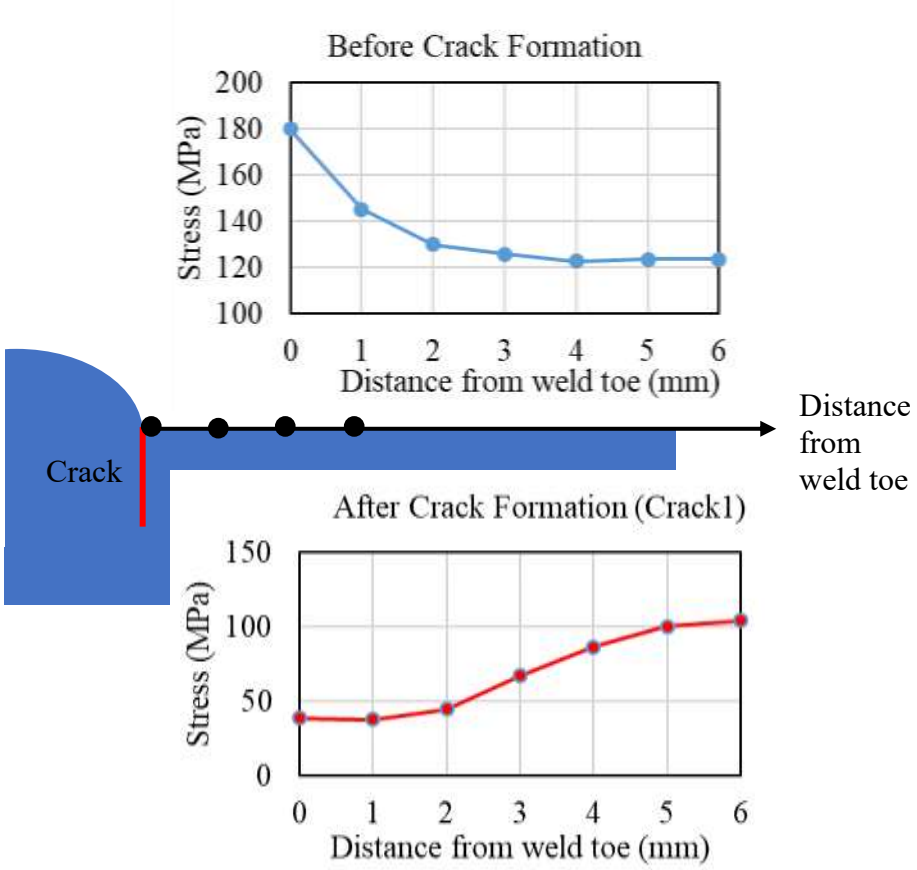

Figure 4.16 Stress change behavior before and after the formation of crack.

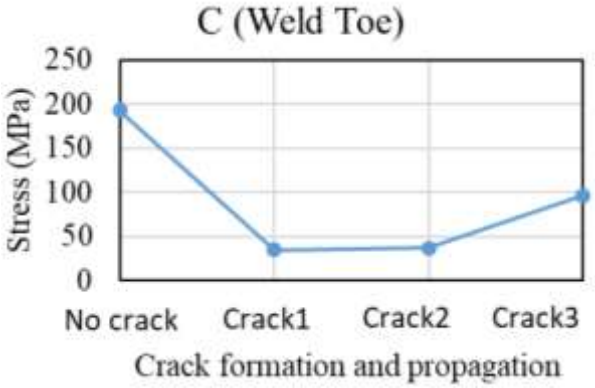

Figure 4.17 Stress change at location C near the weld toe at different stages of crack formation and propagation.

Figure 4.17 shows that the stress drops suddenly when the crack is formed and gradually rises as the crack grows, showing a sharp increase at the largest crack. As described before, the stress decreases suddenly due to crack formation as the stress is no longer transferred between the crack faces, which are not in contact. However, as the crack size grows, the remaining cross-sectional area that bears the stress is reduced and the stress increases again at the largest crack size, showing a sharp increase.

Nevertheless, it is to be noted that the eddy current probe will give an averaged stress value in the detectable area beneath the probe, usually equivalent to its diameter, and not the point stress as shown in Figure 4.17. Therefore, the stress values at four points located around the probe diameter (Figure 4.18(a)) were averaged to observe the stress variation due to the formation and propagation of crack, closer to how an eddy current probe would obtain the voltage values, as shown in Figure 4.18 (b), where point C1 is equivalent to point C in Figure 4.14 (a).

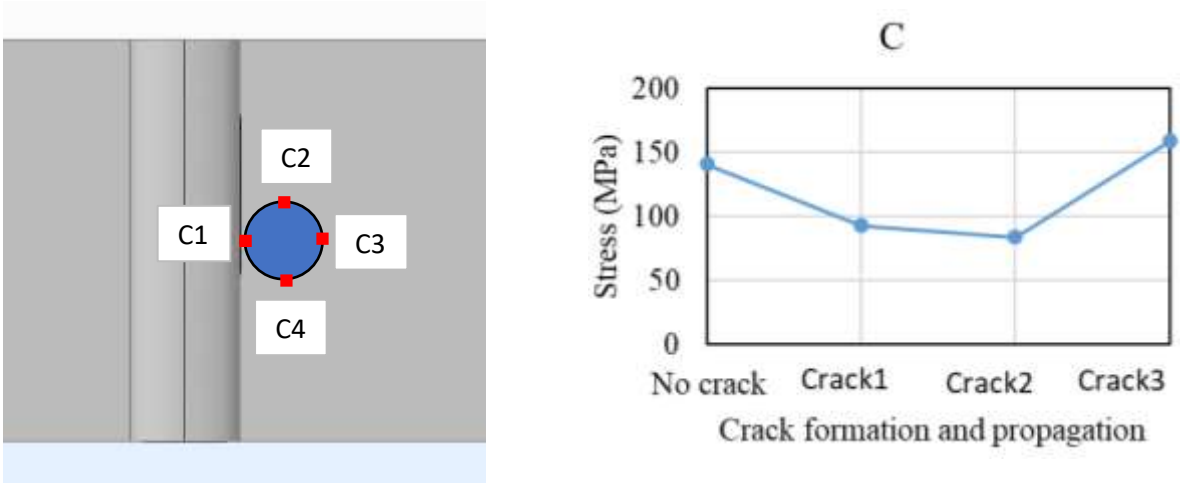

(a) (b)

Figure 4.18 (a) Averaging of stress values at four points near the weld toe at location C, (b) Averaged Stress change at location C near the weld toe at different stages of crack formation and propagation.

It can be seen from Figure 4.18 (b) that the stress drops suddenly as the crack forms, although quite not as much as in case of point stress measurement (Figure 4.17). Furthermore, unlike shown in Figure 4.17, the stress continues to decrease albeit slowly as the crack size grows from Crack-1 to Crack-2, and shows the sharp rise only at the largest crack size of Crack-3. This implies that with the use of a point probe or a smaller diameter probe, a sharper and clearer decrease in stress due to the crack formation can be observed. Therefore, the selection of a suitable probe size depends on the trade-off between sharper and clearer indication of fatigue cracking and the influence of lift-offs.

On the other hand, this behavior could not be observed in the experiment results. This is because the above results correspond to the measurement carried out at location C, lying at the exact center of the specimen. If the stress distribution is observed through another section that passes through edge of the first crack but passes through non-contact zone of the following crack, then the stress value will first increase from the no-crack state to crack formation and then decrease again between the formations of two consecutive cracks. This is illustrated in Figure 4.19 for the stress variation along section y = 35 mm and y = 55 mm for No crack to Cracks-1, 2, and 3, where the stress measurement locations fall alternately under high stress concentration, crack edge zone and low stress, non-contact zone between crack faces for the consecutive cracks. Hence, the occurrence of fluctuation in stress due to the formation and propagation of crack has also been numerically verified.

Therefore, based on the stress fluctuation behavior near the weld toe, there is a possibility of detection of fatigue crack using eddy current based stress measurement.

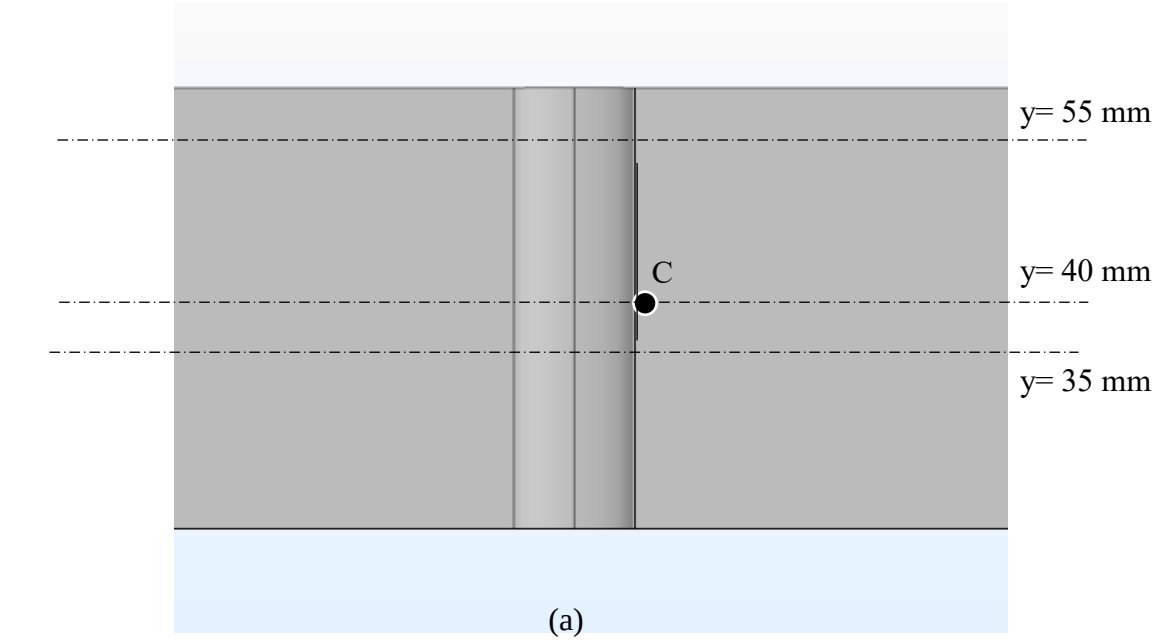

(a)

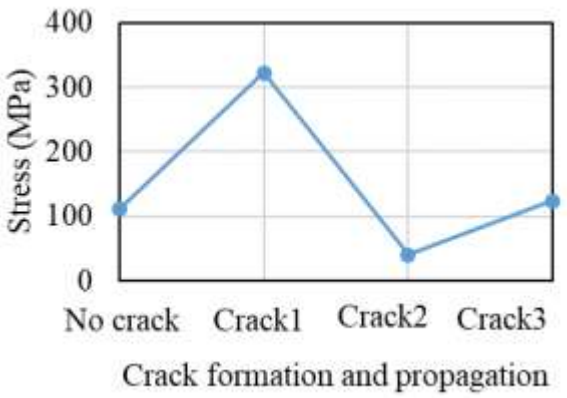

(b)

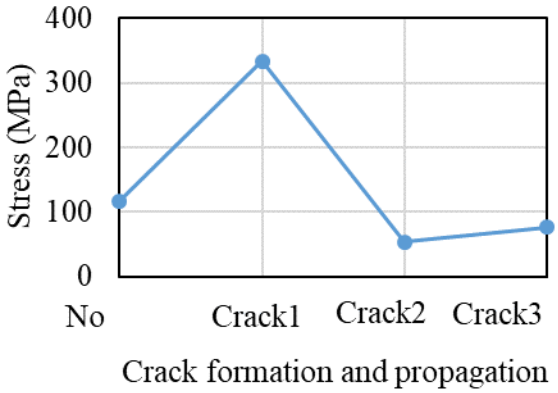

(c)

Figure 4.19 (a) Cross-section at different locations passing through a crack and un-cracked zone and Stress variation at cross-sections along (b) y= 35 mm and (c) y=55mm at different stages of crack formation and propagation.

4.3 Determination of bolt tension variation using eddy current based stress measurement

The feasibility of application of eddy current based stress measurement in determining the tension in the bolt based on the stress variation at the bolt head at different bolt tensions is first confirmed through numerical simulation of a bolt subjected to tensile load, representative of the bolt tension. After affirming that stress change occurs at the bolt head due to the change in bolt tension, which can then be detected by eddy current, the experimental work is carried out, where the voltage by detected by the eddy current probe at the bolt head changes due to the change in stress at the bolt head at different bolt tensions. The study is further tested for future applicability in determination of corrosion in bolt head.

4.3.1 Numerical simulation

4.3.1.1 Finite element modeling

The three-dimensional numerical simulations are carried out in Structural Mechanics module of COMSOL Multiphysics 5.4a, by constructing a numerical model of a high-strength bolt and washer assembly that will be used in the experiment. The dimensions of the bolt and washer are shown in Figure 4.20 (a); the bolt head thickness, shaft length, and shaft diameter are 13mm, 80mm, and 22 mm, respectively, while a washer 4mm thick is also modelled to supply the fixed constraint to replicate the condition nearest to the actual one in a bolted connection (Figure 4.20 (b)). The built-in material *Structural Steel* with Young's modulus of elasticity $2x10^5$ MPa, density 7850 kg/m^3, and Poisson's ratio of 0.3 was assigned to the domains, while a predefined *Free Tetrahedral* mesh with default minimum and maximum element sizes 1.67 mm to 9.3mm were used. Varying loads of 10, 20, 30, 40, 50, 75, 100, 125, 150, 175, 200, and 205 kN are applied as

boundary load at the shaft end (Figure 4.20 (c)), representative of the bolt tension, whereby the change in stress at the bolt head at different bolt tensions is confirmed. A parametric study is also conducted where the bolt head thickness is decreased from 13mm to 7.5mm to investigate the effect of reduction in bolt head thickness due to corrosion on the stress at the bolt head.

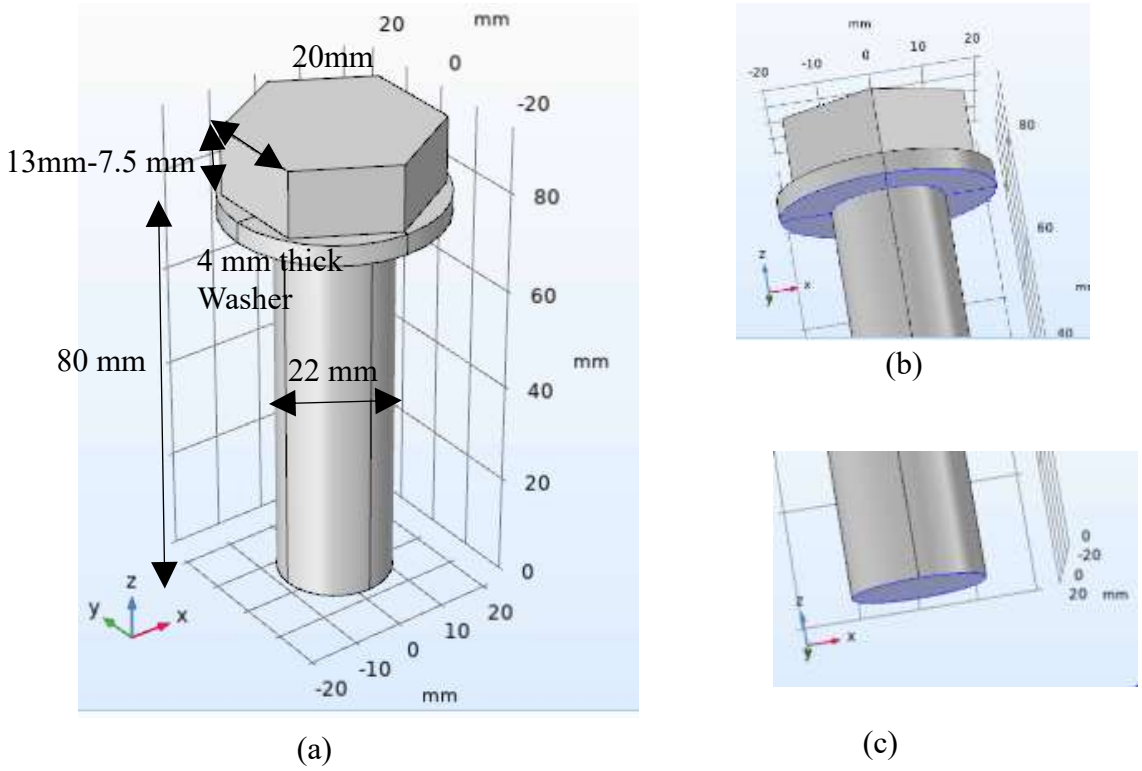

Figure 4.20 (a) Numerical model of the bolt with its dimensions, (b) Fixed constraint applied at the bottom of the washer domain, and (c) Boundary load applied at the end of bolt shaft.

4.3.1.2 Results and discussion

The stress at four locations lying on the probe diameter (ϕ=10 mm) and at the center are averaged to obtain the stress values at the top of the bolt head corresponding to the change in bolt tension, as shown in Figure 4.21 (a). The relationship between stress variation at the bolt head due to the

change in bolt tension is depicted in Figure 4.21 (b), indicating a linear relationship. It is clearly observed that on reduction of the bolt tension, the stress induced at the bolt head also decreases. Therefore, it is possible to apply the eddy current based stress measurement to gauge the change in bolt tension corresponding to the change in stress at the top of the bolt head.

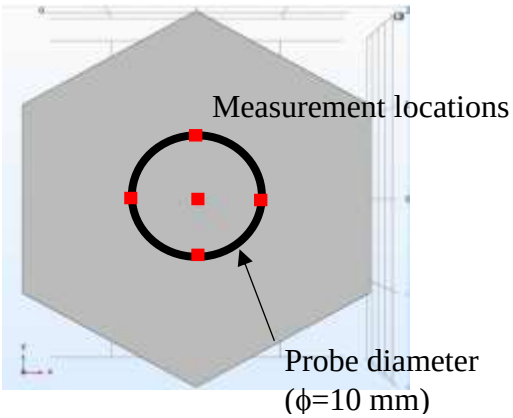

(a)

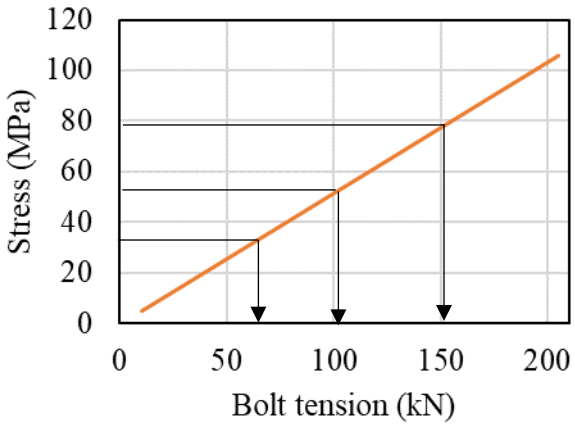

(b)

Figure 4.21 (a) Stress measurement locations around the probe diameter at the top of bolt and (b) Variation of stress at the bolt head corresponding to bolt tension.

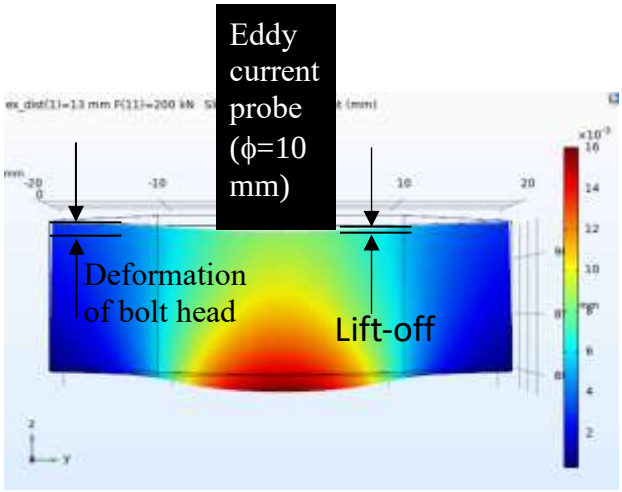

(a)

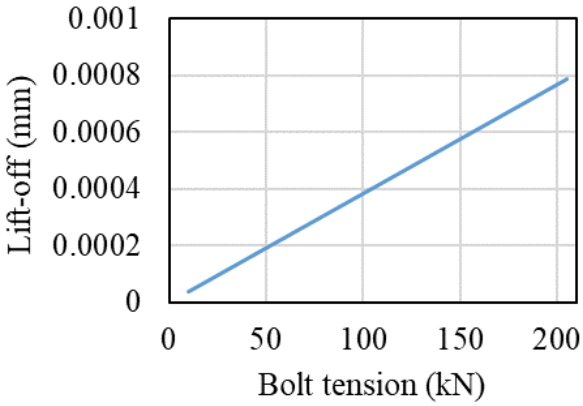

(b)

Figure 4.22 (a) Cross-section through center of the bolt head showing its deformation, and lift-off w.r.t. the eddy current probe location, (b) Variation of lift-off of the probe due to the bolt head deformation at different bolt tension.

With respect to the effect of lift-off, the deformation of the bolt head is evaluated and the lift-offs are calculated from the distance between the eddy current probe to the deformed surface as shown in Figure 4.22 (a). The adjoining figure 4.22 (a) shows the variation of lift-off due to the bolt head deformation at a given bolt tension. It is to be noted that as the bolt tension decreases from 205 kN – 10 kN, the stress at the bolt head decreases from about 106 MPa to 5 MPa (Figure 4.21 (b)), which is a significant change corresponding to the change in bolt tension. On the other hand, the maximum lift-off generated at the bolt head is about 0.0008 mm for the largest bolt tension of 205 kN (Figure 4.22 (b)), which is negligible compared to the variation of stress at the bolt head. Hence, the effect of change in stress at the bolt head is found to be dominant rather than the effects of lift-off in this case. Therefore, eddy current based stress measurement can be applied to gauge the bolt tension corresponding to the change in stress at the top of the bolt head and the effect of lift-off has not been considered in the experimental work.

Next, the effect of reduction in bolt head thickness due to corrosion on the stress change at the bolt head is also investigated for future prospect of determination of extent of corrosion in a bolted connection. Figures 4.23 shows the change in stress at the bolt head due to the reduction of bolt head thickness by 0-5.5mm, corresponding to the variation of bolt head thickness from 13-7.5 mm at the bolt tension of 200 kN. It is clearly seen that there is significant increase in stress at the bolt head due to the reduction of bolt head thickness. Therefore, the corrosion of bolt head also affects the eddy current based stress measurement and future works could be done to apply this method to determine the corrosion extent in the bolt head and the mutual effects of corrosion in the bolt tension change and vice-versa.

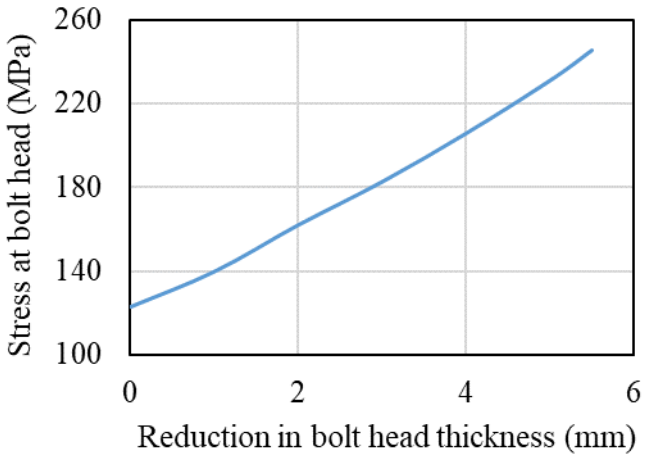

Figure 4.23 (a) Variation of stress at the bolt head corresponding to the reduction in bolt head thickness due to corrosion.

4.3.2 Experimental procedure

In this experimental campaign, tensile stress is introduced into a high-strength bolt of M22 grade fit into Skidmore-Wilhelm bolt tension calibrator (MZ-100) mounted on an I-beam using wing screws, with the help of a hand torque wrench, as shown in Figure 4.24 (a). The adaptor plate and adaptor bushing specific to the bolt diameter are mounted on the front and back of the unit, respectively (Figure 4.24 (b) and (c)). The threaded end of the bolt is inserted through the adaptor bushing, from the back side of the calibrator and the washer and nut are installed on the plate side. Therefore, a bolted joint is simulated with this assembly of adaptor plate, adaptor bushing, bolt, washer, and nut. The bolt assembly is now snug-tightened using the torque wrench such that the needle of the gauge just moves. From this point on, the torque is applied such that 10, 20, 30, 40, 50, 75, 100, 125, 150, 175, 200, 205 kN of tensile load is induced into bolt, as indicated by gauge.

On the other hand, for the eddy current based stress measurement, the eddy current probe 700P11A is placed at the center of bolt head, held in place by a fixing jig as shown in Figure 4.24

(c), to obtain the voltage values at different tensile loads in the bolt. It is connected to the signal generator, Ectane, and the Magnifi software is used to specify the excitation frequency and input voltage to the probe and collect the data for the detected voltage value corresponding to each tensile load generated in the bolt. As in the previous experiments, an excitation frequency of 5kHz and input voltage of 5V is supplied to the probe 700P11A, while the lift-off is maintained at 0 mm. The probe is balanced to zero first at 0 kN tensile load in the bolt and the detected voltages are then measured for the subsequent tension in the bolt.

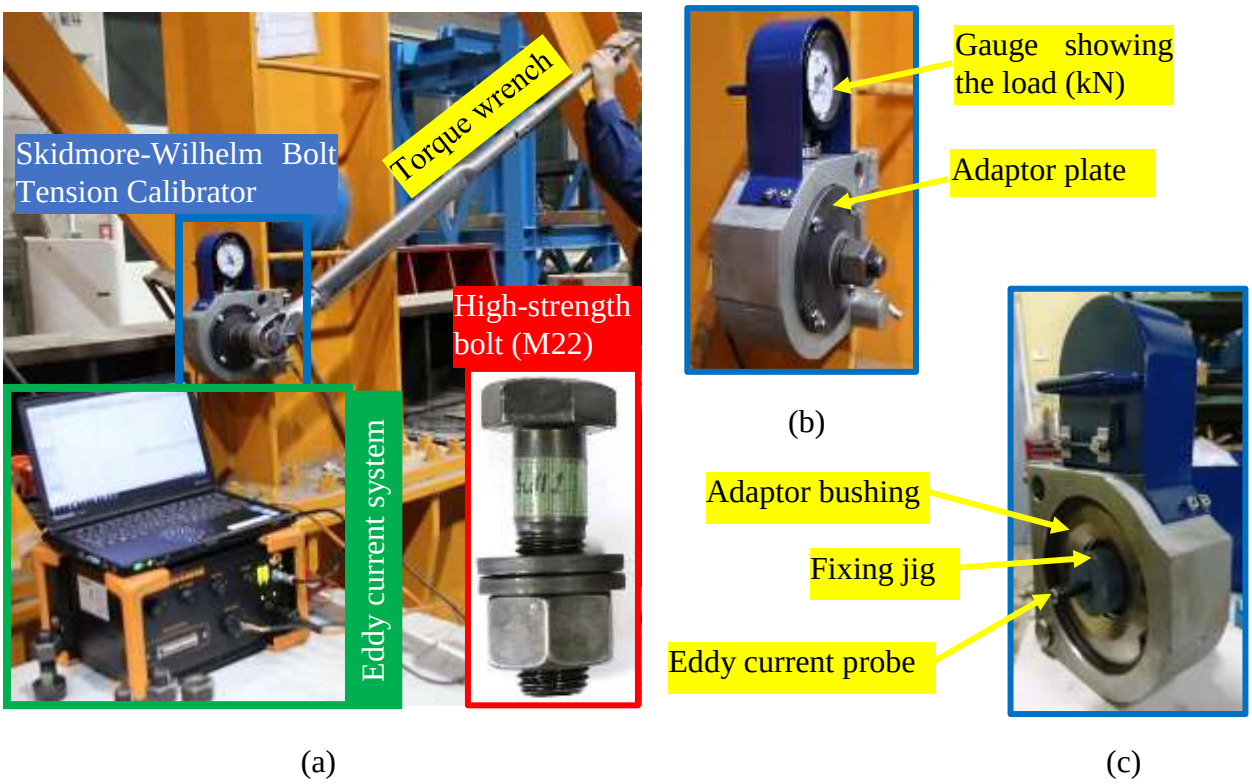

Figure 4.24 (a) Experimental setup for characterization of bolt tension using eddy current based stress measurement, (b) Front and (c) Back sides of the Skidmore-Wilhelm Bolt Tension Calibrator.

In addition to this, another high-strength bolt of the same grade (M22) but with a corroded bolt head, the thickness of which has been reduced to 7.5mm from the original thickness of 13 mm, is tested in order to evaluate the mutual effect of corrosion of bolt head and the tension in the bolt (Figure 4.25). As mentioned by Ahn et al., 2016 [25], the frictional force developed between the connected plates due to the clamping force induced by the bolt tightening, is affected by the reduction of sectional resistance caused by corrosion of the bolt head. The corrosion of the bolt head can occur in three ways – sectional corrosion as in [25, 26], thickness reduction, and a combination of two. In the present experimental work, the reduction in bolt head thickness is considered to represent the corrosion for ease of fabrication of the bolt specimen. Then, the eddy current based stress measurements are carried out for the bolt with reduced bolt head thickness similarly with the tensile load variation from 0 to 205 kN, with the 700P11A bolt at an excitation frequency of 5kHz, input voltage of 5V and 0 mm lift-off. The yellow circles show the location of eddy current probe on the bolt head.

Figure 4.25 Side and top views of the M22 grade, high-strength bolts with bolt head thickness of (a) 13 mm and (b) 7.5 mm.

4.3.3 Results and discussion

Figure 4.26 shows the change in absolute voltage detected by the eddy current probe 700P11A for the variation in bolt tension; the detected voltage increases with the increasing bolt tension and vice-versa. Conversely, the reduction in bolt tension causes decrease in the absolute voltage detected by the probe. This also agrees with the numerical results (Figure 4.21), where the stress at the bolt head decreases due to the decrease in bolt tension. Hence, the reduction in bolt tension due to relaxation, self-loosening, vibration, etc. which are inevitable in the field, can therefore be evaluated using the eddy current based stress measurement. Apart from a slight scatter, the relationship between the detected voltage and the bolt tension seems to be linear.

Therefore, if calibration is carried out for the high-strength bolt of particular grade in the laboratory for a given bolt tension, then the remaining tension value in a bolt in the field can be determined through back calculation of the detected voltage from the calibration data. Hence, eddy current based stress measurement can also be applied to determine the remaining bolt tension and ensure that it is not below the minimum requirements, thus precluding failure of bolted connections due to self-loosening, slip, etc.

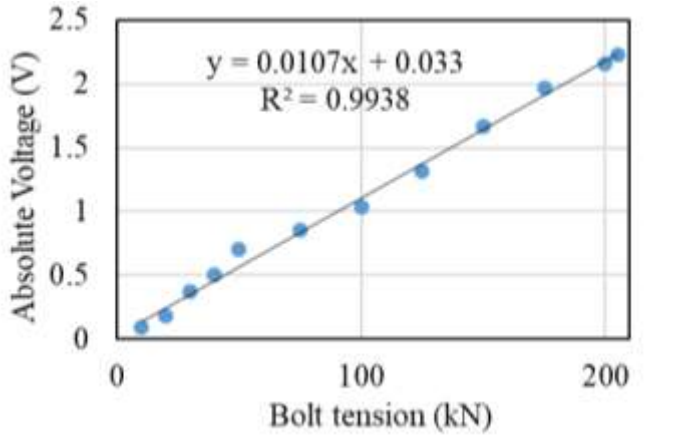

Figure 4.26 Detected voltage vs bolt tension obtained from eddy current based stress measurement.

Next, Figure 4.27 depicts the change in detected voltage values for the bolt with un-corroded head of 13 mm thickness and a corroded bolt whose bolt head thickness was reduced to 7.5 mm, corresponding to the same bolt tension. The bolt with reduced head thickness shows significantly higher voltage values for the same bolt tension, indicating that the corrosion affects the evaluation of bolt tension using eddy current based stress measurement. Conversely, the bolt tension is reduced due to the corrosion of the bolt head as evident by the smaller bolt tension for the same detected voltage.

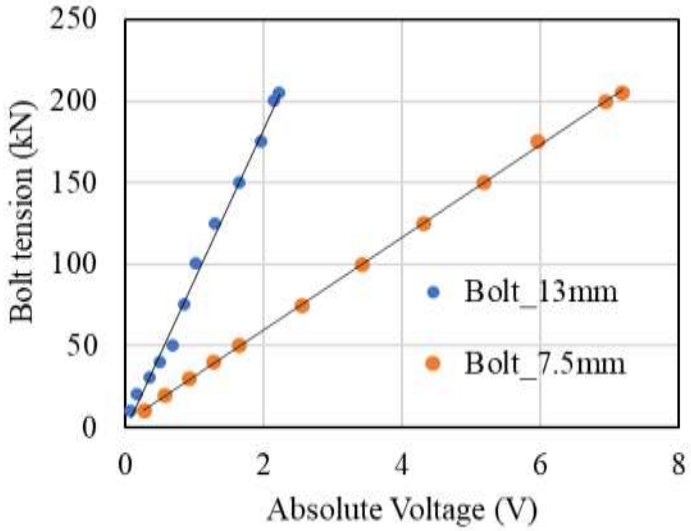

Figure 4.27 Effect of corrosion of bolt head on the detected voltage values.

Similar research has been carried out by Tai et al. (2018) [31] by reducing the bolt head thickness representative of corrosion and measured the strain at the bolt head using strain gauge (Figure 4.28(a)). Thus obtained relationship is similar to the experimental results in the present study except that eddy current response has been used instead of strain at the bolt head as shown in Figure 4.28 (b). Hence, the mutual effects of corrosion and reduction in bolt tension can be evaluated using eddy current based stress measurement.

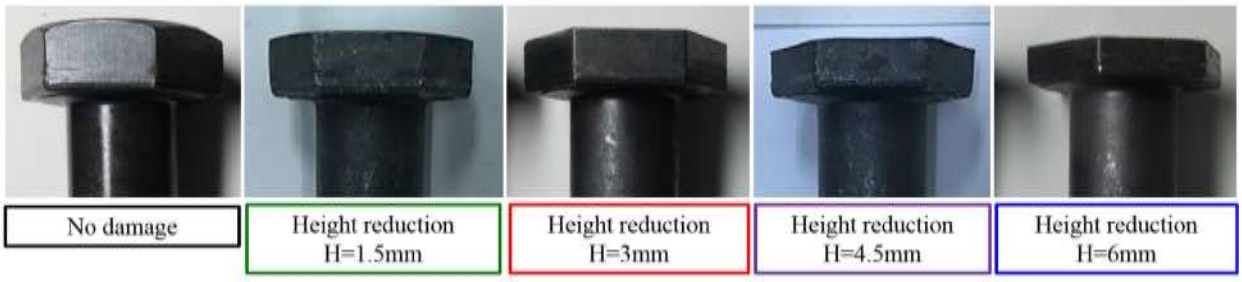

(a)

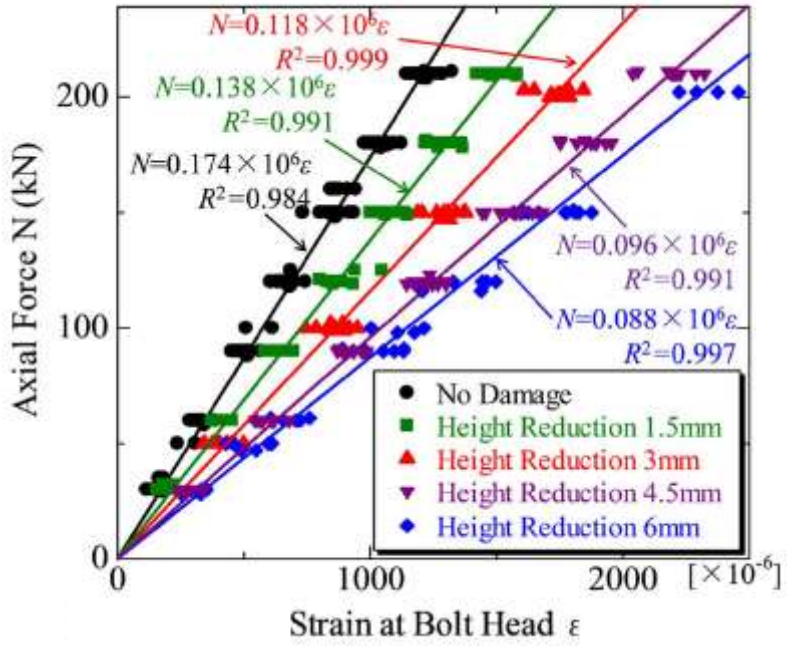

(b)

Figure 4.28 (a) Height reduction of bolt head and (b) Relationship between axial force and strain at bolt head [31].

4.4 Summary

Hence, in the present chapter, two different applications of eddy current based stress measurement have been experimentally verified. – to detect the fatigue crack and to determine the bolt tension, based on the stress change near the weld toe and on the bolt head, respectively. The tensile test was first used to calibrate the absolute voltage detected by the eddy current probe, 700P11A, to

the tensile stress applied to the steel specimen, which was then used to determine the stress variation near the weld toe at four locations A, B, C, and D after each loading cycle of the butt-welded tensile specimen under fatigue test. Based on the observation of the fracture surface with beach marks and the stress variation obtained from the eddy current based stress measurement at location C, where the crack is deduced to have initiated from, the stress change behavior due to the formation and propagation of crack is obtained. This pattern of behavior is a valuable information that can be applied in detecting the crack based on the stress variation near the weld due to the formation of crack, during the monitoring. The stress change behavior obtained from the experimental work has also been verified through numerical simulations.

On the other hand, the numerical simulations first confirmed the stress change in the bolt head due to different bolt tensions, whereby the possibility of application of eddy current based stress measurement to the bolt tension through the stress change at the bolt head is verified. Then, in the experiment, the absolute voltage detected by the eddy current probe, 700P11A, placed on the top of the bolt head was calibrated to the tensile load induced into the bolt using Skidmore-Wilhelm bolt tensile calibrator with a torque wrench, confirming the possibility of using eddy current based stress measurement for the detection of change in the bolt tension. Furthermore, it was also confirmed that the eddy current based stress measurement can be used to detect the mutual effects of corrosion and the bolt tension. Hence, the robustness of the eddy current based stress measurement on applicability in different fields was verified through these experimental campaigns.

Chapter 5 Conclusions and Recommendations

This chapter summarizes the conclusions based on the results obtained in each chapter and proposes future works that can be done to extend the present study.

5.1 Conclusions

The following conclusions can be drawn based on the results of each chapter in the present study:

Chapter 2

A step-wise methodology was devised and applied to estimate the corrosion profile of a corroded steel plate based on the probe lift-offs, with and without protective FRP or Titanium covers, when the only accessible side to the eddy current probe is rough. It was concluded that optimization of the probe geometry and approximation of the lift-off estimation curve should be taken into account to improve the estimation accuracy of the corrosion profile. Furthermore, the material loss obtained from the corrosion profile can be used to judge the severity of the corrosion by using corrosion severity histogram.

Chapter 3

A methodology to conduct eddy current based stress measurement was devised by investigating the effect on the eddy current response due to change in stress of a steel plate, in addition to other influential parameters such as lift-off, excitation frequency, and probe size, through numerical simulations. Phase diagram is proposed as a new, concise method to observe the simultaneous variation of relative permeability (representative of stress) and lift-off at an excitation frequency for a probe. It proved to be invaluable as a means to select suitable excitation frequency and probe size based on the criteria of uniform trend of change of relative permeability for different lift-offs and sufficient sensitivity to this change even at larger lift-offs, respectively. The concept and flow developed in this chapter contributed in formulating the experimental campaign for the following Chapter 4.

Chapter 4

Two experimental investigations were carried out for applying the concept of eddy current based stress measurement for detection of fatigue cracking and determination of bolt tension and its reduction due to corrosion. It is found that based on the change of stress near the weld toe of the butt-welded tensile specimen, the formation of crack and its propagation can be deduced, which can be used as benchmark behavior in the detection of crack and the stage it is at. This experimental result was also verified numerically to ascertain that this change of stress behavior is correct. On the other hand, based on the calibration of eddy current index to the known value of bolt tension, the loss of bolt tension due to the corrosion simulated by the reduction in thickness of the bolt head could be analyzed. Hence, two applications of the eddy current based stress measurement were tested, thus confirming its robustness.

Hence, different viable, eddy current based methods have been devised addressing specific need such as rough, accessible side to the eddy current probe and wider need such as detection of fatigue cracking, bolt tension, etc. by a robust method of eddy current based stress measurement. The proposed methods have been numerically and experimentally verified with the indication of possibility of their application in the real field.

5.2 Recommendations

Chapter 2.

Further works in this chapter would be the fabrication of the probe with optimized geometry to conduct an experiment or field investigation and design of a probe mount, e.g. a cylindrical probe mount fitted around a steel pipe pile, which serves as a datum as the probe moves around its circumference to estimate the corrosion profile. In addition, the design of the current probe could be extended to an array probe to cover more inspection area. On the other hand, a flux ball [89] or spherical coil sensor [90] can be explored for further improvement in accuracy with the possibility of obtaining exact lift-off at a point, to evaluate the exact minimum thickness since they theoretically measure the magnetic field value at a point rather than the average value by cylindrical coils used in conventional eddy current probes. The current study can also be extended to obtain the corrosion on the backside in case of a girder, by using an additional larger probe with lower frequency range that can penetrate through the thickness to reach the corroded backside.

Chapter 3.

This chapter can be extended further by taking into account the direct effect of stress, instead of using relative permeability as a measure of stress, by employing two physics modules – S*olid mechanics* and *Magnetic fields* to model stress and eddy current, respectively, and a multi-physics coupling between the two modules called *Magnetostriction* in COMSOL Multiphysics 5.4a. This would contribute in making the numerical simulation results more comparable to the experimental results among other factors causing discrepancies between the numerical and experimental results.

Chapter 4.

In this chapter, only qualitative analyses have been conducted for detection of fatigue cracking and determination of bolt tension as a first step in verifying the applicability of eddy current based stress measurement. Nevertheless, the possibility of extension of the present study into quantitative analyses can be clearly seen for not only detection but sizing of the fatigue cracks with calibration to the artificially manufactured defects based on the stress change evaluation for each defect size. As for its application in the field, the sweeping of the probe along the weld length is recommended to observe the change in stress along the weld for detection of presence of crack. On the other hand, for determination of the remaining bolt tension, particularly in existing steel structures with older grade of the bolts, the material property can be incorporated additionally into the calibration data for eddy current index to the bolt tension. For this, a core sample can be taken from the actual bolt that retains the original state of the bolt, which can then be tested in lab for its material properties. Hence, with more rigorous calibration including the effect of a combination of sectional and thickness loss of bolt head, the eddy current based stress measurement for bolt tension shows a good possibility of application in the field in future.

REFERENCES

[1] Ahn, J. H., Kainuma, S., Yasui, F., & Takehiro, I. (2013). Repair method and residual bearing strength evaluation of a locally corroded plate girder at support. *Engineering Failure Analysis, 33*, 398-418.

[2] Appuhamy, J. R. S., Ohga, M., Kaita, T., & Dissanayake, R. (2011). Reduction of ultimate strength due to corrosion: A finite element computational method. *International Journal of Engineering* (IJE), *5*(*2*), 194-207.

[3] Kasai, N., Mori, S., Tamura, K., Sekine, K., Tsuchida, T., & Serizawa, Y. (2016). Predicting maximum depth of corrosion using extreme value analysis and Bayesian inference. *International Journal of Pressure Vessels and Piping*, *146*, 129-134.

[4] Khurram, N., Sasaki, E., Katsuchi, H., & Yamada, H. (2014). Experimental and numerical evaluation of bearing capacity of steel plate girder affected by end panel corrosion. *International Journal of Steel Structures*, *14*(3), 659-676.

[5] Melchers, R. E. (2005). The effect of corrosion on the structural reliability of steel offshore structures. *Corrosion science*, *47*(10), 2391-2410.

[6] Yamaguchi, E., & Akagi, T (2012, October). Influence of corrosion of transverse stiffener at support on load-carrying capacity of steel girder. In *Proceedings of the 28th Japan-US Bridge Engineering Workshop* (pp.137-147). Portland, OR. Retrieved from https://www.pwri.go.jp/eng/ujnr/tc/g/pdf/28/28-4-3_Yamaguchi.pdf.

[7] Koch, G., Varney, J., Thompson, N., Moghissi, O., Gould, M., & Payer, J. (2016). *International measures of prevention, application, and economics of corrosion technologies study*. Houston, TX: NACE International IMPACT Report.

[8] Akutsu, A., Sasaki, E., Ebisawa, Y., & Tamura, H. (2017). Analysis of corrosion damage condition of steel members using low frequency eddy current testing. *Journal of Japan Society of Civil Engineers, Ser. A1 (Structural Engineering & Earthquake Engineering (SE/EE))*, *73*(2), 387-398.

[9] Akutsu, A., Sasaki, E., & Tamura, H. (2018). Development of an advanced corrosion damage evaluation method for steel members focused on phase characteristics of low frequency eddy current. *Journal of Japan Society of Civil Engineers, Ser. A1 (Structural Engineering & Earthquake Engineering (SE/EE))*, *74*(1), 145-156.

[10] Cheng, W. (2017). Thickness measurement of metal plates using swept-frequency eddy current testing and impedance normalization. *IEEE Sensors Journal*, *17*(14), 4558-4569.

[11] Fan, M., Cao, B., Tian, G., Ye, B., & Li, W. (2016). Thickness measurement using liftoff point of intersection in pulsed eddy current responses for elimination of liftoff effect. *Sensors and Actuators A: Physical*, *251*, 66-74.

[12] Fan, M., Cao, B., Sunny, A. I., Li, W., Tian, G., & Ye, B. (2017). Pulsed eddy current thickness measurement using phase features immune to liftoff effect. *NDT & E International*, *86*, 123-131.

[13] Lu, M., Yin, L., Peyton, A. J., & Yin, W. (2016). A novel compensation algorithm for thickness measurement immune to lift-off variations using eddy current method. *IEEE Transactions on Instrumentation and Measurement*, *65*(12), 2773-2779.

[14] Yin, W., & Peyton, A. J. (2007). Thickness measurement of non-magnetic plates using multi-frequency eddy current sensors. *NDT & E International*, *40*(1), 43-48.

[15] Yin, W., Peyton, A. J., & Dickinson, S. J. (2004). Simultaneous measurement of distance and thickness of a thin metal plate with an electromagnetic sensor using a simplified model. *IEEE Transactions on Instrumentation and Measurement*, *53*(4), 1335-1338.

[16] Hamada, H., Yamaji, T., & Akira, Y. (2011, July). Corrosion protection for steel pipe piles and sheet piles. *Steel Construction Today and Tomorrow*, *33*. Retrieved from http://www.jisf.or.jp/en/activity/sctt/documents/SCTT33.pdf

[17] Hashimoto, R., Imai, A., Imafuku, K., Ganaha, Y., Kawase, Y. & Furukawa, M. (2017). *High-durability corrosion protection of marine steel structures using titanium covers* (Report No. 115). Retrieved from Nippon Steel & Sumitomo Metal website: http://www.nssmc.com/tech/report/nssmc/pdf/115-12.pdf

[18] Robers, M.A. & Scottini, R. (2002, June). *Pulsed eddy current in corrosion detection*. Paper presented at the 8th European Conference on Nondestructive Testing, Barcelona, Spain.

[19] Mirza, O., Milner L, & Mashiri F. (2018). Experimental investigation of retrofitting techniques for steel bridge girders subject to fatigue failure. *Journal of Steel Structures & Construction, 4*(138). doi: 10.4172/2472-0437.1000138

[20] Haghani, R., Al-Emrani, M., & Heshmati, M. (2012). Fatigue-prone details in steel bridges. *Buildings,2*(4), 456-476.

[21] Todorov, E. I., Mohr, W. C., & Lozev, M. G. (2008, February). Detection and sizing of fatigue cracks in steel welds with advanced eddy current techniques. In *AIP Conference Proceedings*, *975*(1), 1058-1065.

[22] Azizinamini, A., Power, E. H., Myers, G. F., Ozyildirim, H. C., Kline, E. S., Whitmore, D. W., & Mertz, D. R. (2013). Design guide for bridges for service life. *SHRP 2 Renewal Project R19A*, Transportation Research Board, Washington, DC.

[23] Cao, B., Ding, Y., Fang, Z., Geng, F., & Song, Y. (2019). Influence of Weld Parameters on the Fatigue Life of Deck-Rib Welding Details in Orthotropic Steel Decks Based on the Improved Stress Integration Approach. *Applied Sciences*, *9*(18), 3917.

[24] Du, F., Xu, C., Ren, H., & Yan, C. (2018). Structural Health Monitoring of Bolted Joints Using Guided Waves: A Review. *Structural Health Monitoring from Sensing to Processing*, 163.

[25] Ahn, J. H., Lee, J. M., Cheung, J. H., & Kim, I. T. (2016). Clamping force loss of high-strength bolts as a result of bolt head corrosion damage: Experimental research A. *Engineering Failure Analysis*, *59*, 509-525.

[26] Kim, I. T., Lee, J. M., Huh, J., & Ahn, J. H. (2016). Tensile behaviors of friction bolt connection with bolt head corrosion damage: Experimental research B. *Engineering Failure Analysis*, *59*, 526-543.

[27] Shah, J. K., Braga, H. B. F., Mukherjee, A., & Uy, B. (2019). Ultrasonic monitoring of corroding bolted joints. *Engineering Failure Analysis*, *102*, 7-19.

[28] Paolo, Z., Curtarello, A., Maiorana, E., & Pellegrino, C. (2017). Numerical analyses of corroded bolted connections. *Procedia Structural Integrity*, *5*, 592-599.

[29] Paolo, Z., Curtarello, A., Maiorana, E., Pellegrino, C., De Rossi, N., Savio, G., & Concheri, G. (2017). Influence of corrosion morphology on the Fatigue strength of Bolted joints. *Procedia Structural Integrity*, *5*, 409-415.

[30] Wang, T., Song, G., Liu, S., Li, Y., & Xiao, H. (2013). Review of bolted connection monitoring. *International Journal of Distributed Sensor Networks*, *9*(12), 871213.

[31] Tai, M., Shimozato, T., Nagamine, Y., Arizumi, Y., & Yabuki, T. (2018). Dependence of Residual Axial Force on Thickness and Shape in Corroded High-Strength Bolts. *Journal of Structural Engineering*, *144*(7), 04018069.

[32] Ocel, J. (2012). Feasibility of Nondestructive Crack Detection and Monitoring for Steel Bridges (Report No. FHWA-HRT-12-060). Retrieved from https://www.fhwa.dot.gov/publications/research/nde/12060/12060.pdf

[33] García-Martín, J., Gómez-Gil, J., & Vázquez-Sánchez, E. (2011). Non-destructive techniques based on eddy current testing. *Sensors, 11*(3), 2525-2565.

[34] Mi, B., Michaels, J. E., & Michaels, T. E. (2006). An ultrasonic method for dynamic monitoring of fatigue crack initiation and growth. *The Journal of the Acoustical Society of America, 119*(1), 74-85.

[35] Jeon, I., Lim, H. J., Liu, P., Park, B., Heinze, A., & Sohn, H. (2019). Fatigue crack detection in rotating steel shafts using noncontact ultrasonic modulation measurements. *Engineering Structures, 196*, 109293.

[36] Wang, R., Wu, Q., Yu, F., Okabe, Y., & Xiong, K. (2019). Nonlinear ultrasonic detection for evaluating fatigue crack in metal plate. Structural Health Monitoring, 18(3), 869-881.

[37] Camerini, C., Rebello, J., Braga, L., Santos, R., Chady, T., Psuj, G., & Pereira, G. (2018). In-Line Inspection Tool with Eddy Current Instrumentation for Fatigue Crack Detection. *Sensors, 18*(7), 2161.

[38] Ichinose, L. H., Kohno, Y., Kitada, T., & Matsumura, M. (2007). Applications of eddy current test to fatigue crack inspection of steel bridges. *MEMOIRS-FACULTY OF ENGINEERING OSAKA CITY UNIVERSITY, 48*, 57.

[39] Kyrgiazoglou, A., & Theodoulidis, T (2018, October). Simulation and experiments on the eddy current method to detect fatigue cracks in welds. *1st ICWNDT2018*, Athens, Greece.

[40] Sakagami, T. (2015). Remote nondestructive evaluation technique using infrared thermography for fatigue cracks in steel bridges. *Fatigue & Fracture of Engineering Materials & Structures, 38*(7), 755-779.

[41] Baek, S., Xue, W., Feng, M. Q., & Kwon, S. (2012). Nondestructive corrosion detection in RC through integrated heat induction and IR thermography. *Journal of Nondestructive Evaluation, 31*(2), 181-190.

[42] Shi, F., Wang, J., Cui, W., & Qin, L. (2019, October). The influence of different factors on acoustic emission signal in the process of monitoring steel corrosion. In *IOP Conference Series: Materials Science and Engineering*, *612*(3), pp. 032071, IOP Publishing.

[43] Barat, V., Marchenkov, A., & Elizarov, S. (2019). Estimation of Fatigue Crack AE Emissivity Based on the Palmer–Heald Model. *Applied Sciences, 9*(22), 4851.

[44] Ihn, J. B., & Chang, F. K. (2004). Detection and monitoring of hidden fatigue crack growth using a built-in piezoelectric sensor/actuator network: II. Validation using riveted joints and repair patches. *Smart materials and structures, 13*(3), 621.

[45] Raju J., Bhalla, S., & Visalakshi, T. (2019). Internal Corrosion Detection in Pipes Using Piezoelectric Transducers. *Structural Health Monitoring 2019*. Doi: 10.12783/shm2019/32164

[46] Dahia, A., Berthelot, E., Le Bihan, Y., & Daniel, L. (2015). A model-based method for the characterisation of stress in magnetic materials using eddy current non-destructive evaluation. *Journal of Physics D: Applied Physics*, *48*(19), 195002.

[47] Junker, W. R., & Clark, W. G. (1983). Eddy current characterization of applied and residual stresses. In D. O. Thompson, & D. E. Chimenti (Eds.), *Review of Progress in Quantitative Nondestructive Evaluation, Vol. 2B* (pp. 1269-1286). New York, NY: Plenum Press.

[48] Wilson, J. W., Tian, G. Y., & Barrans, S. (2007). Residual magnetic field sensing for stress measurement. *Sensors and Actuators A: Physical*, *135*(2), 381-387.

[49] Malhotra, V. M., & Carino, N. J. (2003). Handbook on nondestructive testing of concrete. CRC press.

[50] Waters, C. (1999). RDT-INCOTEST®: For the detection of corrosion under insulation. *Non-destructive Testing Australia*, *36*(5), 124-129.

[51] Tamura H., Tominaga, S., Sasaki, E., & Minesawa, G.V. (2015, September). *ECT-based thickness loss estimation for corroded steel plate.* Paper presented at the 20th International Workshop on Electromagnetic Nondestructive Evaluation (*ENDE2015*), Sendai, Japan (OS3-1).

[52] Wang, H., Li, W., & Feng, Z. (2015). Noncontact thickness measurement of metal films using eddy-current sensors immune to distance variation. *IEEE Transactions on Instrumentation and Measurement*, *64*(9), 2557-2564.

[53] Mao, X., & Lei, Y. (2016). Thickness measurement of metal pipe using swept-frequency eddy current testing. *NDT & E International*, *78*, 10-19.

[54] Wang, J., Yusa, N., Fukutomi, H., & Hashizume, H. (2014, June). Low frequency eddy current inspection of wall-thinning of large pipes by bobbin coils. In C. Xu, L. Yang, & Q. Pan

(Eds.), *FENDT2014. Proceedings of 2014 IEEE Far East Forum on Nondestructive Evaluation/Testing* (pp. 172-175). Piscataway, NJ: IEEE

[55] Luong, B., & Santosa, F. (1998). Quantitative imaging of corrosion in plates by eddy current methods. *SIAM Journal on Applied Mathematics*, *58*(5), 1509-1531.

[56] Cacciola, M., Calcagno, S., Morabito, F. C., & Versaci, M. (2007). Swarm optimization for imaging of corrosion by impedance measurements in eddy current test. *IEEE Transactions on Magnetics*, *43*(4), 1853-1856.

[57] Rosado, L. S., Gonzalez, J. C., Santos, T. G., Ramos, P. M., & Piedade, M. (2013). Geometric optimization of a differential planar eddy currents probe for non-destructive testing. *Sensors and Actuators A: Physical*, *197*, 96-105.

[58] Wang, J., Yusa, N., Pan, H., Kemppainen, M., Virkkunen, I., & Hashizume, H. (2013). Discussion on modeling of thermal fatigue cracks in numerical simulation based on eddy current signals. *NDT&E International*, *55*, 96-101.

[59] Zhou, H. T., Hou, K., Pan, H. L., Chen, J. J., & Wang, Q. M. (2015). Study on the optimization of eddy current testing coil and the defect detection sensitivity. *Procedia Engineering*, *130*, 1649-1657.

[60] Hoshikawa, H., & Koyama, K. (1998). Uniform eddy current probe with little disrupting noise. In D. O. Thompson, & D. E. Chimenti (Eds.), *Review of Progress in Quantitative Nondestructive Evaluation, Vol. 17A* (pp. 1059-1066). New York, NY: Plenum Press.

[61] Koyama, K., Hoshikawa, H., & Taniyama, N. (Eds.) (2000, October). Investigation of eddy current testing of weld zone by uniform eddy current probe. In *Proceedings of 15th World Conference on NDT (WCNDT2000)*. Roma, Italy. Retrieved from https://www.ndt.net/article/wcndt00/papers/idn046/idn046.htm

[62] Roy, D., Kumar Kaushik, B., & Chakraborty, R. (2013). A novel E-shaped coil for eddy current testing. *Sensor Review*, *33*(4), 363-370.

[63] Aoukili, A., & Khamlichi, A. (2016). Modeling an eddy-current probe for damage detection of surface cracks in metallic parts. *Procedia Technology*, *22*, 527-534.

[64] Buck, J. A., Underhill, P. R., Morelli, J. E., & Krause, T. W. (2016). Simultaneous multiparameter measurement in pulsed eddy current steam generator data using artificial neural networks. *IEEE Transactions on Instrumentation and Measurement*, *65*(3), 672-679.

[65] Chady, T., & Sikora, R. (2003). Optimization of eddy-current sensor for multifrequency systems. *IEEE transactions on magnetics*, *39*(3), 1313-1316.

[66] Yating, Y., & Pingan, D. (2007, August). Optimization of an eddy current sensor using finite element method. In *Proceedings of the 2007 IEEE International Conference on Mechatronics and Automation* (pp.3795-3800). Harbin, China. Retrieved from https://ieeexplore.ieee.org/stamp/stamp.jsp?tp=&arnumber=4304179.

[67] Li, J., Zhang, W., Zeng, W., Chen, G., Qiu, Z., Cao, X., & Gao, X. (2017). Estimation of stress distribution in ferromagnetic tensile specimens using low cost eddy current stress measurement system and BP neural network. *PloS ONE*, *12*(11), e0188197.

[68] Cullity, B. D., & Graham, C. D. (2009). *Introduction to magnetic materials* (2nd ed.). Hoboken, NJ: Wiley.

[69] Yamasaki, T., Yamamoto, S., & Hirao, M. (1996). Effect of applied stresses on magnetostriction of low carbon steel. *NDT&E International*, *29*(5), 263-268.

[70] Kim, J. M., Lee, J., & Sohn, H. (2017). Automatic measurement and warning of tension force reduction in a PT tendon using eddy current sensing. *NDT&E International*, *87*, 93-99.

[71] Liu, J.-G., & Becker, W.-J. (2001, May). Force and stress measurements with eddy-current sensors. In *Proceedings II of the SENSOR* (pp.23-28). Nuremberg, Germany. Retrieved from https://www.researchgate.net/profile/Ji_Gou_Liu/publication/267392759_Force_and_Stress_Measurements_with_Eddy_Current_Sensors/links/544e6d440cf26dda08901149.pdf.

[72] Ricken, W., Liu, J.-G, & Becker, W.-J. (2001). GMR and eddy current sensor in use of stress measurement. *Sensors and Actuators A: Physical*, *91*(1-2), 42-45.

[73] Ricken, W., Schoenekess, H.-C., & Becker, W.-J. (2006). Improved multi-sensor for force measurement of pre-stressed steel cables by means of the eddy current technique. *Sensors and Actuators A: Physical*, *129*(1-2), 80-85.

[74] Schoenekess, H.-C., Ricken, W., & Becker, W.-J. (2007). Method to determine tensile stress alterations in prestressing steel strands by means of an eddy-current technique. *IEEE Sensors Journal*, *7*(8), 1200-1205.

[75] Xiu, C., Ren, L., & Li, H. (2017). Investigation on Eddy Current Sensor in Tension Measurement at a Resonant Frequency. *Applied Sciences*, *7*(6), 538.

[76] Nikravesh, S. M. Y., & Goudarzi, M. (2017). A review paper on looseness detection methods in bolted structures. *Latin American Journal of Solids and Structures, 14*(12), 2153-2176.

[77] Khomenko, A., Koricho, E. G., Haq, M., & Cloud, G. L. (2016). Bolt tension monitoring with reusable fiber Bragg-grating sensors. *The Journal of Strain Analysis for Engineering Design, 51*(2), 101-108.

[78] Mekid, S., Bouhraoua, A., & Baroudi, U. (2019). Battery-less wireless remote bolt tension monitoring system. *Mechanical Systems and Signal Processing*, 128, 572-587.

[79] Blitz, J. (1997). *Electrical and magnetic methods of non-destructive testing* (2nd ed.). London, UK: Chapman & Hall.

[80] Lin, Y., Gigliotti, M., Lafarie-Frenot, M. C., Bai, J., Marchand, D., & Mellier, D. (2015). Experimental study to assess the effect of carbon nanotube addition on the through-thickness electrical conductivity of CFRP laminates for aircraft applications. *Composites Part B: Engineering*, *76*, 31-37.

[81] ETHER NDE (2017). The eddy current probe & accessories catalogue [Product Catalogue]. Retrieved from https://namikon2001.com/wp-content/uploads/2017/08/EThER_NDE_Probe_Catalogue_V7.1.pdf.

[82] OLYMPUS NDT (2010). Eddy current inspection: Eddy current probes and accessories [Product Catalogue]. Retrieved from http://www.epsilon-ndt.com/upload/file/eddy-current-problari.pdf.

[83] GE Inspection Technologies (2007). Eddy current probes and accessories catalogue [Product Catalogue]. Retrieved from https://www.tcontrol.ro/Content/prospecte/ECprobes.pdf.

[84] Slaughter, J. C. (2009, October). Coupled structural and magnetic models: Linear magnetostriction in comsol. In *Proceedings of COMSOL Conference*. Boston, M.A. Retrieved from https://www.comsol.eu/paper/download/44538/Slaughter.pdf.

[85] Jiles, D. C., Lee, S. J., & Lo, C. C. H. (2002). The effects of stress on magnetic properties and the use of magnetic measurements for evaluation of materials. In *Conference on Resurgence of Metallic Materials*.

[86] Papadopoulou, S. (2016). Correlation of magnetic properties with deformation in electrical steels. In *IOP Conference Series: Materials Science and Engineering*, *108*(1), pp. 012015): IOP Publishing.

[87] Clark, A. E., Teter, J. P., Wun-Fogle, M., Moffett, M., & Lindberg, J. (1990). Magnetomechanical coupling in Bridgman-grown Tb0. 3Dy0. 7Fe1. 9 at high drive levels. *Journal of applied physics, 67*(9), 5007-5009.

[88] Itami, J. (2017).Eddy current based stress measurement method for steel member and its application. *Master's thesis,* Tokyo Institute of Technology.

[89] Brown Jr, W. F., & Sweer, J. H. (1945). The Fluxball A Test Coil for Point Measurements of Inhomogeneous Magnetic Fields. *Review of Scientific Instruments, 16*(10), 276-279.

[90] Tumanski, S. (2007). Induction coil sensors—A review, *Measurement Science and Technology*, *18*(3), R31-R46.